ELECTROMECHANICAL PROPERTIES OF POLYMER NANOCOMPOSITES CONTAINING PERCOLATED CARBON NANOMATERIAL NETWORK WITH CONTROLLED NANOSTRUCTURE AND INTERFACE

Sang-Ha Hwang

Department of Materials Science Engineering

Graduate School of UNIST

2015

ELECTROMECHANICAL PROPERTIES OF POLYMER NANOCOMPOSITES CONTAINING PERCOLATED CARBON NANOMATERIAL NETWORK WITH CONTROLLED NANOSTRUCTURE AND INTERFACE

Sang-Ha Hwang

Department of Materials Science Engineering

Graduate school of UNIST

Electromechanical Properties of Polymer Nanocomposites Containing Percolated Carbon Nanomaterial Network with Controlled Nanostructure and Interface

A dissertation

submitted to the Graduate School of UNIST

in partial fulfillment of the

requirements for the degree of

Doctor of Philosophy.

Sang-Ha Hwang

1. 16. 2015

Approved by
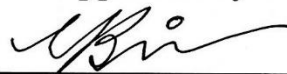
_____

Major Advisor

Young-Bin Park

Electromechanical Properties of Polymer Nanocomposites Containing Percolated Carbon Nanomaterial Network with Controlled Nanostructure and Interface
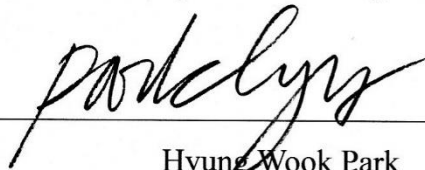
Sang-Ha Hwang

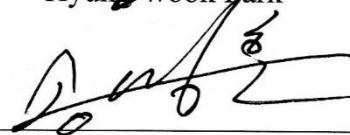This certifies that the dissertation of Sang-Ha Hwang is approved.
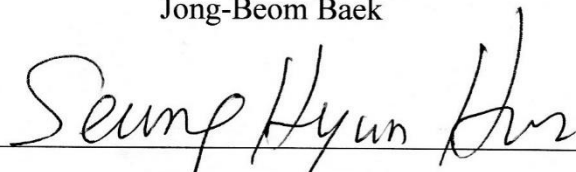
1. 16. 2015

_____

Thesis Supervisor: Young-Bin Park

_____

Hyung Wook Park

_____

Myoung Hoon Song

_____

Jong-Beom Baek

_____

Seung Hyun Hur

Abstract

Strain-induced resistance change, known as piezoresistivity, is one of the unique characteristics of carbon-nanomaterial-filled polymer composites and makes them a potential candidate for strain sensors. This electromechanics-based strain sensing mechanism has received much attention recently due to the distinct combined advantages provided by polymers and the percolated network formed by carbon nanomaterials. Despite the merit of distributed sensing behavior, most of the previous studies have focused on small-area, one-dimensional strain sensing. In order to overcome these limitations, we conducted our research on the aims at studying and developing a multi-faceted approach to enable distributed, large-area, multi-directional strain sensing and to "tailor" the sensing performance by controlling the following factors: (1) carbon nanomaterial geometry and hybridization; (2) carbon nanomaterial-polymer interface; and (3) microstructures including porosity, alignment and micro-domain.

The effects of carbon nanomaterial geometry on piezoresistivity could be best captured by studying the electromechanical behavior of carbon nanotube buckypapers, graphene sheets, and carbon nanotubes-graphene hybrids, as they enable "isolation" of the percolated carbon nanomaterial network. The strain sensing behavior of polymer-impregnated carbon nanomaterial sheets were also studied, which provided additional advantages of highly loaded nanocomposites and easy material handling. Reduced graphene oxide was selected and coated on a polymer substrate, which enabled 2D distributed conductive network and allowed tailored sensitivity based on the interfacial strength controlled by the reduction method. A further study about interfacial bonding discussed on the effects of polydopamine-functionalized reduced graphene oxide dispersed in poly(vinyl alcohol), which served as a conductometric humidity sensor. At the same time, polydopamine functionalization resulted in remarkable simultaneous improvements in tensile modulus, strength, and percent elongation, which suggests enhanced interfacial strength as well as matrix reinforcement. Finally, the piezoresistivity of highly porous nanocomposites were investigated using graphene oxide hydrogels with controlled pore size and distribution. This self-assembled 3D architectures allowed tailoring of strain sensitivity and served as a potential alternative solution that can replace conventional pressure, vibration sensors commonly used for structural health monitoring.

The conducted study covered a comprehensive approach to develop carbon-nanomaterial-enabled smart sensors, encompassing materials design and processing, understanding of the underlying physics, and applications for wide-area sensing. This is unique and significant research that bridges the gap between the exceptional properties of nano-scale materials and macro-scale sensing systems. It is anticipated that the outcome of the proposed research will make inroads into application areas where large-area strain sensing and intelligent structural health monitoring, enabled by distributed sensor network with tailored accuracy and sensitivity, are required, including aerospace, automotive, civil structures, wind turbines, and nuclear power plants.

Contents

List of figures

Figure 4-2 (a) Electromechanical behavior measurement setup and (b) mechanism of tensile strain generation in PC-HS composite sheets bonded to a PMMA plate subjected to three-point bending.

Figure 4-3 Digital photographs and SEM images of CM-250/M-5 (5:5) hybrid sheet ((a)–(c)) and CM-250/NGP (5:5) hybrid sheet ((d)–(f)). (a), (c) Digital photographs upon folding. (b), (e) SEM images of hybrid sheet surface. (c), (f) SEM images of crack morphology in hybrid sheets with in-plane tension.

Figure 4-4 SEM images of fracture surfaces of PC-impregnated BP and HS: (a) low- and (b) high-magnification images of PC-BP; (c) low- and (d) high-magnification images of PC-CM-250/M-5; (e) low- and (f) high-magnification images of PC-CM-250/M-15; (g) low- and (h) high-magnification images of PC-CM-250/NGP.

Figure 4-5 Tensile properties of (a) before PC impregnation and PC-BP and PC-HS with: (b) material types (at MWCNT:xGnP or MWCNT:NGP of 50:50), (c) PC-CM-250/M-5 and (d) PC-CM-250/NGP with varying M-5 and NGP content, respectively.

Figure 4-6 Effect of M-5 and NGP on the normalized inter-electrode resistance of hybrid sheets with each distance group at 50 wt% of M-5 and NGP loading.

Figure 4-7 Resistance change in: (a) CM-250 buckypaper; (b) CM-250=M-5 (5:5) hybrid sheet; (c) CM-250=NGP (5:5) hybrid sheet under cyclic flexural strain. ('R45' denotes resistance between electrodes 4 and 5, and so forth.)

Figure 4-8 Effects of M-5 and NGP content on piezoresistivity in the longitudinal direction (R45) of CM-250-based hybrid sheets: (a) CM-250/M-5 hybrid sheets; (b) CM-250/NGP hybrid sheets.

Figure 4-9 Schematic representation of microstructural changes in buckypaper and hybrid sheets subjected to mechanical strains.

Figure 4-10 Electromechanical behavior of PC-CM-250/M-5 composite sheets with varying CM-250:M-5 ratio under flexural loading up to fracture, measured in: (a) longitudinal, (b) diagonal and (c) transverse directions.

Figure 4-11 Electromechanical behavior of PC-CM-250/NGP composite sheets with varying CM-250:NGP ratio under flexural loading up to fracture, measured in: (a) longitudinal, (b) diagonal and (c) transverse directions.

Figure 6-1 A photograph and proposed structure of a dGO/PVA composite film.

Figure 6-2 (a) and (b) AFM image and height profile of GO. (c) and (d) AFM image and height profile of dGO. GO and dGO (dopamine:GO = 0.5:1) samples were spin-coated on a Si wafer for AFM measurements.

Figure 6-3 (a) XPS survey spectra and (b) C1s binding energy region of GO and dGO spin-coated on a Si wafer. An additional Cl 2p peak in (a) originates from dopamine hydrochloride (HCl) which was used as the precursor of polydopamine.

Figure 6-4 (a) ATR-FTIR spectra of GO and dGO samples in the region between 4000 and 700 cm^{-1} and (b) magnified wave number range of 2,000 to 700 cm^{-1} of GO and dGO. To obtain a thick film of GO and dGO for ATR-FTIR measurement, each solution was repeatedly coated onto a Si wafer by drop casting.

Figure 6-5 Stress-strain curves of: (a) neat PVA, GO/PVA, dGO/PVA composite films at 0.5 wt.% GO or dGO loading and (b) dGO/PVA composite films with various dGO loadings (polydopamine:GO = 0.5:1).

Figure 6-6 (a) Swelling ratio, (b) weight losses measured from water-dipping tests performed on dried dGO/PVA (polydopamine:GO=0.5:1) composite films with various GO contents. (c) Optical photograph shows difference in weight loss between neat PVA and dGO/PVA films after 12 hours of dipping in water at room temperature.

Figure 6-7 Variation of resistance with respect to (a) stepwise dehumidification and (b) linear humidification for different dGO loadings.

Figure 6-8 Resistance reversibility in the response of a 5 wt.% dGO/PVA film at 30℃.

Figure 7-1 (a) EDA-rGOH-5 contained in water after crosslinking reaction and (b) SEM image shows its porous microstructure.

Figure 7-2 C 1s binding region of (a) VC-rGOH-5, (b) EDA-rGOH-5, (c) EDA-rGOH-10 and (d) EDA-rGOH-15 were taken from XPS spectra.

List of tables

Nomenclature

CNMs: Carbon nanomaterials

CNTs: Carbon nanotubes

SWCNTs: Single-wall carbon nanotubes

MWCNTs: Multi-wall carbon nanotubes

$\vec{C}$: Chiral vector

n, m: The number of steps along the zigzag carbon bonds of the hexagonal lattice in sp^2 carbons (integers)

$\vec{a}_1, \ \vec{a}_2$: Unit vector

FEM: Finite elemental modeling

NGPs: Nanographene platelets

T_g: Glass transition temperature

PAN: Polyacrylonitrile

PMMA: Polymethyl methacrylate

xGnPs: Exfoliated graphite nanoplatelets

GO: Graphene oxide

PVA: Polyvinyl alcohol

EG: Exfoliated graphene

CVD: Chemical vapor deposition

PECVD: Plasma-enhanced chemical vapor deposition

SHM: Structural health monitoring

rGO: Reduced graphene oxide

EDA: Ethylene diamine

VC: Ascorbic acid, Vitamine C

TEM: Transmission electron microscopy

SEM: Scanning electron microscopy

BPs: Buckypapers

HS: hybrid sheets

BET: Brunauer–Emmett–Teller

DMA: Dynamic mechanical analyzer

$\bar{r}_{i,j}$: Normalized resistance measured between electrodes i and j (i, j = 1, 2, 3, …..,8)

$R_{i,j}$: Raw resistance measured between electrodes i and j

$L_{i,j}$: Distance between electrodes i and j

$\overline{\Delta r}_{i,j}$: Normalized change in resistance measured between electrodes i and j

$\Delta R_{i,j}$: Resistance change in resistance measured between electrodes i and j

$(R_0)_{i,j}$: Initial resistance measured between electrodes i and j

GF: Gauge factor

R_0: Electrical resistance of composite in the pre-stressed state

ΔR: Resistance change, $(R-R_0)$

ε: Tensile strain

R^2: Linearity

Tr-GO: Thermally reduced graphene oxide

Hr-GO: Reduced graphene oxide using hydrazine as a reducing agent, Chemically reduced graphene oxide

XPS: X-ray photoelectron spectroscopy

eV: Electron volt (=$1.60217657 \times 10^{-19}$ Joule)

AE: Acoustic emission

PAA: Polyacrylic acid

dGO: Polydopamine functionalized graphene oxide

W_0, W: Weights of the sample before and after immersing in water, respectively.

RH: Relative humidity (%)

V: Voltage

AFM: Atomic force microscopy

ATR-FTIR: Attenuated total reflectance Fourier transform infrared (ATR-FTIR)

rGOHs: Reduced graphene oxide hydrogels

XRD: X-ray dirrractometer

FE-SEM: Field emission-scanning electron microscope

I. INTRODUCTION

Depending on the size of the solid additives, composites can be categorized into microcomposites (conventional composites with filler size in microns) and nanocomposites (composites with filler size less than 100 nm in at least one direction) [1] In the case of the microcomposites, common forms of fillers are granules and fibers. Conventional composites generally require high filler loadings to modify the matrix properties, which presents both technological and economic challenges. Also, while such fillers contribute to enhancement of modulus and strength of composite materials, they often lead to reduction in toughness and embrittlement due to the complexities associated with processing [2]. On the contrary, nanocomposites are commonly fabricated by dispersing the nanofiller in the polymer matrix. Nanofillers are a new class of filler, exhibiting at least one characteristic length in the order of nanometers [3].

Nanocomposites generally exhibit four major advantages over conventional composites:

(1) Light weight (high specific modulus and strength due to greater reinforcing efficiency);

(2) Low cost (small amount of filler required);

(3) Improved properties compared to conventional composites; and

(4) Ability to impart multifunctionalities (i.e., electrically and thermally conductive composites with enhanced mechanical properties).

Nanocomposites can be further categorized by the geometry of nanofiller, which can vary from isotropic to highly anisotropic. Nanofillers can be classified as nanospheres (0-dimensional or 3-dimensional), nanotubes or nanowires (1-dimensional), and nanoplatelets (2-dimensional). The high specific surface area of nanofiller, that is, high specific interfacial area of the composite material, offers the possibility of polymer-nanofiller interaction at the molecular level, yielding substantial modification of their properties. Hence, significant improvements in properties can be achieved by incorporating a small amount of nanofiller (typically, 1-5% in mass fraction). Also, the nanoscale-confined polymer and nanofiller structure, combined with alignments of these constituents contribute to the improvements of physical properties. However, the performance of nanocomposites strongly depends on the degree of dispersion and the quality of adhesion between the nanofiller and polymer matrix, which depend in part on the chemistry between the constituents and processing factors.

In terms of nanocomposite processing, there are two important aims: (1) de-agglomeration of nanofillers and (2) uniform distribution in the polymer matrix. The former process is directly related to the interparticle forces. For this purpose, the applied processing forces should overcome the cohesive forces between nanoparticles. Particle-particle and particle-polymer interaction forces are very important factors in determining both the ease of formation of nanocomposites and the performance of the final product. The interfacial area between nanoparticles and polymer matrix should be maximized

to increase the benefits of the nanofiller-polymer interaction. This means that agglomerates should be broken down to smallest units, and ideally exfoliated into individual nanoparticles. Alternatively, especially for 2D nanoplatelets, intercalation provides an opportunity for significantly increased interfacial area. In either case, it is imperative that good adhesion exists at the interface so that efficient load transfer and reinforcement can be achieved. As it is not always possible to have sufficient compatibility between nanofillers and polymer matrix, it is common to employ surfactants and compatibilizers that enhance these interactions. Thus, surfactants and compatibilizers may be considered as processing aids that help fabricate nanocomposites with desired performance [4].

There is a way to classify the nanoparticles based on their chemical composition and atomic structure. In this study, emphasis will be place on the carbon nanomaterials (CNMs) with varying dimensions, especially on 1D carbon nanotubes (CNTs) and 2D graphene or nanographite platelets, both of which are used as nanoscale filler materials for multifunctional conductive polymer nanocomposites

Since the electrical conduction in CNM-polymer composites is enabled by the formation of interconnected percolated network formed by the nanofillers, it is possible to disrupt or densify by subjecting it to changes in temperature, pressure, and chemical vapor [5-7]. This behavior can be used for a wide range of potential applications, including biological, chemical and mechanical sensors and actuators [8]. Biochemical sensors usually monitor the change in the electrical behavior of composite driven by various ionic and nonionic interactions between analyte and nanoparticles, which is the key analytic mechanism[9]. It is important to increase the contact area between analyte and nanoparticles to maximize their interactions so as to increase the sensitivity. In this regard, thin film technology is commonly employed to fabricate layer-by-layer nanocomposite sensors consisting of porous conductive layers. Both impurity content and crystallinity of nanofiller are also important factors that govern the sensitivity of biochemical sensors [10].

In the case of electromechanical sensors, however, their electrical behavior is monitored with respect to the mechanical deformation. Resistivity is one of the most commonly analyzed physical quantities in the study of nanocomposite-based sensors. Strain-induced resistance change, known as piezoresistivity, is an appropriate electromechanical property for addressing the strain level of target area and structure [11-14]. As shown in Fig. 1-1, the piezoresistive behavior is governed by the mean distance between nanofillers and three electromechanical mechanisms: (1) external-load-induced change in network formed by conductive fillers with physical contact; (2) tunneling effect among neighboring fillers; and (3) inherent piezoresistivity of conductive fillers themselves. As shown in Fig. 1-2, overall resistance change is thereby derived from decreased or increased number of conductive networks that were formed with a combination of these three mechanisms.

Recently, in the area of structural health monitoring, strain sensing using polymer nanocomposites have received much attention due to the distinct advantages of polymers and nanofillers [15-18]. In particular, a number of theoretical and experimental research on strain sensing behavior of CNT-

polymer and graphene-polymer composites has been reported on the reversible electromechanical characteristics of CNT buckypapers [19-21], CNT-polymer composites [22-24], and graphene-polymer composites [18, 25]. However, many of these previous studies were focused on small scale, one-dimensional strain sensing capability. Hence, technological demand was brought up for large-area, multi-directional strain sensing to apply nanocomposite-based strain sensors to structural health monitoring. To achieve this goal, a systematic investigation on nanocomposite strain sensors, in terms of nanomaterial geometry, interfacial adhesion, and orientation, is necessary to design tailored, scalable and embeddable strain sensors.

The experimental studies on CNM-polymer composites has mainly investigated the effects of CNM content and processing method on composite properties [2]. However, there are other experimental parameters that affect the performance of nanocomposite-based strain sensors, including CNM geometry, interfacial adhesion, and micro-structure. Also, a wide range of material and processing parameters available enables configuration of the sensor with much greater design flexibility, tailored to the target structure.

As shown in Fig. 1-3, seven controllable experimental parameters can be considered to achieve durable, accurate, cost-effective and wide-area strain-monitoring sensors. The parameters in red boxes are the focuses of this research, and three individual experiments were designed to study the effects of each controllable parameter on strain sensing performance. Additionally, nanofiller content or percolated network density was controlled for each experiment. The other three parameters were also controlled or designed for each experiment in case their influences on strain sensing performance are independently affected or distinguished.
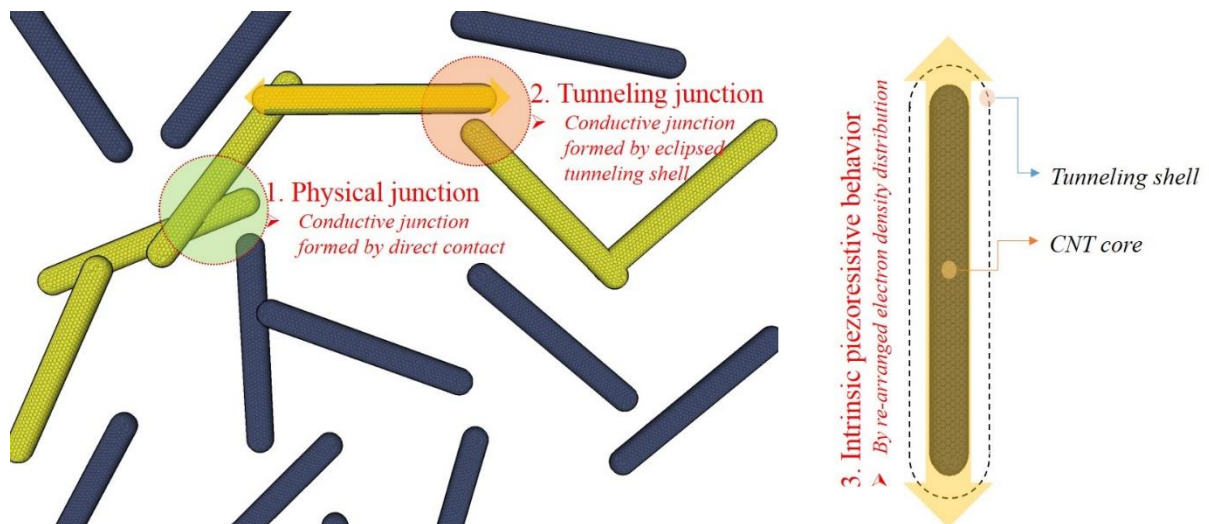
Figure 1-1 Schematic illustration of an electrical conductive CNT network (yellow) in a polymer matrix and its 3 detailed piezoresistive network components (red).
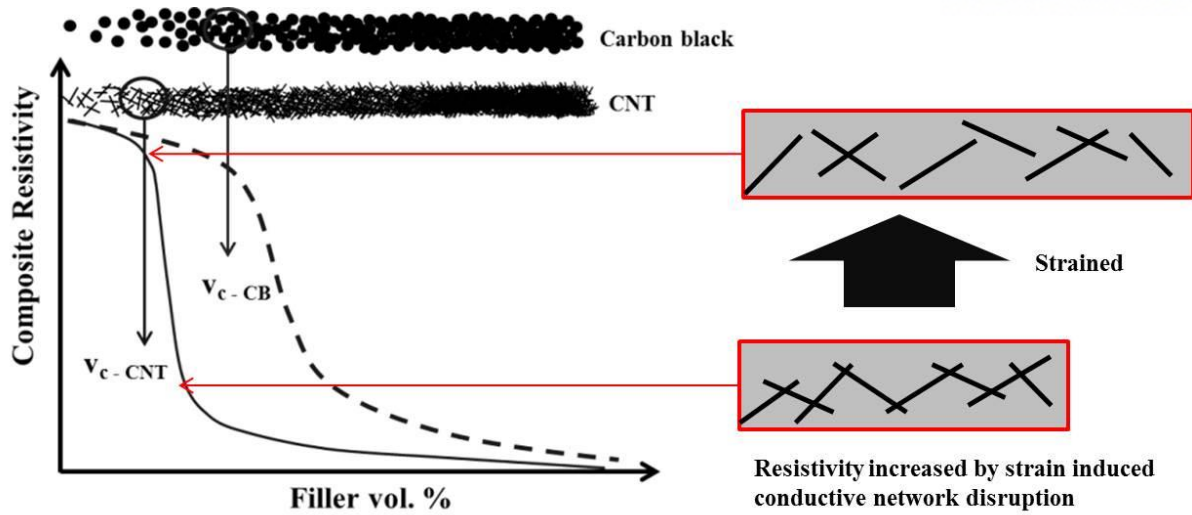
Figure 1-2 Illustration of CNM (CNT and carbon black) composite conductive network percolation (v_c) and simple model of piezoresistivity in CNT-polymer composite.
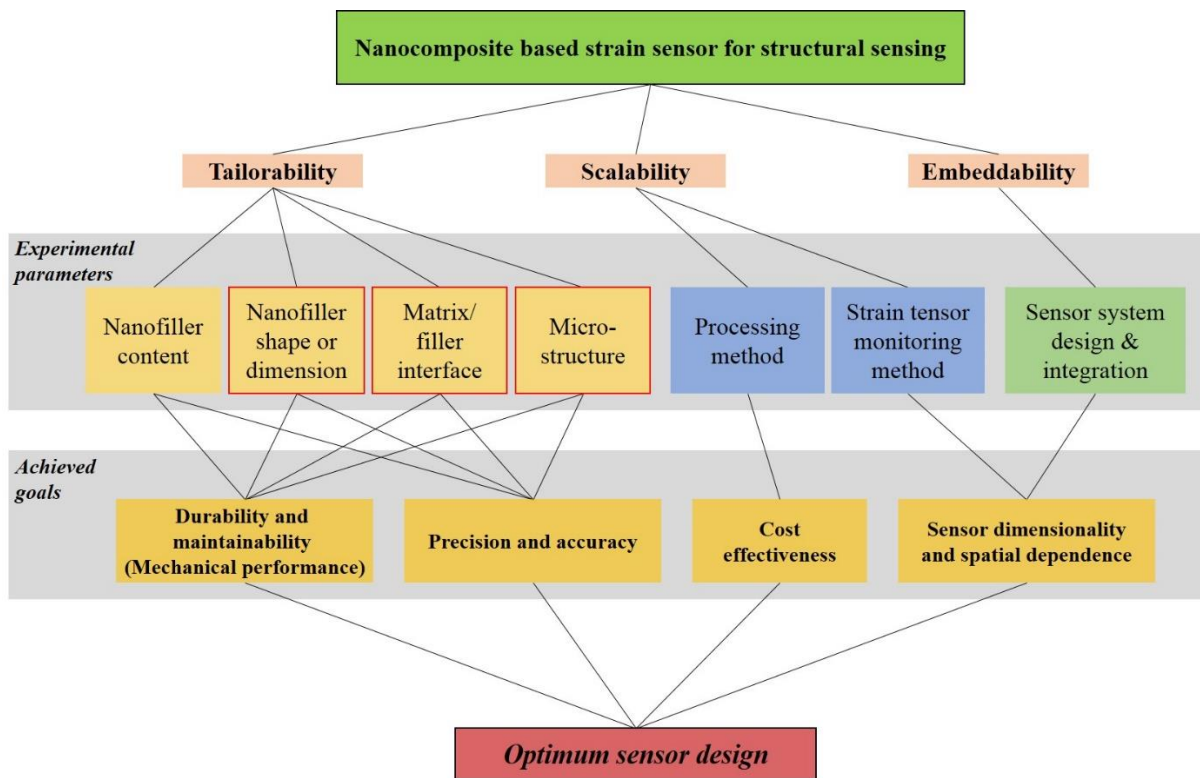
Figure 1-3 General requirements for nanocomposite-based strain sensors and experimental parameters that affect sensing performance and design.

II. LITERATURE REVIEW

2. 1 Carbon Nanomaterials Based Nanocomposites

2. 1. 1 Carbon Nanotubes and Their Polymer Nanocomposites

The rise of CNTs has stimulated significant number of investigation on their physical and mechanical properties and potential applications for decades. It has been confirmed both theoretically and experimentally that CNTs possess remarkably high stiffness and strength thereby have great potential for composite application as fillers and reinforcements [26]. CNTs also have exceptionally high electrical and thermal conductivities. These unique mechanical and physical properties of nanotubes combined with their high aspect ratio (length/diameter) and low density have brought about extensive research in creating composite material systems to exploit these properties [1]. Considerable interest has focused on utilizing nanotubes as reinforcement to tailor mechanical [27-29] properties and its conductive character utilized as electrically [30-32] and thermally [33, 34] conductive composites.

Ideally, a single-walled carbon nanotube (SWCNT), which is the basic structure of CNT, is formed by rolling a single graphene sheet (hexagonal sp^2 hybridized carbon structure) into a cylinder, and a multi-walled nanotube (MWCNT) is composed of multiple layer of graphene cylinders with a 3.4 Å of interlayer spacing. Nanotube properties are highly structure- and size-dependent and are influenced by atomic arrangement called chirality. The chirality of nanotubes can be defined by chiral vector as shown in Fig. 2-1 and described: $\vec{C} = n\vec{a}_1 + m\vec{a}_2$. Where the integers (n,m) are the number of steps along the zigzag carbon bonds of the hexagonal lattice and $\vec{a}_1$ and $\vec{a}_2$ are unit vectors. Nanotubes with n = m are called armchair tubes (chiral angle of 30°), and nanotubes with m = 0 are known as zigzag tubes (chiral angles are 0°). For any other values of n and m the tubes are chiral tubes. Depending on chirality, SWCNTs can be either conducting or semiconducting. Wei *et al.* [35] demonstrated that MWCNTs have extraordinarily high current carrying capacity, sustaining current densities greater than 10^9 A·cm^{-2}. These novel electrical properties have generated substantial interest in utilizing CNTs in nanoelectronics.
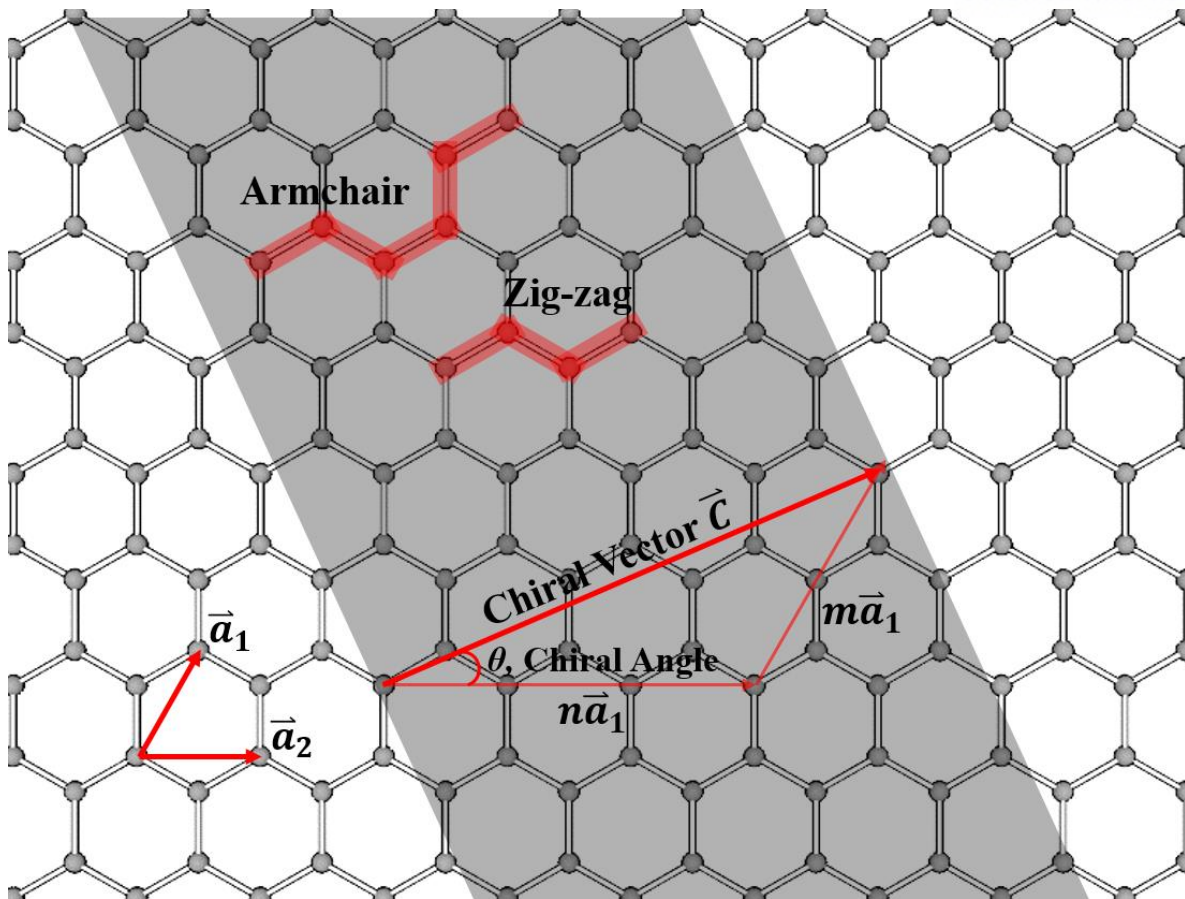
Figure 2-1 Chirality of CNTs depend on rolling direction of a graphene sheet.

Baughman *et al*. [36] first reported electromechanical actuation behavior of CNTs, where charge induced mechanical deformation of nanotubes. Unlike conventional piezoelectric materials, where dipoles are oriented by applying high electric fields at elevated temperatures, electromechanical coupling of CNTs results from phonon frequency shifts as a consequence of charge injection. The influence of local mechanical deformation on their electrical properties was investigated, for example, by Tombler *et al*. [37] deformed a metallic CNT using an atomic force microscope while measuring changes in electrical conductivity then reversible changes in conductivity were observed. Theoretical investigation by Nardelli *et al*. [38] observed the influence of bending deformation on a CNT's electrical properties and reported that the deformation altered the band structure of the nanotube, depending on nanotube chirality. This intrinsic electromechanical characteristics of CNTs make them ideal candidates for future multi-functional material systems that combine adaptive and sensory capabilities.

There is considerable interest in making macroscopic engineering materials that can exploit these novel material properties. The coupling of physical properties with mechanical deformation particularly has widespread application in the development of multi-functional materials for sensing and actuation. Particular importance in the development of sensors and actuators based on CNT nanocomposite is their electrical conductivity and understanding of underlying mechanisms.

Polymeric or ceramic matrix of composites is usually considered as non-conductive material because of its extremely low electrical conductivity (in the order of 10^{-10}– 10^{-15} S ·m^{-1}). Dispersing conductive filler into the non-conductive matrix can form percolated conductive composites. In this case, their electrical conductivity is strongly dependent on the volume fraction of the conductive filler. At low volume fractions, the conductivity remains very close to the conductivity of the matrix. When a certain volume fraction is reached, the conductivity of the composite drastically increases by many orders of magnitude. The phenomenon is known as percolation and can be well explained by simple percolation theory. The electrical percolation threshold of conductive reinforcements embedded in an insulating matrix is sensitive to the geometrical shape of the conductive phase. The small size and large aspect ratio are helpful to lower the percolation threshold [39]. Because CNTs have large aspect ratios (10^2–10^4), many researches have reported the possibility of significantly low electrical percolation thresholds. Sandler *et al*. [40] and Moisala *et al*. [41] have reported extremely low percolation thresholds for MWCNT nanocomposites, and Bryning *et al*. [42] reported very low percolation thresholds in SWCNT nanocomposites. Thostenson *et al*. [43] examined the influence of the nanostructure on the nanocomposite electrical properties. They used calendering to fabricate highly dispersed and dispersion geometry controlled nanocomposites. For both cases, nanocomposites exhibited percolation thresholds below 0.1 wt%. Depending on the polymer matrix, the processing technique, and the nanotube type used, wide range of percolation thresholds from 0.001 wt.% to more than 10 wt.% have been reported.

The percolation threshold p_c is defined mathematically as a filler volume fraction at which an infinite spanning cluster appears in an infinite system [44]. For all volume fractions $p > p_c$, the probability of finding a spanning cluster extending from one side of the system to the other side is 1. Whereas for all volume fractions $p < p_c$, the probability of finding such an infinite cluster is 0. But in composite science, the percolation threshold is usually defined as the filler volume faction at which measurements on specimens or results of numerical simulations begin to show percolation behavior. The percolation threshold may sometimes be surprisingly low for CNM-polymer composites but is actually with some degree of probabilities.

To find the theoretically defined percolation threshold and to predict its percolation behavior, the effective or ideal percolation threshold obtained numerically or experimentally for finite-size networks needs to be extrapolated to infinite system size based on the finite element modeling (FEM) with several detailed parameters. For example, Li *et al*. [45] obtained the percolation threshold as a function of nanotube aspect ratio and nanotube curl ratio for infinite systems. For wavy nanotubes, an effective nanotube length which is the maximum distance between a pair of arbitrary points on the nanotube was considered. It is also shown that the percolation threshold of wavy nanotubes increases with increasing curl ratio. The relationship between the percolation threshold and the aspect ratio of wavy nanotubes at a certain curl ratio is also roughly linear in a logarithmical balance as shown in Fig. 2-2.
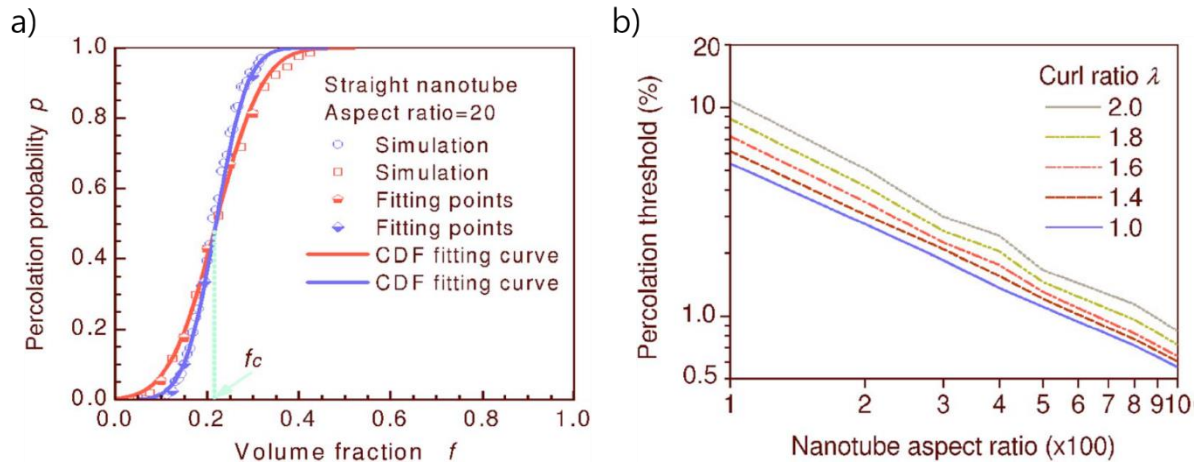
Figure 2-2 (a) Fitting of *p-f* curves by cumulative distribution functions and (b) Effect of nanotube waviness on percolation threshold [45].

Several groups have reported electrical resistivity results for MWCNT and SWCNT ropes [46-48]. Although the differences in the electrical properties of different nanotubes can be fairly significant, the electrical conductivity of individual CNTs are essentially in the order of 10^4–10^7 S·m^{-1}. From the comparison of MWCNT and SWCNT, Gojny *et al.* [49] concluded that MWCNTs offer the highest potential for enhancement of electrical conductivity. The logic behind this conclusion is that the multi-walled nanotubes usually have a better dispersion than SWCNTs.

Measured electrical conductivities for nanotube-based composites typically ranged from 10^{-5} – 10^{-2} S·m^{-1} for nanotube contents above the percolation threshold [50, 51]. However, electrical conductivity tailored to the range of 0.01–3480 S·m^{-1} by varying the CNT content range 0.11 - 15 wt.% has also been reported [11, 52]. Surely, the increase of the CNT volume fraction can increase the electrical conductivity of composites, but the wide range of electrical conductivity reflects the complex nature of CNT-based conductive composites that cannot be explained only by increased nanotube volume fractions. Stermann *et al.* [53] concluded that the overall electrical conductivity of CNT percolated networks or CNT-based composites are dominated by the contact resistance between CNTs. Measurements on crossed SWCNTs gave contact resistance of 100 – 400 kΩ for metal-metal or semiconducting-semiconducting SWCNT junctions and two orders of magnitude higher values for metal-semiconducting junctions reported [54]. The contact resistance is further enhanced and complicated when CNTs are dispersed in a matrix material. There is a thin insulating layer bridged between the contact points of the junction nanotubes. If this insulating layer is thin enough, this insulating layer may not prevent electric tunneling effect [55] but certainly increases the contact resistance. Kilbride *et al.* [50] found the significantly low conductivity from the studies of CNT-polymer thin films,. They suggested that conduction in the composite films is dominated by electric tunneling effect and a thick coating of polymer around nanotubes results in poor electrical conductivity.

More recent study by Li *et al*. [56] reported that the maximum tunneling distance in CNT based polymer or ceramic composites is about 1.8 nm. Their simulation results also indicate that the contact resistance plays a dominant role in nanotube composite films in contrast to the dominant role of the intrinsic resistance of nanotubes. Based on this result, the primary reason for diverse experimental data of electrical conductivity of CNT based nanocomposite is the different thickness of insulating matrix formed in between distant nanotubes. Hence, it is expected that the electrical conductivity of the nanocomposite can be significantly improved if the nanotubes are well dispersed and the thickness of insulating film is effectively reduced.

The discussion above has been mainly based on the assumption that a uniform or random nanotube distribution facilitates the formation of conductive spanning clusters and thus results in higher conductivity. This assumption is adopted in the use of Monte Carlo simulations where a statistically homogeneous filler distribution forms the basis of analysis. Similarly, in experimental measurements of conductivities, researchers have strived to pursue composite systems with well dispersed fillers. Such an ''ideal'' system forms a basis for comparison of conductivity percolation thresholds as influenced by such factors as filler aspect ratio, matrix materials, contact resistance, nanotube waviness, *etc*.

However, it is imperative to appreciate the probabilistic nature of the formation of filler spanning clusters. The deviation from the ''ideal'', uniform filler distribution can obviously enhance the composite conductivity. In fact it has been recently reported that agglomeration of CNTs to a certain extent helps enhancing the composite conductivity, especially at filler fraction above the percolation threshold [57, 58]. This experimental condition is equivalent to the numerical simulation where instead of their random placement, nanotubes are deliberately placed in higher frequency at certain clusters which can then more readily form a spanning cluster in a given direction. The limiting case in such experimental as well as simulation/analysis work is the alignment of nanotubes in a predetermined orientation. Local agglomeration is perhaps one of the reasons behind the scattering of percolation threshold values reported by various researchers, and the fluctuation could be either higher or lower than that of the ''ideal'' uniform system. Lastly, it should be noted that while partially agglomerated system may have the benefit of enhancing the composite conductivity, it may be technically challenging to produce them in a highly controlled manner.

There are some controversial results regarding the dependence of electrical conductivity on nanotube alignment. Haggenmueller *et al*. [59] reported single-walled CNTs–polymer composites with enhanced electrical properties by aligning nanotubes in the matrix. Choi *et al*. [60] also reported that the nanotube alignment contributed to the enhancement of electrical conductivity of CNT–polymer composites. The effect was explained by the more efficient percolation path for the parallel direction and/or the decease of disorder by alignment of nanotubes. But the results of Du *et al*. [61] indicated that the alignment of nanotubes in the polymer matrix significantly lower the electrical conductivity compared with that of the unaligned composite with the same nanotube concentration. Their further study concluded that the

highest conductivity occurs when the nanotubes in the composite are slightly aligned rather than randomly isotropic [31]. The controversial results can hardly be explained by the difference between the orientation controlling techniques employed because the results used in the comparisons were usually obtained from the same technique.

2. 1. 2 Graphene and Their Polymer Nanocomposites

Since the discovery of graphene, this single-layered one atom-thick planar structure has considered the promising experimental platform for physics and nanotechnology [62]. As shown in Table 2-1, several attempts have been made to synthesize graphene on a large scale to address the needs of various industries, particularly the composite industry, in which the use of graphene has dramatically transformed the global market for the production of state-of-the-art composite materials. The addition of graphene to a host matrix has achieved a number of enhanced properties with promising applications in many industries, such as aerospace, electronics, energy, structural and mechanical, environmental and medicine.

Because of graphene's exceptional mechanical, electrical, and thermal properties, it considered as the most promising candidate to be a major filler for nanocomposites and several unique applications [63-65]. Graphene nanocomposites at very low loading show substantial enhancements in their multifunctional aspects, compared to conventional composites and their materials [66]. This not only makes the material with light weight, but also makes it strong and exceptional for various multifunctional applications. As described in previous sections, the remarkable properties of nanomaterials showing possibility to improve the several physical and mechanical properties of the host matrix upon homogenous dispersion. This helps in strengthening and increasing the interfacial area between the graphene and the host matrix. The interfacial area and bonding are dictates the emergence of the cumulative properties of graphene in nanocomposites. Kuilla et al. [67] recently reviewed graphene-polymer nanocomposites, and systematically explained the importance of graphene type, host material type especially on the electrical and mechanical properties of nanocomposites. They also summarized a comparison of various experimental results of nanofillers and listed their important applications in detail. Many significant reports on graphene-based nanocomposites with a polymer matrix reported in recent years. Jang et al. [68] reviewed the processing methods of nanographene platelets (NGPs) nanocomposites. Hansma et al. [69] showed fabrication of more graphene like nanofiller-based nanocomposites. They demonstrated successful optimization of the amount and interfacial adhesion so as to achieve strong, low-density, lightweight, and more resilient nanocomposites. Ramanathan et al. [70] reported increase in the glass transition temperature (T_g) of a polymer matrix with functionalized graphene sheets. They observed that, by the addition of 1wt% of functionalized graphene sheets to the polyacrylonitrile (PAN), the T_g of the composite material increased by 40℃, whereas, 30℃ increased with addition of only 0.5wt% to polymethyl methacrylate (PMMA). They also observed 80% increase

in elastic modulus and 20% increase in ultimate tensile strength by addition of 1wt.% graphene to PMMA. These exceptional results concluded that monolayered functionalized graphene serves as the best nanofiller among all examined nanofillers in terms of mechanical and thermal properties. Yu *et al*. [71] investigated epoxy-based exfoliated graphite nanoplatelets (xGnP) nanocomposites and showed possibility for the electronic applications especially for development of thermal management materials and concluded that it has improved performance compared to that of CNTs. Liu *et al*. [72] successfully synthesized graphene-fullerene hybrid nanocomposites and examined its optical properties. Booth *et al*. [73] demonstrated the mechanically robust macroscopic graphene freestanding sheet that can withstand under heavy loads and showed exceptionally high stiffness. Watcharotone *et al*. [74] fabricated a transparent, electrically conductive thin film using simple spin-coating and various reduction of graphene oxide (GO). They mixed GO in the silica solution to obtain metal-encapsulated graphene nanocomposites. Recently, more advanced graphene-based composite research conducted by Lee *et al*. [75] used cryomilling to synthesize fine particles of graphene and chitosan. The mixture was sonicated and layered to form nanocomposites. The graphene particles conferred a cumulative effect in improving the mechanical attributes of the composite while decreasing the agglomeration quotient of graphene during mixing. Guo *et al*. [76] prepared a water-dispersed graphene-tryptophan-polyvinyl alcohol (PVA) nanocomposite for improving tensile strength, modulus, and thermal stability. There was a 23% increase in tensile strength when only a small loading of graphene (0.2 wt %) was introduced in the PVA matrix. Ansari *et al*. [77] studied the DC electrical conductivity retention of their indigenously prepared graphene-PANI-MWCNT nanocomposite in air and also assessed the cyclic aging. They found that Pani-graphene showed higher electrical conductivity and good stability for the DC electrical conductivity retention under isothermal conditions. Jeon *et al*. [78] prepared an exfoliated-graphene- (EG-) cellulose acetate nanocomposite using the melt compounding. They found that exfoliated graphene (EG) was uniformly dispersed in the host matrix with lower loadings. They also found that the composite had high thermal stability and improved conductivity and modulus.

So far, graphene shows a great number of applications including engineering, electronics, energy, biomedical and many more [79]. Majority of the reported results dealt with electronic/sensor-oriented applications, to generalize the broad applications of graphene and graphene-based nanocomposite into their respective disciplines.

Although recent research activities have focused on experimental work so far, theoretical analysis still plays a crucial role in understanding their mechanisms, molecular level dynamics, and underlying basic physical model. Many advanced simulation tools and theories confirmed from CNT-based nanocomposite researches provide chance to analyze specific results for graphene nanocomposites. With the aid of these cumulated and well-defined analysis approach, more fundamental understanding and guide to successful design for nanocomposite can be systematically achieved. Such theoretical investigations are expected to help the investigators to optimize the system for their applications and

case studies.

Table 2-2 Comparison of various methods for fabrication of of graphene and its derivatives

Methods	Conditions	Yield and properties	Ref.
Bottom-up approaches			
CVD	Carbon sources: CH_4, H_2 Substrate: Ni, Ru, Cu Temperature: 1000℃	Sheet size of up to a few tens of micrometers.	[80, 81]
PECVD	Carbon source: CH4, H2 Substrate: Cu Temperature: 650℃	Large area of more than 1 cm of monolayer graphene	[82]
Graphitization	Substrate: 6H-SiC(0001) Temperature: 1280℃	Grain size: up to 50 μm long, 1 μm wide	[83]
Solvothermal	Reagents: Na and ethanol Temperature: 220℃	Folded graphene structures Bulk conductivity: ~0.05 S·m^{-1}	[84]
Organic synthesis	Thermal fusion of polycyclic aromatic hydrocarbons at 1100℃	For a 30 nm thick film on quartz, conductivity: 20,600 S·m^{-1}	[85]
Top-down approaches			
Liquid exfoliation of graphite	Intercalate: NMP	Single-layer yield: 7–12 wt.% after purification Film conductivity: ~6,500 S·m^{-1}	[86]
	Intercalate: SDBS	Single-layer yield: ~3% with a size of ~1 μm Film conductivity: ~35 S·m^{-1}	[87]
Thermal exfoliation and liquid intercalation	Thermal exfoliation at 1000℃ Intercalates: oleum and TBA	Size: ~250 nm Resistance of single sheet: 10–20 kΩ	[88]
Electrochemical exfoliation	Electrolyte: 1-Octyl-3-methyl-imidazolium hexafluorophosphate Electrodes: graphite rods	Sheet size: 500 x 700 nm	[89]
Chemical reduction of GO	Reduction agent: hydrazine Deoxygenation agent: KOH or NaOH Temperature: 50–90℃	Resistance of graphene paper: 7,200 S·m^{-1} Incomplete removal of oxygen	[90] [91]
	Reduction agent: bovine serum albumin Reduction agent: vitamin C Temperature: 95℃	Template for nanoparticle synthesis Film conductivity: up to 7,700 S·m^{-1}	[92] [93]
	Reduction *via* bacteria respiration Reduction agent: hydriodic acid and acetic acid	Resistance decreased up to 10^4 by reduction Sheet resistance: pellets dried after solution reduction: 30,400 S·m^{-1}	[94] [95]
	Reduction agent: hydriodic acid and acetic acid In solution at room temperature or in vapor at 40℃	Thin film after vapor reduction: 7,850 S·m^{-1} Formation of 1–4 layers of rGO	[96]
	Sonolytic reduction: ultrasonication at 211 kHz for 30 min Microwave-assisted reduction in the presence of hydrazine	Formation of 1–8 layers of rGO with size up to a few micrometers	[97]
Thermal reduction of GO	220℃ in air for 24 h 150℃ in DMF for 1 h	Film sheet resistance: 8 kΩ·sq^{-1} Film resistance: 6 kΩ	[98] [99]
Photothermal	High pressure Hg lamp with H_2 or N_2	Sheet size: ~1 μm	[100]

| reduction of GO | flow | Single-sheet conductivity: 2,000–20,000 S·m⁻¹ | |
| | Pulsed xenon flash | Sheet resistance of rGO area: ~9.5 kΩ·sq⁻¹ | [101] |

2. 2 Nanocomposite-Based Strain Sensors

Over a decade, there have been extensive investigations on the development of CNM-polymer nanocomposite strain sensors. For effective distributed sensing, nanomaterials must be uniformly dispersed within the matrix. Van der Waals interactions between nanotubes and graphene result in aggregates and stacks [102, 103]. Also, agglomeration is significant in chemical vapor deposition (CVD) grown multi-walled nanotubes because of nanoscale entanglement. For processing nanocomposites many approaches involve several steps that may include high speed mixing [104], high-energy sonication and solution-evaporation processing [67, 105], surfactant-assisted processing through formation of a colloidal intermediate [106], functionalization of nanotubes with the polymer matrix [107], and high shear mixing [108].

The coupling of physical properties with mechanical deformation particularly has widespread applications in the development of multi-functional materials for sensing and actuation. Of foremost importance in the development of sensors and actuators based on CNT composites is their electrical conductivity. Polymeric or ceramic matrix of composites is usually considered as non-conductive because of its extremely low electrical conductivity (in the order of 10^{-10}~10^{-15} S/m) [109]. Dispersing conductive materials into the nonconductive matrix can form conductive composites. The electrical conductivity of a composite is strongly dependent on the volume fraction of the conductive phase. At low volume fractions, the conductivity remains very close to the conductivity of the pure matrix. When a certain volume fraction is reached, the conductivity of the composite drastically increases by many orders of magnitude. The phenomenon is known as percolation and can be well explained by the percolation theory as shown in Fig. 1-1. The electrical percolation threshold of conductive reinforcements embedded in an insulating matrix is sensitive to the geometrical shape of the conductive phase. Small size and large aspect ratio tend to lower the percolation threshold. Because CNTs and graphene had tremendously large aspect ratios (100-10,000), many researchers have observed exceptionally low electrical percolation thresholds.

Sandler *et al*. [40] and Moisala *et al*. [41] have reported ultra-low percolation thresholds for multi-walled CNT composites, and Bryning *et al*. [42] reported very low percolation thresholds in single-walled nanotube composites. Stankovich *et al*. [103] reported the first graphene-polymer conductive composites, and it showed the lowest reported value of percolation for any carbon based composites, except CNT based composites. Thostenson *et al*. [26] examined the influence of nanoscale structure on the electrical properties of nanocomposites. In the case of graphene and graphene related composite materials, it is difficult to establish their correlations and general dependencies between polymer matrix, processing, filler shape and type. Using a calendering approach, nanocomposites were processed with a highly

dispersed structure and a partially agglomerated structure. For both structures the nanocomposites exhibit percolation thresholds below 0.1 wt.%. Depending on the matrix, the processing technique, and the nanomaterial type used, percolation thresholds ranging from 0.001 to more than 10 wt% have been reported.

Because of their several outstanding electrical properties, some of reports have proposed the use of CNM-based nanocomposites as conductometric vapor sensors [110, 111]. In these reports the changes in electrical resistivity of the composite are measured and are attributed to swelling of the polymer matrix and/or conductive modification due to the solvent absorption. It was noted by Yoon *et al*. [112] for CNT-polymer composite sensor and Bai *et al*. [113] for graphene-polymer composite sensor that the different gas concentrations diffuse into the polymer affects the distance between CNTs through polymer swelling. Wei *et al*. [114] demonstrated that their aligned nanotube composite arrays displayed similar changes in resistance when subjected to thermal or optical exposure. Again, the resistance changes are attributed to dimensional change of the nanocomposite, and they suggested that the composites could also be used as mechanical sensors.

In the area of resistance-based strain sensors, CNT nanocomposites were more intensively studied because of their longer history. Darhap *et al*. [115] investigated the use of thin films of randomly oriented CNTs and measured resistance changes using a four-point-probe. They noted a linear change in the sheet resistance when subjected to tension or compression. Zhang *et al*. [22] reported that multi-walled CNT-reinforced composites can be utilized as strain sensors. The sensitivity of their nanocomposite electrical conductivity to applied strain was reported to be 3.5 times higher than a traditional strain gage, and they suggested that the instantaneous change in resistance with strain can be utilized for self-diagnostics and real-time health monitoring. This piezoresistive behavior has also been demonstrated by Kang *et al*. [15] where single-walled nanotube–polymer composite films were utilized for strain sensing and examined their static and dynamic behavior. By extending the sensor to a long strip they created a ''neuron sensor'', and they suggested that a neural system in the form of a grid could be attached to the surface of a structure to form a sensor network, enabling structural health monitoring.

A change in volume due to mechanical loading directly results in resistance changes. In their review, Fiedler *et al*. [116] first proposed the concept of conductive modification with nanotubes as having potential for both strain and damage sensing. Electrical techniques have long been established as a non-invasive way to monitor damage in carbon fiber-reinforced composites under static and dynamic loading conditions. Because carbon fibers are conductive, fiber fracture results in changes in electrical resistance. This approach does not give much insight on matrix-dominated fracture mechanisms that affect durability and fatigue life, and is not applicable to composites with non-conducting fibers (*e.g.* glass or aramid fibers). Others have attempted to locally modify electrical properties of glass fiber yarn bundles through coating with carbon powder and utilize them for damage sensing.

Some of recent studies show the significance of CNT-polymer nanocomposite sensors as shown in

14

Fig. 2-3. Thostenson *et al*. [117] established that the change in the size of reinforcements, from conventional micron-sized fiber reinforcement to CNTs with nanometer-level diameters, enables unique opportunity for the creation of multi-functional *in situ* sensing capability. By combining these reinforcements of different scales, CNTs can penetrate the matrix-rich areas between fibers in individual bundles as well as between adjacent plies and can achieve a percolating nerve-like network of sensors throughout the arrays of fibers in a composite, as illustrated in Fig. 2-3 (a). This multi-scale composite shows not only capability of strain sensing but also detection of delamination of composite ply. More recently, Rein *et al*. [21] fabricated CNT buckypaper embedded epoxy composites and they showed high strain dependency of conductivity change with distinct signal patterns with different geometry of local defects as shown in Fig. 2-3 (b).
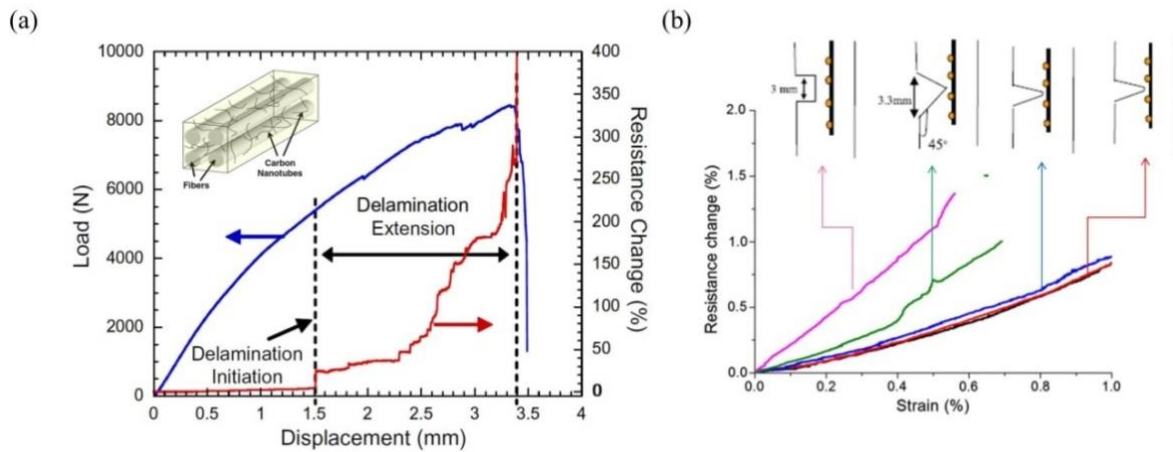
Figure 2-3 (a) Load/displacement and resistance response of a composite ply [88] and (b) Resistance change as a function of the total strain of the specimen for MWCNT BP in Polymer 1 in the presence of different defects [21].

To date, strain-induced effects on graphene have been studied for band-gap creation, magnetic property tuning, and band structure modification, which were treated at the atomic level [118-120]. Simply, measuring piezoresistivity of graphene-polymer composite was studied to analyze physical properties of strained graphene for strain sensors. More recently, however, applicability of small scale graphene polymer layer-by-layer composites were introduced and received attention because of their ease of patterning, simple assessment method and extremely high sensitivity. Lee *et al*. [121] first reported the piezoresistive response of a single layer of wafer-scale CVD-grown graphene on a PET substrate. Fu *et al*. [122] reported patterned graphene strain sensor with ultrahigh sensitivity. A recent report by Bae *et al*. [123] showed CVD-patterned graphene-polymer sensor with relatively less sensitive but more expanded measurable strain range and multi-dimensional strain sensing capability with specific graphene configuration called rosettes demonstrated its applicability to detect human body motion as shown in Fig. 2-4.
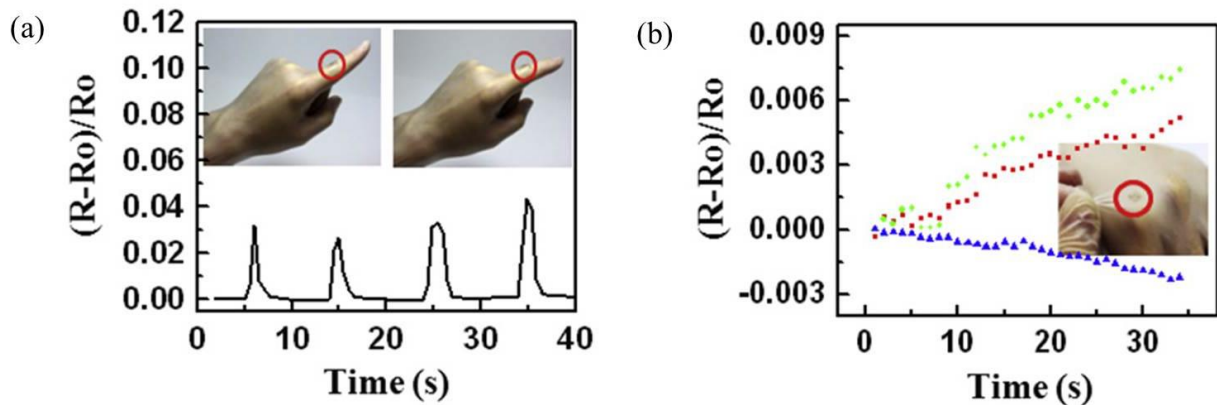
Figure 2-4 (a) Repeatedly increase and decrease in normalized resistance of graphene strain sensor mounted on finger of wearable glove (inset) with respect to monitoring the finger motion up and down. (b) Variation in normalized resistance with respect to time during stretching of graphene based Rosette gauge mounted on wearable glove [123].

2. 3 Structural Health Monitoring Using Piezoresistive Nanocomposites

Premature structural failure can lead to serious public safety and economic consequences [124]. Structural health monitoring (SHM) can play a critical role in preventing and mitigating the course of structural damage [125]. SHM has a clear role in virtually all structural engineering efforts. The traditional practice of SHM has involved visual inspection done by human, possibly with the aid of simple instruments, such as plumb lines and levels. This low-tech yet reliable technique has been highly successful for millennia. Despite more recent developments and applications of various nondestructive evaluation techniques based on such physics as ultrasound, eddy current, acoustic emission, X-ray, thermography, *etc*., they are still hindered by a large influence of human factor and the difficulties associated with automation. Modern SHM systems, which are characterized by permanently installed sensor network, the availability of information on structural state at arbitrary times, and automated assessment and prognostics, inevitably involve added expenses that need to be justified in terms of increased benefits to the owners and operators of structural systems.

Since it is often required that strain measurements be made over finite regions, size and effective dimension of the measured region have a large influence on the nature of measurement. Traditional point sensors are designed to measure a localized region sufficiently small to be considered a "point." Hence, it is often necessary to install these zero-dimensional sensors in an array to cover the targeted region to be monitored. Distributed sensors, however, is capable of measuring over large regions with effective dimensions greater than zero. Among the various types of distributed sensors, piezoresistive nanocomposite strain sensors have been studied in recent years [88]. The studies have been geared toward demonstrating the proof-of-concept of small scale, 1D strain sensing.

16

2. 3 Research Objectives

As nanocomposites offer high design flexibility due to a broad spectrum of design parameters, a systematic approach is necessary for optimizing the parameters to tailor the sensor performance, aided by an understanding of the underlying physics and chemistry of materials processing-structure-property relationships. Tailorability, scalability and embeddability are the required characteristics for such applications. Detailed research objectives of the proposed study are shown in Fig. 2-5.

The study will investigate the effects of the following factors on the piezoresistive behavior and strain performance of nanocomposites: (1) nanofiller geometry (1D fiber-like CNT, 2D platelet-like graphene, and hybrids); (2) matrix-nanofiller interface; and (3) nanofiller orientation. As for the study on the influences of nanofiller geometry, CNM-based freestanding sheets, such as buckypapers and graphene papers, can be used without the need to consider the effects of other experimental parameters that may arise from the complexities that often exist in heterogeneous materials. As shown in Fig. 2-5 (a), buckypapers and CNT-graphene hybrid sheets can be simply fabricated *via* vacuum filtration with different CNM geometries and CNT : graphene ratios [126, 127]. The freestanding CNM sheets will be installed in the multi-point strain sensing system to demonstrate 2D strain sensing capability. A further study will be conducted on the strain sensing performance of polymer-impregnated freestanding CNM sheets, which provide added benefits of easy material handling and tailored properties.

Limited deformation is expected in CNMs due to poor stress transfer from the polymer matrix to the nanofillers, caused not only by the large elastic mismatch between CNMs and polymer but also by the weak interfacial bonding [128]. In most research on CNT- and graphene-based composite sensors, it has been shown that the stronger the interfacial bonding between matrix and CNMs, the higher the sensitivity [129]. However, many difficulties still remain in quantifying the effects of interfacial strength on piezoresistive behavior. For CNT-polymer composites, numerical modeling often has been employed to predict the electrical conductivity without consideration of the interfacial bonding and electrical properties of polymer matrix to minimize the minor variable [130]. However, experimental studies have shown that although interfacial bonding has a minor influence on the electrical conductivities of CNT-polymer composites, it has a significant effect on the piezoresistive behavior. In this regard, it is necessary to design a proper experimental method for quantitative investigation of interfacial adhesion effect. A simple, layer-by-layer coated 2D film model is ideal for this task. Therefore, reduced graphene oxide (rGO) has been selected to coat the top surface of a polymer substrate to enable the formation of distributed conductive network over a large contact area taking advantage of the 2D morphology. Using polydopamine, rGO can easily be functionalized by noncovalent hydrogen bonding and be expected to show the best performance with PVA matrix because of their abundant hydroxyl pendant groups. This water-absorbable conductive material is a great candidate for the conductometric humidity sensor.

Because the viscoelastic nature and limited maximum compressive strain of polymer, it is difficult to design CNM based sensor with compressive strain sensing capability. Soft and easily compressible

polymers such as silicon rubber or polyurethane can be used as polymer matrix for such application. However, theses rubbers and elastomers usually behaves as nonlinear mechanical characteristic and having high Poisson's ratio hence interpretation of its signal is came with high degree of uncertainty. Therefore, we demonstrated GO-based supramolecular hydrogels with ethylene diamine (EDA) and ascorbic acid (Vitamine C, VC) functional groups *via* hydrothermal self-assembly. The main aim of this study is to confirm their validity of porous CNM structure as sensory materials under compressive deformation and identify their relation between the controlled porosity and piezoresistive behavior.

By combining the results from the above-mentioned systematic approaches, it is expected that quantitative relationships between experimental parameters and performance will be identified, thereby enabling the optimal design of structural sensing systems for various applications.
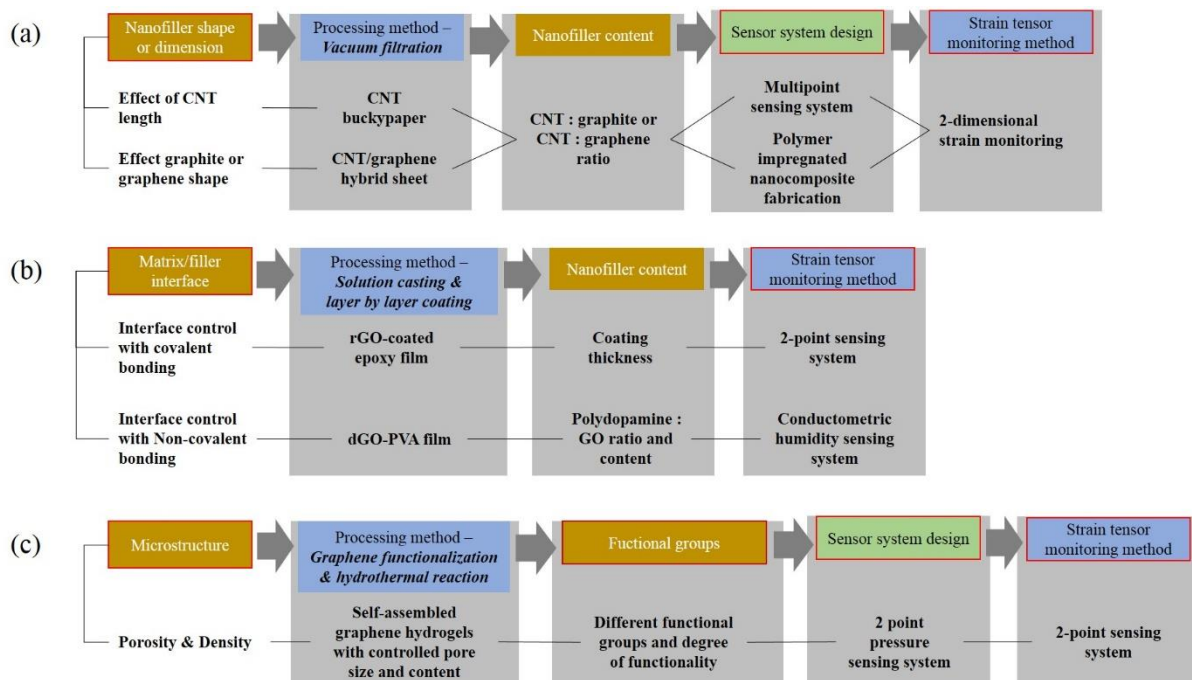
Figure 2-5 Systematic approach and experimental design for the quantitative study of various parameters on strain sensor performance

III. EXPERIMENTAL AND MATERIALS OVERVIEW

3. 1 Experimental Design – Overview

As shown in Fig. 3-1, CNTs (2 types), xGnPs (3 types) and GO were selectively used to fabricate different types of resultants and each resultants were used to study their effect on piezoresistive behavior. Hybrid freestanding sheets were fabricated *via* vacuum filtration. Because of their structural characteristics, the effects of nanomaterial shape on the piezoresistive behavior can be shown without other possible effects of interfacial characteristic and nanomaterial alignment. Further studies were performed with the piezoresistive behavior of polymer nanocomposites based on CNM freestanding films. Because of their morphological and chemical characteristics, rGO is an ideal material to be functionalized both covalently and noncovalently. The effects of interfacial bonding on piezoresistive behavior and humidity sensitivity was studied using rGO-polymer composite films with different forms of rGO, i.e., rGO uniformly dispersed in the polymer and rGO coated on a polymeric substrate. Conducting cylindrical structure of sponge-like graphene hydrogels were prepared using ethylenediamine and ascorbic acid functionalized GO *via* hydrothermal method and their piezoresistive behavior under compressive strain was studied. With different types of crosslinking agent and crosslinking density, the microstructures of hydrogels were controlled and their effect on piezoresistive behavior was studied. These experimental procedures are simplified and organized in Fig. 3-1 and detailed procedures will be presented from Chapters 4 to 7.
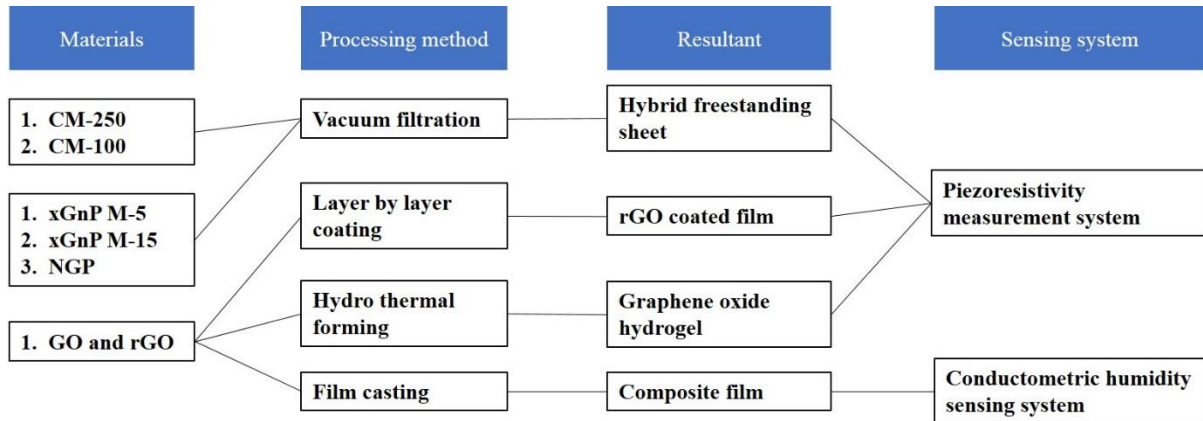
Figure 3-1 Experimental procedure overview

3. 2 Materials

3. 2. 1 Multi-walled Carbon Nanotubes

MWCNTs, grown by chemical vapor deposition, with a purity rating of >95%, 5–10 nm inner diameter, 60–100 nm outer diameter, and two different lengths - 100 μm (CM-100) and 250 μm (CM-

250) - were purchased from Hanwha Chemical. Their bulk density is around ~0.1 g·cm^{-2} (CM-100) and ~0.02g·cm^{-2} (CM-250). They were synthesized by catalytic CVD process and it has about 90 wt.% purity without any purification. Their enhanced conductivity and dispersibility make them suitable for conductive composite applications.

3. 2. 2 Exfoliated Graphite Nanoplatelets

Two types of grade M xGnP with average lateral dimensions of 5 μm (M-5) and 15 μm (M-15) were purchased from XG Sciences. Grade M particles have an average thickness of approximately ~9 (M-15) and 18 nm (M-5) and typical surface area of 120 – 150 m^2·g^{-1}. These dark grey powders show bulk density of 0.03 – 0.1 g·cm^{-3} and oxygen content less than 1 wt.%.

Nanographene platelets (NGPs) with a documented average lateral dimension of <10 μm, average thickness of <1 nm, oxygen content of <2.1%, and surface area of 400–800 m^2/g were purchased from Angstron Materials..

The transmission electron microscopy (TEM) and scanning electron microscopy (SEM) images of as-received xGnPs and NGP particles showed high aspect ratios (Fig. 3-2 (a–c)). The lateral dimensions of M-5 and M-15 were ~5 and ~15 μm, respectively, while the thicknesses were ~16 and ~9 nm, respectively. In the case of NGP, lateral dimension (>2 μm) and thickness (>5 nm) were much smaller than those of xGnPs. Hence, the aspect ratios of M-5 and M-15 were calculated as ~313 and ~1667, respectively, while that of NGP was calculated as 400.

Fig. 3-2 (d) shows the Raman spectra of M-5, M-15 and NGP. Small D band and sharp G band peaks confirm the sp^2-type bonding of the carbon atoms in the basal plane of M grade xGnPs and minimal defect in the graphitic structure. It is thus believed that the acid intercalation and subsequent pulverization, involved during the M grade xGnP manufacturing process, did not oxidize the surface of the xGnP, which would degrade the electrical and mechanical properties of an individual platelet. However, much larger I_D/I_G ratio was observed from NGP, which may be due to more destructive intercalation and pulverization processes as compared to M grade xGnPs. In addition, the region of Raman spectra from 1500 to 1650 cm^{-1} shows red shift of G band from M-5 to M-15 to NGP, indicative of decreases in thickness, as confirmed by TEM analyses.
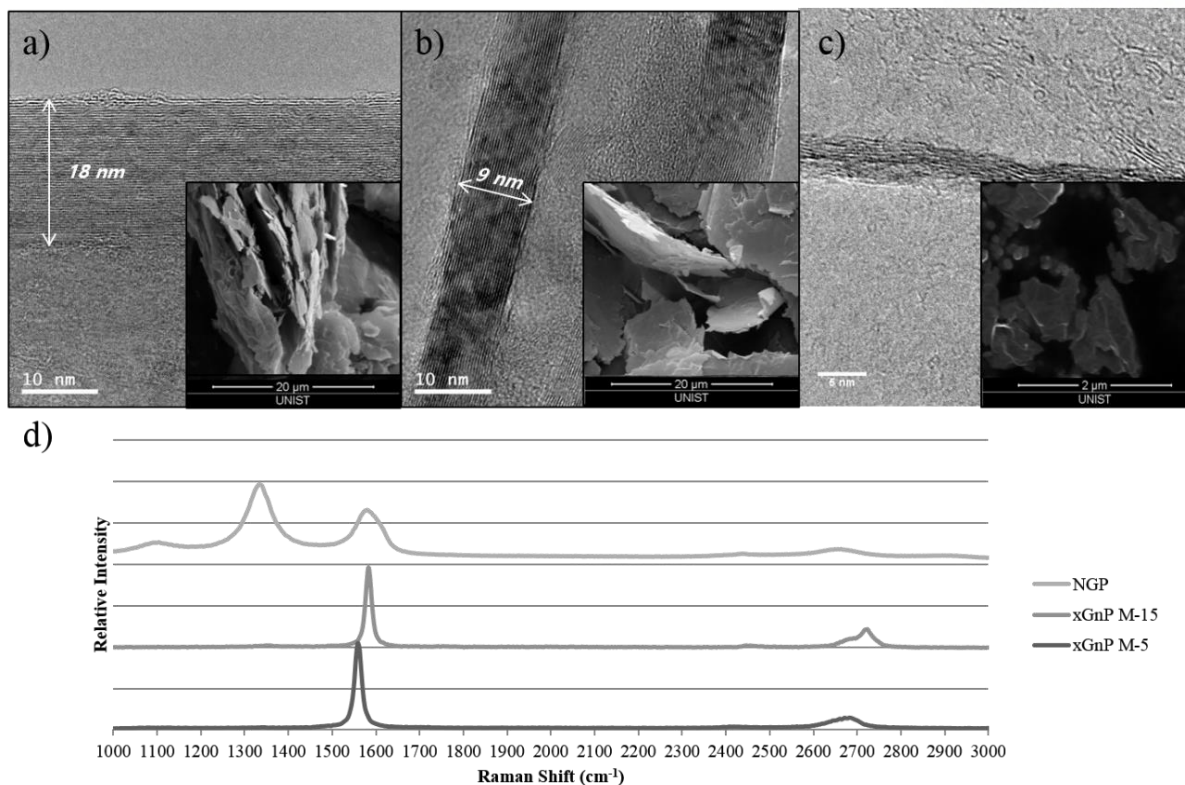
Figure 3-2 Typical SEM and TEM micrographs of the surface and the cross sectional view of xGnPs ((a) M-5, (b) M-15) and (c) NGP, respectively. (d) Raman spectra of as-received xGnPs and NGP.

3. 2. 3 Graphene Oxide

Graphite oxide was prepared from purified natural graphite (SP-1, Bay Carbon) using the modified Hummer's method. The graphite powder (2.0 g) was put into a solution of concentrated H_2SO_4 (3.0 mL), $K_2S_2O_8$ (1.0 g), and P_2O_5 (1.0 g) at 80 ℃. The resultant dark blue mixture was allowed to cool to room temperature over a period of 6 h and was then carefully diluted with distilled water, filtered, and washed on the filter until the pH of the rinse water became neutral. The product was dried in air at ambient conditions overnight. This preoxidized graphite was then subjected to oxidation by the Hummers method. The preoxidized graphite powder (2.0 g) was added to concentrated H_2SO_4 (46 mL) and $KMnO_4$ (6.0 g) was added gradually with stirring and cooling, while the temperature of the mixture was maintained below 20 ℃. The mixture was then stirred at 35 ℃ for 2 h, and distilled water (92 mL) was added. After 15 min, the reaction was terminated by the addition of a large amount of distilled water (280 mL) and a 30% H_2O_2 solution (5.0 mL), after which the color of the mixture changed from black to bright yellow. The mixture was filtered and washed with a 1:10 HCl solution (500 mL) in order to remove metal ions. The graphite oxide product was suspended in distilled water to give a viscous, brown dispersion, which was subjected to dialysis to completely remove metal ions and acids. To obtain the GO dispersion, graphite oxide was exfoliated by treatment with a mechanical homogenizer at 15,000 rpm for 15 min, followed by sonication (ultrasonic cleaner, 100 W, Branson) for 15 min and then centrifugation at 4,000 rpm for 10 min.

IV.PART 1. MULTIWALLED CARBON NANOTUBE – EXFOLIATED GRAPHITE NANOPLATELET HYBRID SHEETS

4. 1 Part Introduction

To date, many studies had been reported on the electromechanical characteristics of CNT buckypapers [15, 21, 115], CNT-polymer composites [24, 131, 132] and graphene–polymer composites [18, 133] for strain sensing. Recently, Li *et al*. [134] reported that CNT films can be used as strain sensors at the macroscale due to the dependence of the electrical properties of the SWCNT films on mechanical deformation at the nanoscale. Hu *et al*. [14] exclusively studied the strain sensitivity of the CNT-polymer composites based on the statistical resistive network using theoretical and experimental results. More recently, Eswaraiah *et al*. [133] demonstrated the real-time strain response of functionalized graphene-polyvinylidene floride (PVDF) nanocomposites at the macroscale under tensile loads and the use of these nanocomposites as strain sensors.

Similar to CNT and graphene nanocomposites, xGnP and GO can be dispersed in selected polymer matrices to yield composite materials with preferred properties [135, 136]. xGnP- or GO-based polymer composites exhibit outstanding thermal, electrical and mechanical characteristics. The graphitic nanostructured particles were ''hybridized'' with CNTs and were mainly studied as functional materials for particular applications, such as supercapacitors [137], transparent electrodes [138, 139], catalyst supports [140, 141], field emission devices [142, 143], chemical sensors [144] and photonic applications [145]. The knowledge of synergistic effect was obtained from the recent electrochemical study of ''hybrid films,'' while their effects on electromechanical properties, more specifically piezoresistive behavior, are still illusive.

In this part, we present a novel hybrid composite for efficient wide-area strain sensing, utilizing various combinations of size and length of xGnPs, NGPs and CNTs that form freestanding sheets, which are subsequently impregnated with polycarbonate by vacuum filtration. The aim of the presented work is to study the interactions between 2D platelet-like xGnPs and NGPs and 1D fiber-like CNT, and their effects on the electromechanical properties of the composite sheets. The feasibility of widearea strain sensing was studied employing multi-probe resistivity monitoring under flexural loading.

4. 2 Experimental

4. 2. 1 Preparation of MWCNT – xGnP Hybrid Sheets and Polymer Impregnation

Surfactants were dissolved in methyl alcohol with a concentration of 0.05 wt.%. 120 mg of MWCNTs, MWCNT/xGnP mixture with various types and content of MWCNTs, xGnPs were dispersed in 2 L of surfactant-methyl alcohol solution. After an hour of stirring and 3 h of sonication in a bath type sonicator, the solutions were further treated for 2 h with a horn-type sonicator. A nylon membrane

(0.45 μm pore size, Millipore) was used to make freestanding papers by vacuum filtration. Two liters of carbon nanomaterial suspension was filtered to make one 78-mm-diameter paper with a thickness of 60–80 μm. The paper was then washed with methanol and acetone to remove residual surfactants and then placed in an oven and dried at 60 ℃ overnight before being peeled off from the membrane. The constituents of carbon nanomaterial sheets effectively determine their microstructure and properties, and the types and surface areas of the sheets produced are specified in the Table 4-1. As shown in Fig. 4-1 (a), the dried buckypapers (BPs) and hybrid sheets (HSs) were placed between two sheets of 85-mm-diameter PTFE membrane filter (0.45 μm pore size, Airtech) and vacuum infiltrated with 150 mL of PC-chloroform solution (55 g·L^{-1}). Finally, the PC-impregnated BP and HS were dried in an oven overnight at 70 ℃. Fig. 4-1(b and c) shows the digital images of CM-250/M-5 HS before and after PC impregnation, which show high flexibility. Carbon nanomaterial (filler) contents in PC-impregnated composite sheets were measured by weighing the BP and HS before and after PC impregnation. The compositions of all the composite sheets fabricated are summarized in Table 4-2.
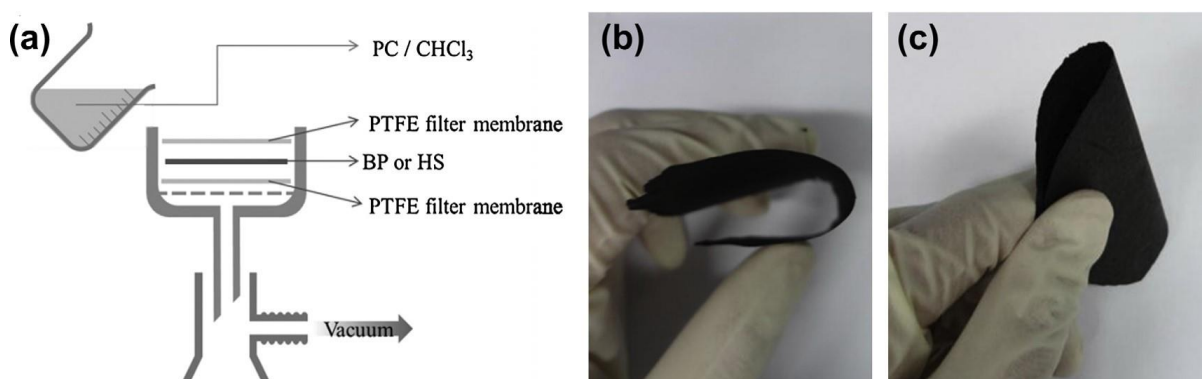
Figure 4-1 (a) Schematic diagram of PC impregnation process and digital images of HS (CM-250/M-5) (b) before and (c) after polymer impregnation.

Table 4-6 Specific surface areas (A_{BETs}) of buckypapers and hybrid sheets.

Material type	Sample name	xGnP or NGP content (wt.%)	A_{BET} (m^2/g)
CM-250	CM-250	0	210.0
CM-250 & M-5[a]	CM-250/M-5 (8:2)	20	197.2
	CM-250/M-5 (5:5)	50	157.2
	CM-250/M-5 (3:7)	70	121.3
CM-250 & M-15[a]	CM-250/M-15 (8:2)	20	-
	CM-250/M-15 (5:5)	50	109.4[c]
	CM-250/M-15 (3:7)	70	-
CM-250 & NGP[b]	CM-250/NGP (8:2)	20	273.8
	CM-250/NGP (7:3)	30	324.2
	CM-250/NGP (6:4)	40	349.8

Material type	Sample name	Filler content (wt.%)	A_{BET}
	CM-250/NGP (5:5)	50	375.3
CM-100	CM-100	0	197.2
CM-100 & M-5[a]	CM-100/M-5 (8:2)	20	-
	CM-100/M-5 (5:5)	50	147.8[c]
	CM-100/M-5 (3:7)	70	-
CM-100 & M-15[a]	CM-100/M-15 (8:2)	20	-
	CM-100/M-15 (5:5)	50	101.6[c]
	CM-100/M-15 (3:7)	70	-
CM-100 & NGP[b]	CM-100/NGP (8:2)	20	-
	CM-100/NGP (7:3)	30	-
	CM-100/NGP (6:4)	40	-
	CM-100/NGP (5:5)	50	381.3[c]

[a] 70 wt.% was the highest M grade xGnPs content achievable.
[b] 50 wt.% was the highest NGP content achievable.
[c] Selected hybrid sheets (MWCNT:xGnP/NGP = 5:5) for A_{BET} comparison purposes.

Table 4-7 Filler compositions in PC-BP and PC-HS composite sheets.

Material type	Sample name	Filler content in PC-HS (wt.%)
CM-250	PC-CM-250	59.6
CM-250/M-5[a]	PC-CM-250/M-5 (8:2)	62.4
	PC-CM-250/M-5 (5:5)	64.9
	PC-CM-250/M-5 (3:7)	71.4
CM-250/M-15[a]	PC-CM-250/M-15 (8:2)	65.2
	PC-CM-250/M-15 (5:5)	71.3
	PC-CM-250/M-15 (3:7)	75.3
CM-250/NGP[b]	PC-CM-250/NGP (8:2)	69.3
	PC-CM-250/NGP (7:3)	76.3
	PC-CM-250/NGP (6:4)	81.3
	PC-CM-250/NGP (5:5)	81.3
CM-100	PC-CM-250	61.3
CM-100/M-5[a]	PC-CM-250/M-5 (8:2)	63.4
	PC-CM-250/M-5 (5:5)	69.3
	PC-CM-250/M-5 (3:7)	75.3
CM-100/M-15[a]	PC-CM-250/M-15 (8:2)	65.2
	PC-CM-250/M-15 (5:5)	71.3
	PC-CM-250/M-15 (3:7)	72.2
CM-100/NGP[b]	PC-CM-250/NGP (8:2)	70.5
	PC-CM-250/NGP (7:3)	70.2
	PC-CM-250/NGP (6:4)	74.8

PC-CM-250/NGP (5:5)	79.7

[a] 70 wt.% was the highest M-5 or M-15 content achievable.
[b] 50 wt.% was the highest NGP content achievable.

4. 2. 2 Characterization

The surface areas of as-received MWCNTs and xGnPs were measured using a w surface area analyzer (Micromeritics ASAP 2020) using N_2 adsorption at 77 K. The tensile properties of PC-impregnated BP and HS composites were obtained using a dynamic mechanical analyzer (DMA, TA Instruments Q800), operated in quasi-static mode at room temperature. The specimens measuring 30 mm by 6 mm were cut from 60 to 80 μm thick (as measured by a thickness measuring system (KMAC)) nanocomposite sheets using a laser cutting system (VersaLaser VLS2.30). The gage length was 15 mm, and the tensile load was applied at a rate of 2 mm·min^{-1}. Five specimens were tested for each sample and were used to obtain the average tensile modulus, tensile strength, and % elongation to failure. Composite sheets were cut into 50 mm by 50 mm squares and glued to 10-mm-thick PMMA plates using an epoxy adhesive, as shown in Fig. 4- 2 (a). Eight electrodes were attached on the periphery of the square film using a silver paste and were connected to an electrical signal acquisition system consisting of Keithley 2002 multi-meter and 7001/7012-S switching system. The composite-sheet-bonded PMMA plates were subjected to three-point bending using a universal materials testing system (Instron 5982), as shown in Fig. 4- 2 (b), and piezoresistivity was measured in situ. A maximum flexural strain of 2% was applied at a strain rate of 1% ·min^{-1}.
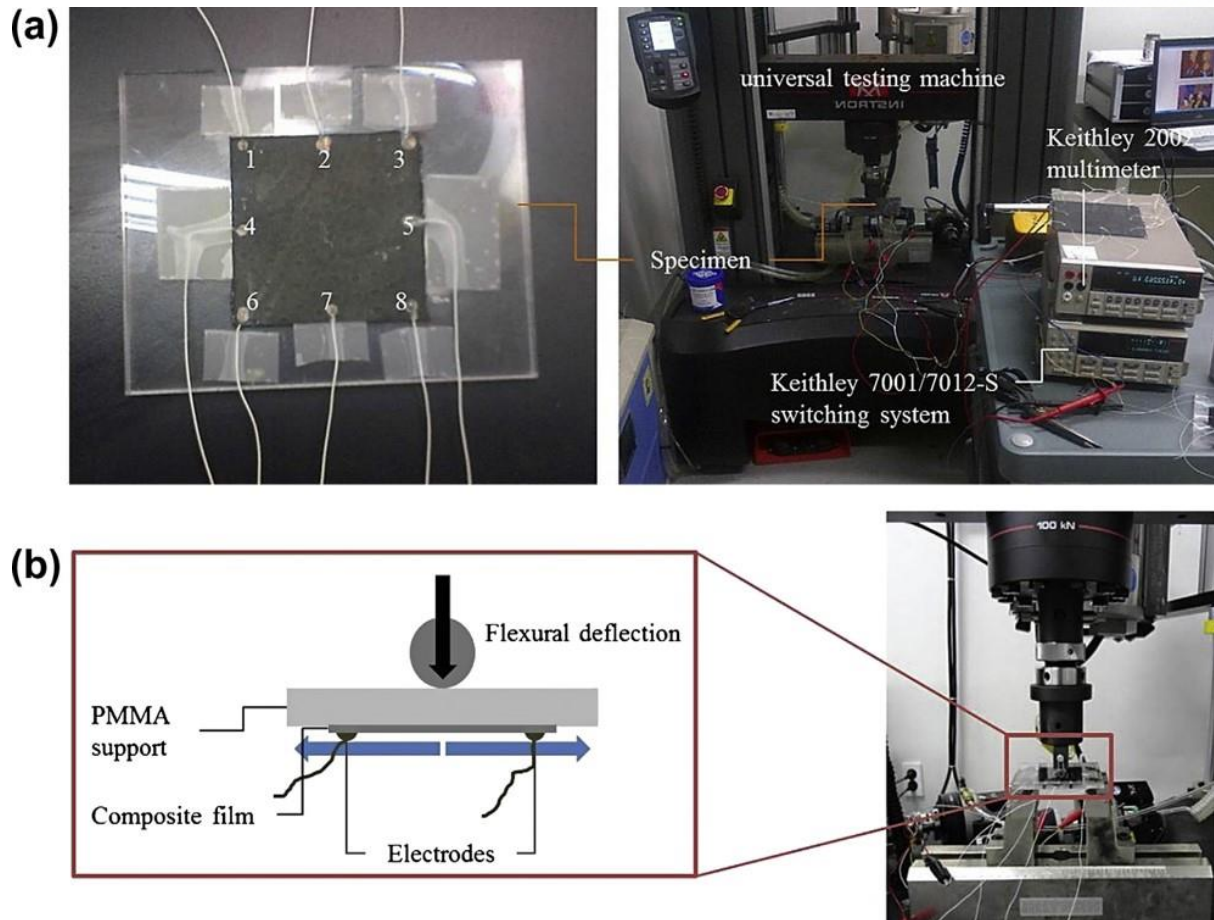
Figure 4-2 (a) Electromechanical behavior measurement setup and (b) mechanism of tensile strain generation in PC-HS composite sheets bonded to a PMMA plate subjected to three-point bending.

4. 3 Results and Discussion

4. 3. 1 Microstructure and Morphology

Table 4-1 summarizes the eight different sets of buckypapers and hybrid sheets prepared for this study. The sample sets and names are based on the combination of MWCNT and xGnP types and the MWCNT:xGnP ratio in hybrid sheets. The specific surface areas of buckypapers and selected hybrid sheets, denoted as A_{BET}, are also shown in Table 4-1. The reported specific surface area of MWCNT buckypaper is around 200 $m^2 \cdot g^{-1}$, and our measurement showed similar values for the buckypapers of both CNT lengths. From the BET measurement, it is evident that buckypapers have much higher surface areas than MWCNT–xGnP hybrid sheets because of the one-dimensional structure, unique morphology and nanoscale size of CNTs. The measured A_{BET} of xGnP M-5 and M-15 was around 90 and 70 $m^2 \cdot g^{-1}$, respectively. The measured A_{BET} of NGP was around 400 $m^2 \cdot g^{-1}$, and therefore, the A_{BET}

It is noted in Fig. 4-3 (a) and (d) that xGnP hybrid sheets are macroscopically robust under flexural stress, as they can be almost folded without failure. Fig. 4-3 (b), (c), (e) and (f) show the basal plane morphologies of the CM-250/M-5 and CM-250/NGP hybrid sheets before and after stretching. In Fig.

26

4-3 (c) and (f), the MWCNT bridging suggests that the surface adhesion between MWCNT and xGnP is very strong because of the van der Waals interactions and π–π interactions of sp^2 carbon atoms.
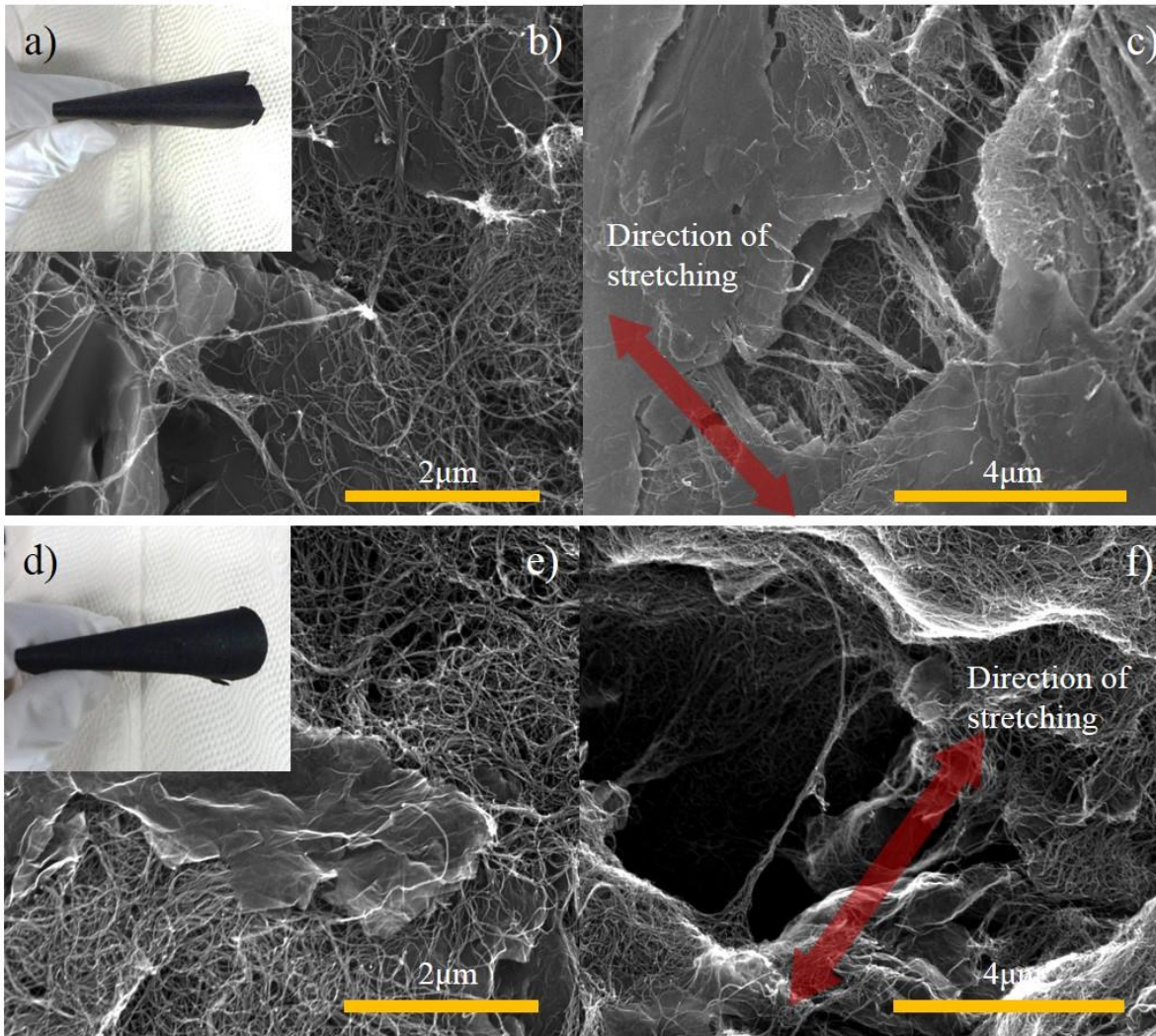
Figure 4-3 Digital photographs and SEM images of CM-250/M-5 (5:5) hybrid sheet ((a)–(c)) and CM-250/NGP (5:5) hybrid sheet ((d)–(f)). (a), (c) Digital photographs upon folding. (b), (e) SEM images of hybrid sheet surface. (c), (f) SEM images of crack morphology in hybrid sheets with in-plane tension.

The morphologies of the fracture surfaces of PC-impregnated BP and HS as observed with the SEM are shown in Fig. 4-4. The low magnification images of PC-CM-250/M-5 and PC-CM-250/M-15 show anisotropic fracture morphologies, that is, xGnPs shows flow-induced alignment in the filtration (or through-thickness) direction (Fig. 4-4 (c and e)), while PC-BP shows transversely orthotropic or in-plane isotropic morphologies (Fig. 4-4 (a)). From the SEM images of PC-CM-250/NGP (Fig. 4-4 (g and h)), large voids that continuously surround the impregnated CM-250/NGP region can be observed, indicative of relatively high nanofiller content as confirmed in Table 4-2, which may lead to lower structural robustness under deflection. Thus, it is believed that the NGP agglomerates, produced as a result of its relatively poor dispersity, lead to loose interconnection with CNTs and large pore size in

hybrid sheets, as compared to xGnPs. From high-magnification images, PC-CM-250/M-5 and PC-CM-250/M-15 composite sheets exhibit relatively high void contents as compared to PC-CM-250 composite sheet, which may be attributed to the restriction of PC solution flow imposed by the vertically aligned xGnPs and partially by the xGnPs pulled out during fracture (Fig. 4-4 (d and f)).
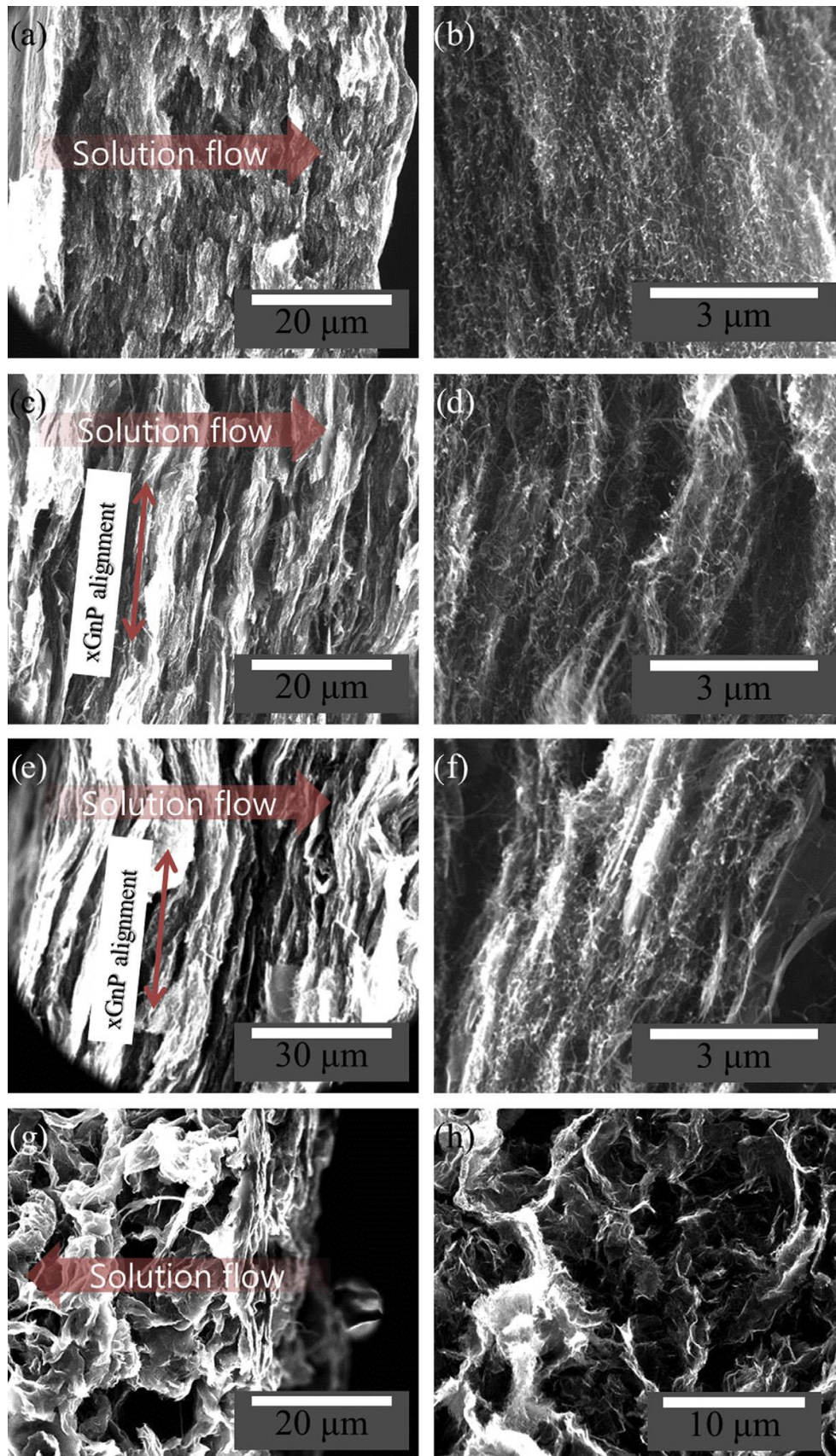
Figure 4 - 4 SEM images of fracture surfaces of PC-impregnated BP and HS: (a) low- and (b) high-magnification images of PC-BP; (c) low- and (d) high-magnification images of PC-CM-250/M-5; (e) low- and (f) high-magnification images of PC-CM-250/M-15; (g) low- and (h) high-magnification images of PC-CM-250/NGP.

4. 3. 2 Tensile Properties

The tensile properties of MWCNT/xGnP hybrid sheets at 5:5 content ratio are shown in Fig. 4-5 (a). The tensile modulus of the CM-250 buckypaper was increased by 21% from 513 to 609 MPa with the addition of xGnP-M-5, while its tensile strength and elongation were decreased from 21.3 MPa and 6.3% to 14.3 MPa and 3.5%, respectively. Despite the fact that the aspect ratio of xGnP-M-15 is much higher than xGnP-M-5, the stiffening efficiency of xGnP in CM-250/M-15 hybrid sheet (only 2.5% improvement in tensile modulus as compared to CM-250 buckypaper) was lower than that in the CM-250/M-5 hybrid sheet. A similar trend is observed in CM-100/xGnP hybrid sheets. This suggests that the size effect, which can be translated into the specific surface area, is more dominant than the aspect ratio, for enhancement of tensile modulus, as the smaller size increases the volume of the interphase between xGnPs and the domain. The tensile moduli of the porous sheets studied are indicative of the packing densities of the carbon nanosheets, and the sheet strengths and elongations are governed by the interactions of carbon nanoparticles or domains. We can infer from the SEM images and BET results that the MWCNT bundles exhibit not only strong van der Waals and π–π interactions but also mechanical interlocking through entanglements. This results in the higher strength and elongation of buckypapers as compared to hybrid sheets. Although it is clear that xGnPs interfere with the interactions between MWCNTs, the small xGnP particles from sonication-induced damage fill the buckypaper pores, thus increasing the occupied volume and modulus.

Comparison of MWCNT/M-5 and MWCNT/NGP hybrid sheets at a 5:5 ratio revealed that inclusion of NGP in buckypaper significantly decreases its modulus by 57.4% from 513.1 to 218.3 MPa, its ultimate tensile strength by 71.9% from 21.3 to 6.0 MPa, and its maximum elongation by 95% from 6.3 to 0.3%. A similar trend is observed from the CM-100/NGP (5:5) hybrid sheet. This is attributed not only to weak interactions between CNTs and NGP particles, but also to the low packing density of the MWCNT/NGP hybrid sheet. It is elaborated by the combined results from the microstructure and degree of defects of as-received NGPs (Fig. 3-2 (c) and (d)) and the microstructure of the mechanically stretched MWCNT/NGP hybrid sheet (Fig. 4-3 (f)). Few-atom-thin NGP nanosheets are thermodynamically unstable, and their high specific surface area maximizes the van der Waals interactions, which results in re-aggregation of MWCNTs and NGPs in suspension, leading to a wrinkled morphology of the hybrid sheet. These pre-agglomerated domains are barely inter-connected for a robust free-standing hybrid sheet, as can be observed from Fig. 4-3 (f), which leads to deteriorated mechanical properties. In addition, we can easily imagine that the interactions between CNT and NGP particles are weaker than those between CNT and xGnP particles, due to the low crystallinity of NGPs, as confirmed from the Raman spectrum in figure 3-2 (d).

BPs and HSs are essentially porous materials, and therefore, impregnating them with polymers, such as PC, allows filling of the voids, effectively reinforcing and toughening the sheets. Fig. 4-5 (b)-(c) shows the tensile properties of PC-impregnated BP and HS composites. The tensile moduli of PC-

MWCNT/xGnP composite sheets (MWCNT:xGnP = 50:50 by weight) showed no apparent trend, ranging from 1.9 to 2.4 GPa (Fig. 4-5 (b)). On the contrary, the ultimate strength and maximum elongation of PC-HS composites showed clear dependency on CNT length and xGnP size. As compared to CM-100-based composite sheets, CM-250-based composite sheets showed higher strength and elongation, as the longer nanotubes allow more tightly interconnected network at the micro/nanoscale. As for M-5- and M-15-based composites, the former showed better impregnation quality, since M-5 has smaller lateral dimension as compared to M-15. Based on these reasons, the PC-CM-250 composite showed the highest ultimate tensile strength of 23.64 MPa and maximum elongation of 31.5%, while PC-CM-100/M-15 composite showed the lowest ultimate tensile strength of 14.12 MPa and maximum elongation of 11.3% among all the PC-MWCNT/xGnP composites considered. We discovered the mechanical properties of PC-MWCNT/NGP composite sheets suffered from the porous microstructure that resulted from carbon nanomaterial aggregates, as previously confirmed in the SEM images (Fig. 4-4 (g and h)). The tensile moduli of PC-CM-250/NGP and PC-CM-100/NGP composite sheets were 229 and 260 MPa, respectively, which are an order of magnitude lower than PC/MWCNT and PC-MWCNT/xGnP composite sheets. Similar trends were observed for ultimate tensile strength and maximum elongation. From Fig. 4-5 (c and d), we confirm that the mechanical properties suffer by increasing xGnP and NGP contents due to degraded impregnation quality and increased void content.
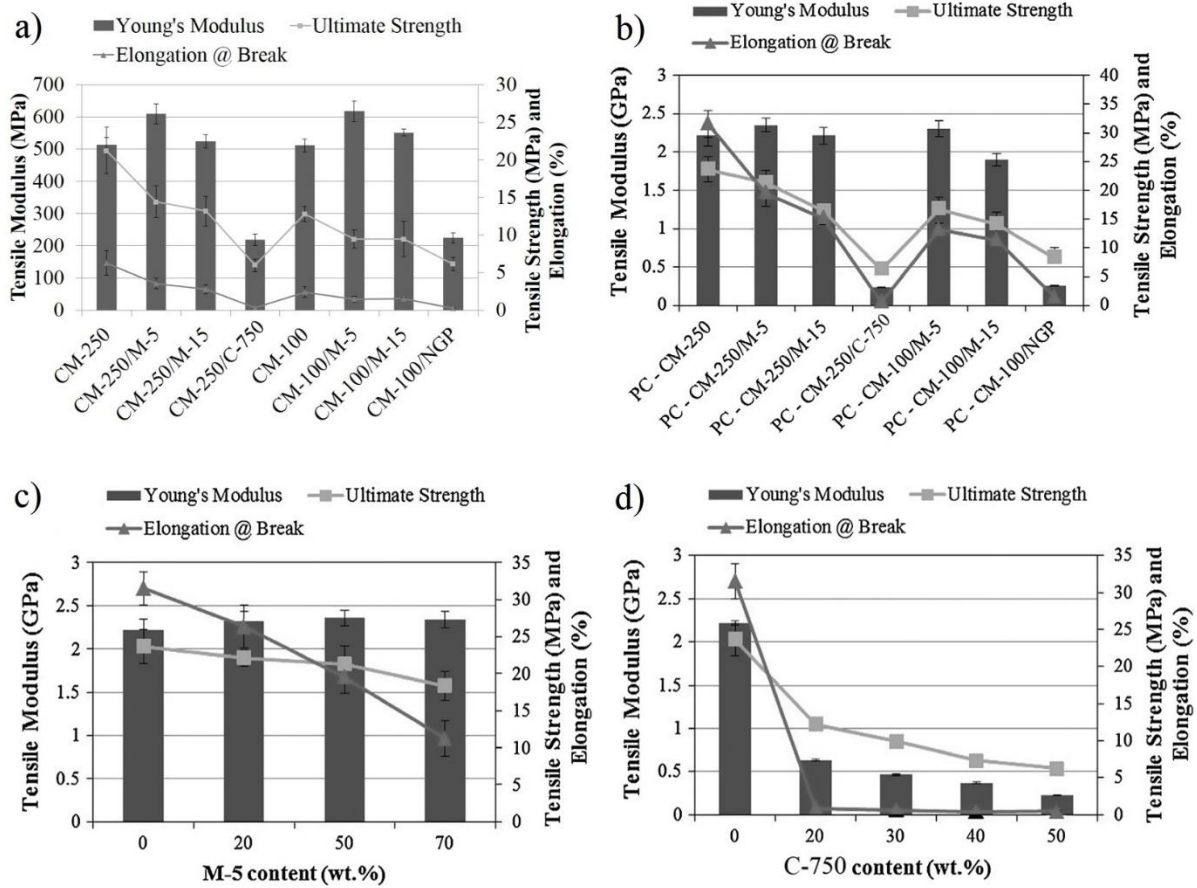
Figure 4-5 Tensile properties of (a) before PC impregnation and PC-BP and PC-HS with: (b) material types (at MWCNT:xGnP or MWCNT:NGP of 50:50), (c) PC-CM-250/M-5 and (d) PC-CM-250/NGP with varying M-5 and NGP content, respectively.

4. 3. 3 Electrical Resistivity

For the experimental study on piezoresistivity of hybrid sheets, eight electrodes were attached to the periphery of a hybrid sheet bonded to a PMMA plate as previously shown in Fig 1(a). The resistances were measured from all possible electrode pairs (a total of $C_8^2 = 28$ pairs) in sequence. In order to eliminate the inter-electrode distance dependence of the raw resistances measured, each resistance was divided by the distance between the corresponding electrodes as follows:

$$\bar{r}_{i,j} = \frac{R_{i,j}}{L_{i,j}} \tag{1}$$

Where $\bar{r}_{i,j}$ denotes the normalized resistance measured between electrodes i and j ($i, j = 1, 2, 3, \ldots, 8$), $R_{i,j}$ is the corresponding raw resistance measured and $L_{i,j}$ is the distance between electrodes i and j.

The normalized inter-electrode resistances were categorized into five distance groups, and selected values are plotted in Fig. 4-6. The averages and standard deviations of the normalized resistances of

various material combinations are summarized in table 4-3. Among all carbon nanomaterial sheet types, the CM-250 buckypaper shows the lowest average normalized inter-electrode resistance of 2.24 $\Omega \cdot cm^{-1}$ and standard deviation of 0.17 $\Omega \cdot cm^{-1}$, indicative of isotropic and homogeneous electrical properties. It can also be inferred that both xGnP-M-5 and M-15 were well dispersed in CM-250/M-5 and CM-250/M-15 hybrid sheets, suggested by low standard deviations of 0.20 and 0.22 $\Omega \cdot cm^{-1}$, respectively. However, the CM-250/NGP hybrid sheet shows a relatively high standard deviation of 0.51 $\Omega \cdot cm^{-1}$, suggesting less uniform dispersion of NGPs in the hybrid sheet.
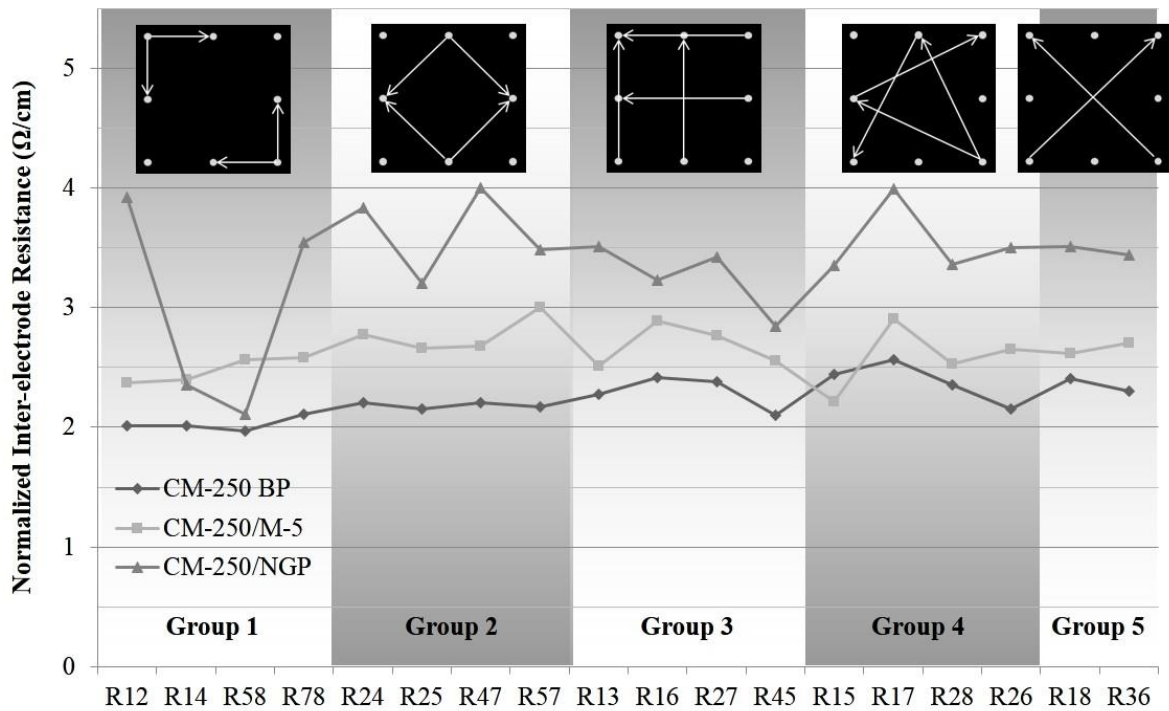
Figure 4-6 Effect of M-5 and NGP on the normalized inter-electrode resistance of hybrid sheets with each distance group at 50 wt% of M-5 and NGP loading.

Table 4-8 Average normalized inter-electrode resistances of hybrid sheets (MWCNT:xGnP = 5:5) and their standard deviations.

BP or HS type	Average inter-probe resistance ($\Omega \cdot cm^{-1}$)	Standard deviation ($\Omega \cdot cm^{-1}$)
CM-250	2.24	0.17
CM-250/M-5	2.63	0.20
CM-250/M-15	2.85	0.22
CM-250/NGP	3.37	0.51
CM-100	2.34	0.15
CM-100/M-5	2.63	0.24

4. 3. 4 Piezoresistive Behaviors

Electromechanical tests were performed with buckypapers and hybrid sheets with various material combinations and xGnP or NGP contents under cyclic flexural loading. For each electrode pair, the change in resistance was computed by comparing the resistances obtained from two consecutive measurement rounds, and was normalized by dividing it by the initial resistance and the physical distance between the electrodes as follows:

$$\overline{\Delta r_{i,j}} = \frac{1}{L_{i,j}} \frac{\Delta R_{i,j}}{(R_0)_{i,j}} \tag{2}$$

where $\overline{\Delta r_{i,j}}$ denotes the normalized change in resistance measured between electrodes i and j (i, j = 1, 2, 3, … , 8), $\Delta R_{i,j}$ is the corresponding change in resistance, $(R_0)_{i,j}$ is the initial resistance and $L_{i,j}$ is the distance between electrodes i and j.

As the PMMA plate undergoes three-point bending, the carbon nanomaterial sheet undergoes the same quasi-uniaxial tensile strain as the bottom surface of the plate, as shown in Fig. 4-2 (b). The normalized resistance change in each pair of electrodes shows orientation-dependent piezoresistive behavior led by the flexural-strain-induced stretching and disrupted conductive network (Fig. 4-3). Fig. 4-7 shows the orientation-dependent piezoresistive behavior of (a) CM-250 buckypaper, (b) CM-250/M-5 (5:5) hybrid sheet and (c) CM-250/NGP (5:5) hybrid sheet. The buckypaper and hybrid sheets exhibit different percentage changes in resistance in longitudinal (between electrodes 4 and 5), transverse (between electrodes 2 and 7) and diagonal (between electrodes 1 and 8) directions. The percentage change in resistance is greatest in the longitudinal direction, as it is aligned in the direction of maximum tensile strain in the PMMA plate. On the contrary, negligible and intermediate percentage changes in resistance are observed in the transverse and diagonal directions, respectively, which is in accordance with the relative in-plane strains generated in the carbon nanomaterial sheets. It can be observed that hybrid sheets show a higher percentage change in resistance than that of buckypaper at the same strain level, which indicates the difference in the strain sensitivity, as hybrid sheets have a relatively loose inter-connected conductive network as compared to buckypapers. In addition, at 1% strain, the CM-250/NGP (5:5) hybrid sheet shows 27% higher percentage change in resistance than the CM-250/M-5 (5:5) hybrid sheet. The effects of M-5 and NGP content on the piezoresistivity of CM-250-based hybrid sheets are shown in figure 4-8. Both CM-250/M-5 and CM-250/NGP hybrid sheets show increasing percentage changes in resistance with increasing M-5 and NGP content. This is due to the fact that as the xGnP content increases, the conductive network in the hybrid sheet becomes more loosely bound, thus reducing its robustness and therefore increasing the sensitivity.
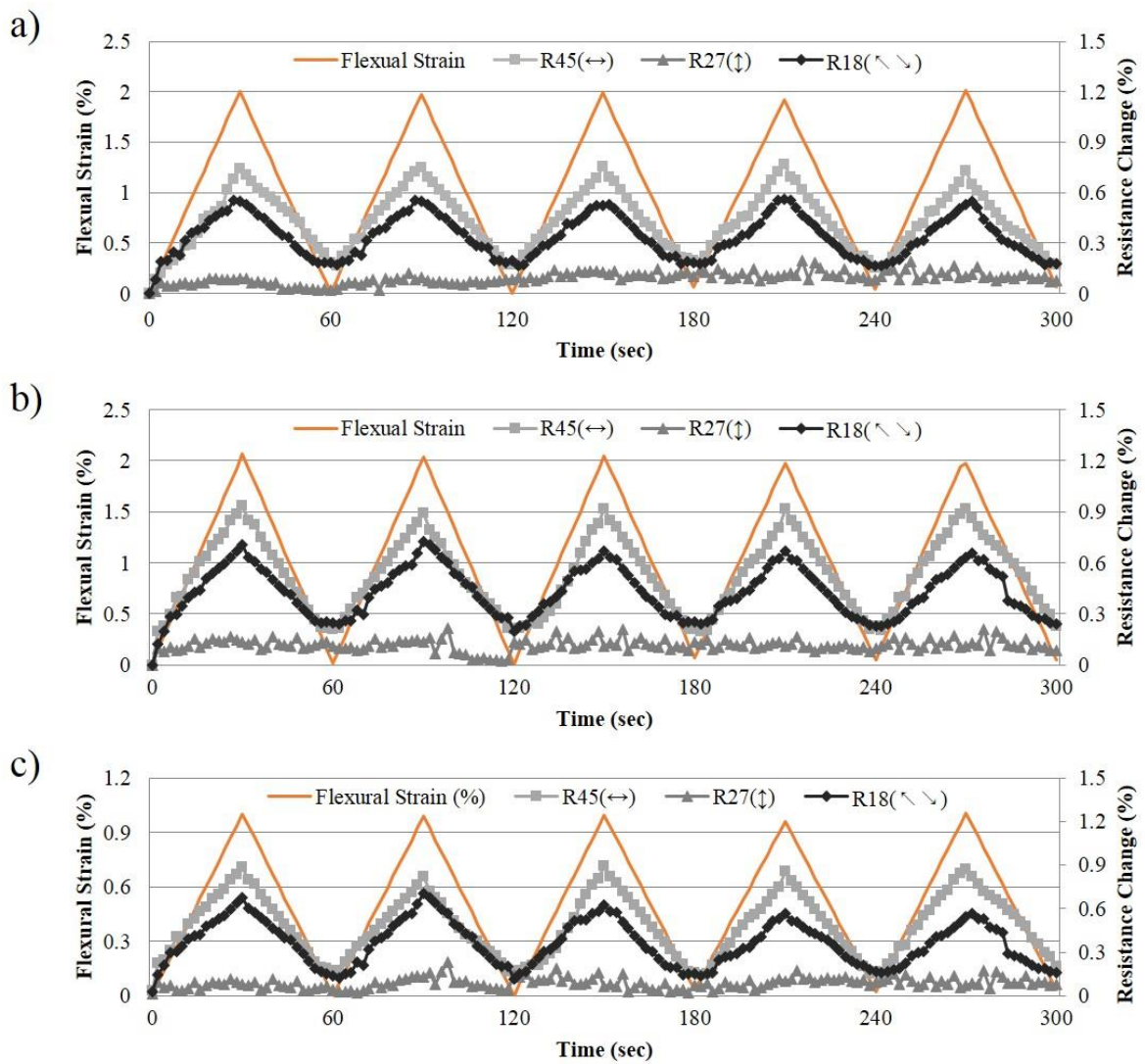
Figure 4-7 Resistance change in: (a) CM-250 buckypaper; (b) CM-250=M-5 (5:5) hybrid sheet; (c) CM-250=NGP (5:5) hybrid sheet under cyclic flexural strain. ('R45' denotes resistance between electrodes 4 and 5, and so forth.)

35
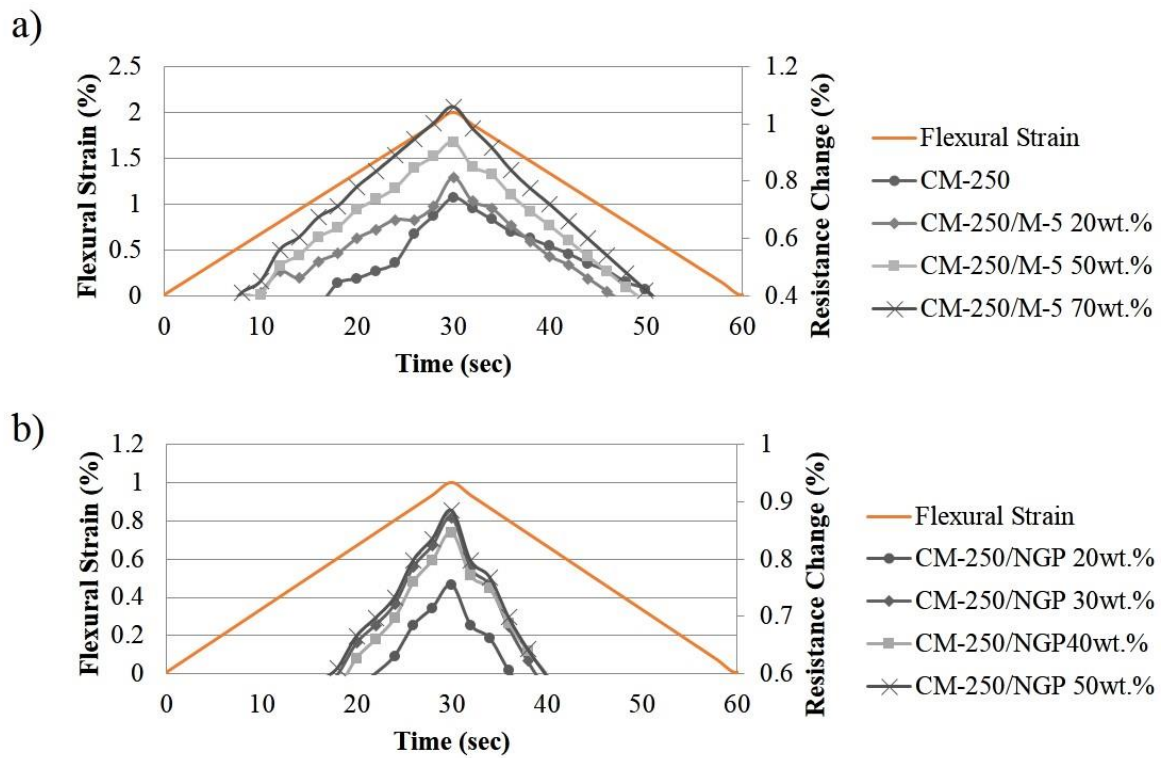
Figure 4-8 Effects of M-5 and NGP content on piezoresistivity in the longitudinal direction (R45) of CM-250-based hybrid sheets: (a) CM-250/M-5 hybrid sheets; (b) CM-250/NGP hybrid sheets.

The differences in the sensitivity of MWCNT buckypaper and MWCNT–xGnP hybrid sheets can be further elucidated by the schematic shown in Fig. 4-9. At the same MWCNT : xGnP ratio, the MWCNT–M-5 hybrid sheet shows higher sensitivity than the MWCNT– NGP hybrid sheet because of the large domains formed by pre-aggregated NGP particles. The larger the particle or domain size, the more easily the conductive network gets disrupted by external strains. On the other hand, fiber-type MWCNTs form a much more robust conductive network, which results in lower strain sensitivity.
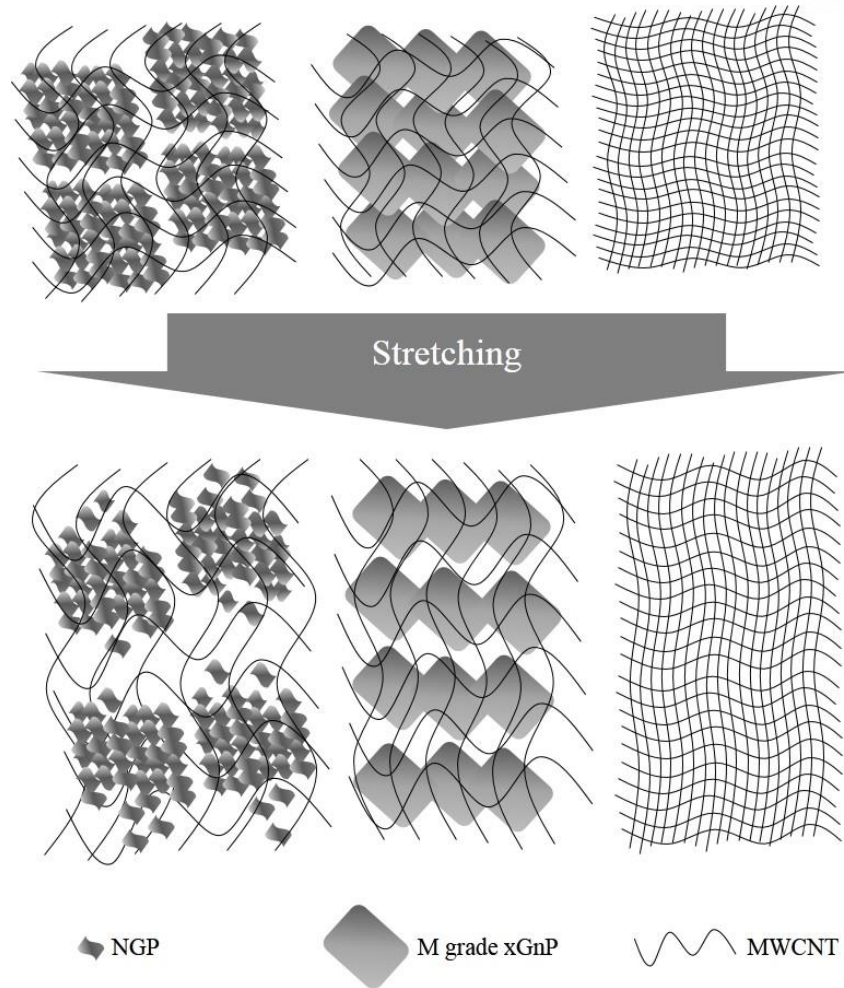
Figure 4-9 Schematic representation of microstructural changes in buckypaper and hybrid sheets subjected to mechanical strains.

Piezoresistive behavior of selected PC-impregnated composite sheets were characterized with the same test setup used for BPs and HSs without PC impregnation (Fig. 4-2). In order to investigate the effects of platelet-like nanomaterial geometry and content on strain sensitivity, composite samples containing CM-250, M-5, and NGP were selected. Fig. 4-10 shows the piezoresistive responses of PC-CM-250/M-5 composite sheets with varying CM-250:M-5 weight ratio, measured in three different directions – that is, (1) in the longitudinal direction parallel to the direction of maximum flexural strain (measured between Electrodes 4 and 5); (2) in the diagonal direction (measured between Electrodes 1 and 8); and (3) in the transverse direction perpendicular to the longitudinal direction (measured between Electrodes 2 and 7). (Refer to Fig. 4-6 for electrode number assignment.) The sensitivity of a piezoresistive sensor can be quantified using a gauge factor (GF), which is defined as the relative change in electrical resistance with respect to the strain incurred:

$$GF = \frac{\Delta R/R_0}{\varepsilon} \tag{3}$$

where R_0 is electrical resistance of composite in the pre-stressed state and ΔR is resistance change, R-R_0, generated by the applied mechanical strain, ε.

The electromechanical responses of PC-CM-250/M-5 composite sheets with varying M-5 content up to fracture are shown in Fig. 4-10. The results were fitted by linear regression, and their sensitivities, measured over the strain range of 0–3.5%, are summarized in Table 4-4 with R^2 for quantitative comparison. As M-5 content increases, GF in the longitudinal direction increases from 0.572 to 0.704 with the R^2 value of 0.99, while that in the diagonal direction increases moderately from 0.273 to 0.364 with a slightly lower R^2 value of 0.98–0.99. In the transverse direction, however, GF was measured to be close to zero regardless of M-5 content, which suggests that negligible strains are induced in the transverse direction. Thus, PC-impregnated carbon nanomaterial sheets is capable of measuring strain changes in multiple directions, that is, strains can be measured in arbitrary directions simply by placing the electrodes in the direction along which strains are desired to be measured, and that the sensitivity can be tuned by varying the MWCNT:M-5 ratio. In addition, drastic increases in resistance changes were observed in all three directions upon fracture, indicative of fracture-induced carbon nanomaterial network disruption. This suggests that piezoresistivity measurement allows not only strain monitoring but also detection of catastrophic structural failure. The piezoresistive responses of PC-CM-250/NGP composite sheets with varying NGP content measured up to fracture are shown in Fig. 4-11, and the sensitivities, measured over the strain range of 0–1.5%, are summarized in Table 4-5. Higher GFs were achieved in longitudinal and diagonal directions, as compared to PC-CM-250/M-5 composites, which may be attributed to the fact that the more loosely interconnected conductive network formed between MWCNTs and NGPs – due to the agglomeration of NGPs (Fig. 4-9) – led to higher strain sensitivity. Fig. 4-12 shows the piezoresistive responses of the various PC-impregnated carbon nanomaterial composite sheets subjected to cyclic flexural loading. For PC-CM-250 and PC-CM-250/M-5 composites, 2% flexural strain was applied, while 1% flexural strain was applied to PC-CM-250/NGP composites. The electrical resistance change show linear trends with cyclic flexural strains, and the linearity is maintained for multiple cycles with no apparent signs of drifting or capacitive charging–discharging. Among all types of composites, PC-CM-250/NGP composites showed the highest average GF. For example, at MWCNT:M-5 or MWCNT:NGP ratio of 50:50, the average GF of PC-CM-250/NGP was 0.92 in the longitudinal direction, while those for PC-CM-250 and PC-CM-250/M-5 composite sheets were 0.56 and 0.64, respectively. Again, from the cyclic electromechanical measurement, direction dependency was observed, and linearity was maintained for multiple cycles regardless of material type. The GFs obtained (<1) are relatively lower than previously reported values for BPs, which range between 1 and 5 [8, 146], and commercially available resistance-type strain gages, which range between 2 and 3.2. However, to the best of our knowledge, this is the first time the strain sensing abilities and sensitivity tenability of polymer-impregnated BPs and MWCNT/M-5 or NGP HSs

have been characterized systematically. Polymer-impregnated BP or HS composites allow substantially higher carbon nanomaterial loading (60–80 wt.%) with controlled nanostructure as compared to conventional nanocomposites, which is hindered by the difficulties associated with nanofiller dispersion and processability at high filler contents, and much improved handleability as compared to neat BPs and HSs. Polymer-impregnated BP and HS composites can serve as highly loaded, multi-functional materials with light weight, high strength and stiffness, and electrostatic discharging and electromagnetic shielding functionalities, in addition to strain sensing capability.
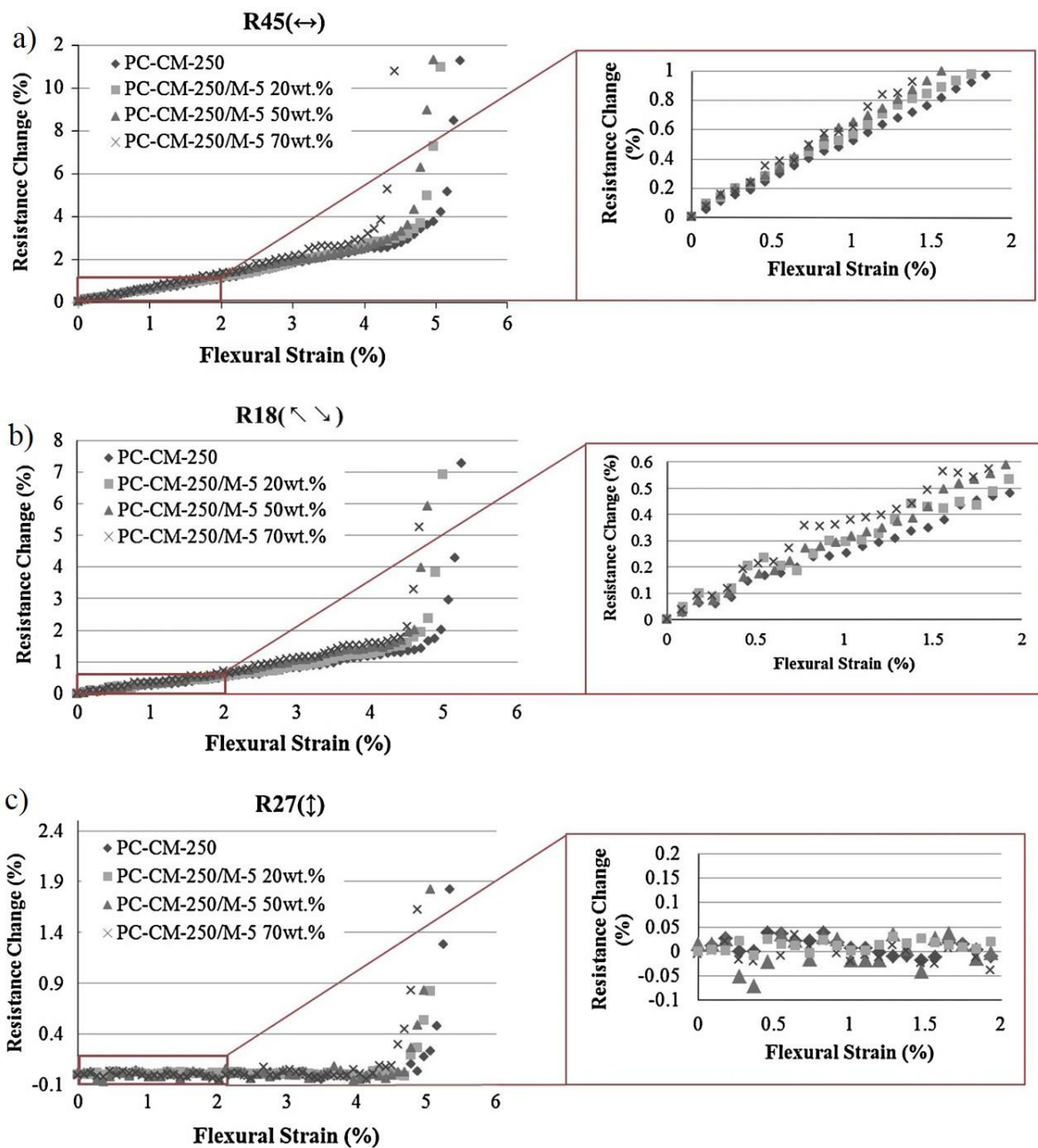
Figure 4-10 Electromechanical behavior of PC-CM-250/M-5 composite sheets with varying CM-250:M-5 ratio under flexural loading up to fracture, measured in: (a) longitudinal, (b) diagonal and (c) transverse directions.

Table 4-9 GF and R^2 with M-5 content and measured direction.

M-5 content (wt.%)	Measured direction	GF	R^2
0	Longitudinal (R45)	0.572	0.992
	Diagonal (R18)	0.273	0.989
	Transverse (R27)	-0.001	-0.009
20	Longitudinal (R45)	0.599	0.993
	Diagonal (R18)	0.294	0.977
	Transverse (R27)	-0.004	-0.314
50	Longitudinal (R45)	0.626	0.999
	Diagonal (R18)	0.341	0.985
	Transverse (R27)	0.003	0.031
70	Longitudinal (R45)	0.704	0.990
	Diagonal (R18)	0.364	0.982
	Transverse (R27)	0.0004	0.0003
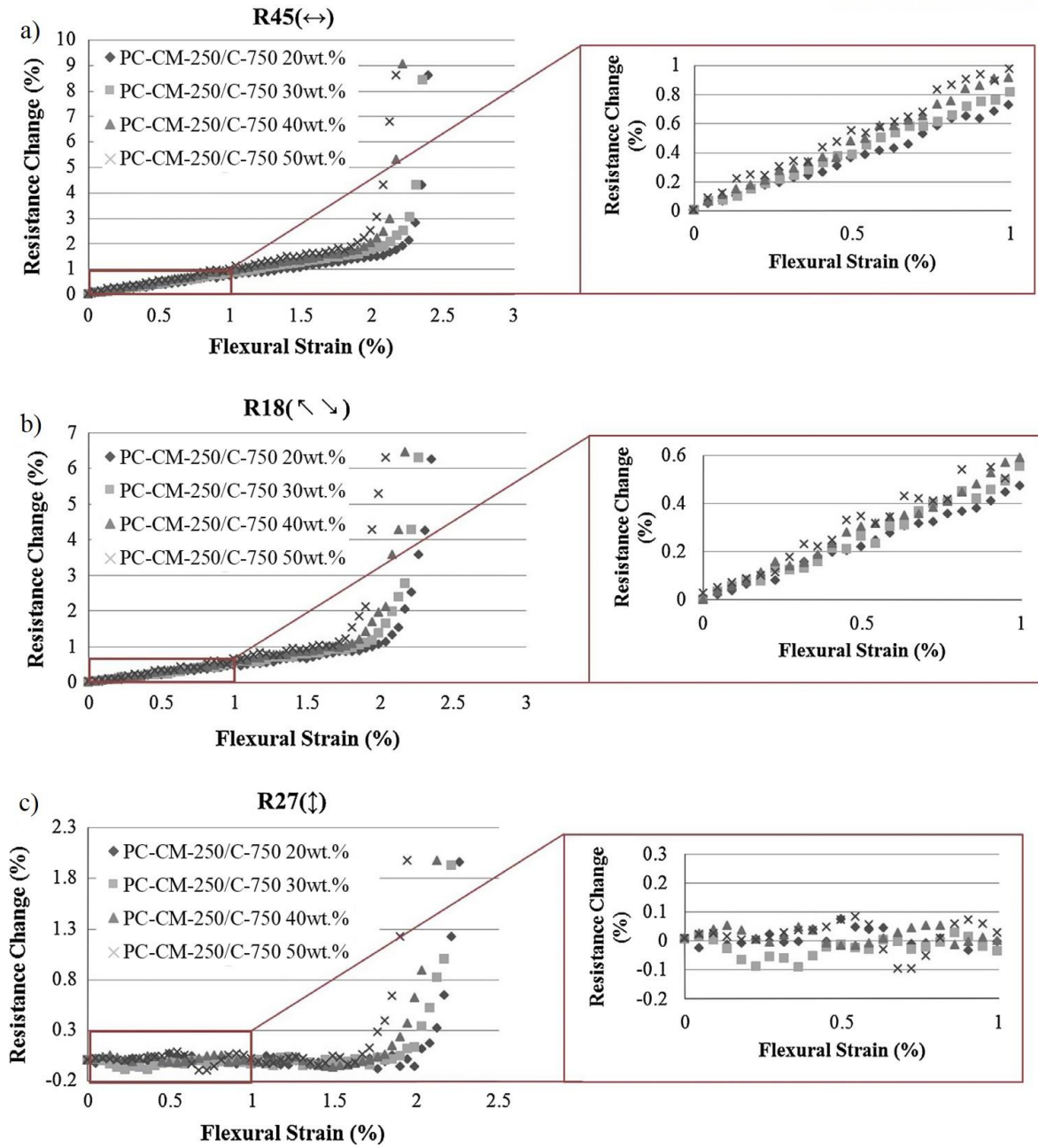
Figure 4-11 Electromechanical behavior of PC-CM-250/NGP composite sheets with varying CM-250:NGP ratio under flexural loading up to fracture, measured in: (a) longitudinal, (b) diagonal and (c) transverse directions.

Table 4-10 GF and R^2 with NGP content and measured direction.

NGP content (wt.%)	Measured direction	GF	R^2
0	Longitudinal (R45)	0.572	0.992
	Diagonal (R18)	0273	0.989
	Transverse (R27)	-0.001	-0.009
20	Longitudinal (R45)	0.714	0.995
	Diagonal (R18)	0.46	0.994
	Transverse (R27)	0.004	-0.046
30	Longitudinal (R45)	0.816	0.998
	Diagonal (R18)	0.525	0.986
	Transverse (R27)	-0.017	-0.253
40	Longitudinal (R45)	0.923	0.997
	Diagonal (R18)	0.583	0.99
	Transverse (R27)	0.014	-0.229
50	Longitudinal (R45)	0.997	0.989
	Diagonal (R18)	0.63	0.971
	Transverse (R27)	0.014	-0.05
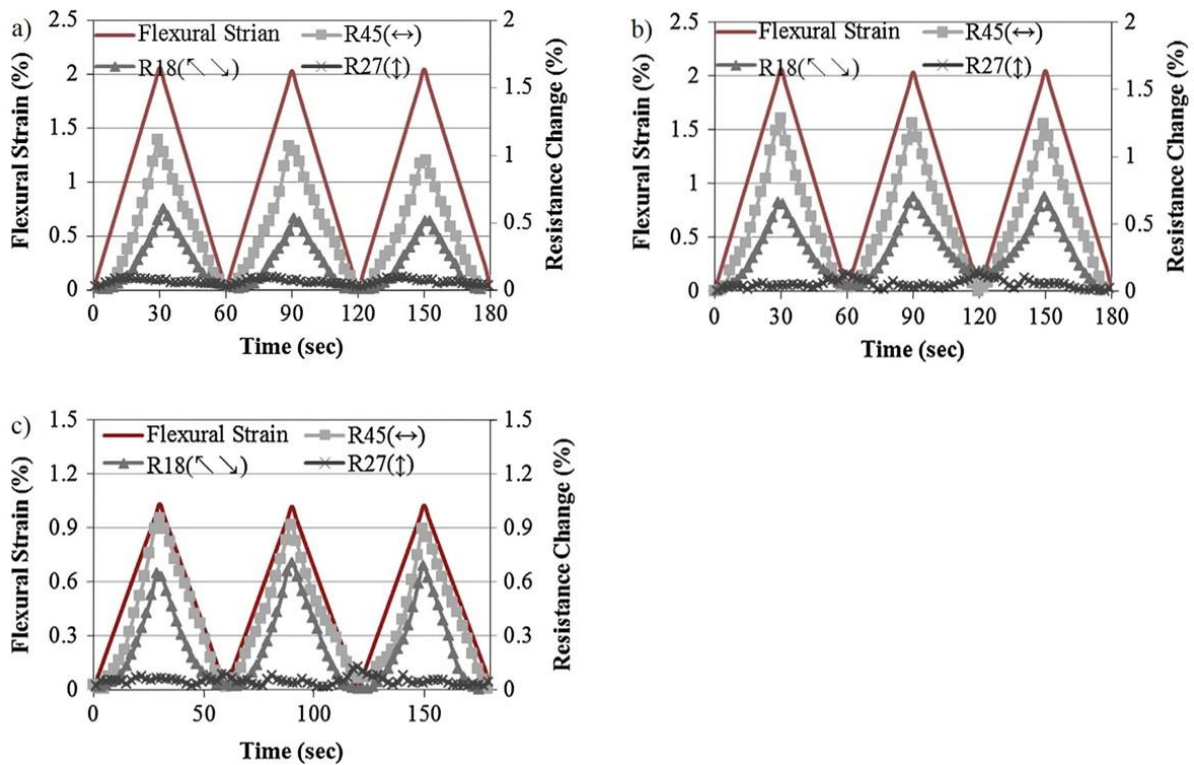
Figure 4-12 Multi-directional resistance changes in: (a) PC-CM-250, (b) PC-CM-250/M-5 and (c) PC-CM-250/NGP composites under cyclic flexural loading ((a and b): 2% strain and (c): 1% strain, respectively).

4. 4 Part Summary – Nanomaterial Shape *vs* Piezoresistive Behavior

The microstructural, mechanical, and electromechanical properties of PC-impregnated BP and HS composites have been reported in this chapter. The composite sheets were prepared by the vacuum filtration method, and carbon nanomaterial content decreased with decreasing MWCNT:xGnP ratio because the platelet-type fillers inhibit polymer flow, tending to entrap the polymer solution in the pores. The electromechanical behavior of composite sheets was characterized by in situ piezoresistivity measurement, and strain sensitivity was quantitatively analyzed using the gauge factor. The linearity of the change in resistance over a wide strain range shows the viability of these materials to be used as piezoresistive sensors. We demonstrated that the GF can be tailored by controlling the MWCNT:xGnP or MWCNT:NGP ratio, as it allows control of conductive network configuration, which directly influences strain sensitivity. It was also confirmed that the GF depends on the measured direction, which would allow multi-directional strain sensing using multiple electrodes placed on the periphery of the composite sheet sensor. The reversibility of the strain sensing composite sheets was also confirmed through cyclic flexural tests. PC-impregnated carbon nanomaterial sheets allow much improved mechanical properties and handling, as compared to unimpregnated sheets, which would facilitate practical applications. Currently, research is being performed to develop algorithms to extract 2D and 3D strain distributions from piezoresistivity data.

V. PART 2. REDUCED GRAPHENE OXIDE COATED POLYMER FILMS

5. 1 Part Introduction

Carbon nanotube(CNT)-based materials have been shown to have strong potential as smart materials due to their efficient electron transfer mechanism and high sensitivity [147]. Recently, based on a number of interesting properites of graphene, another type of carbon allotopes, such as high mobility of charge carriers, unique transport performance, high mechanical strength, and high electrical conductivity, much effort has been directed twoard expanding its application to smart materials, including chemical vapor sensors, bio sensors and strain sensors [148-154]. Moreover, graphene offers many advantages over CNTs, including ease of fabrication and ability to be patterned with optical transparency [67, 155, 156]. To date, strain-induced effects on graphene have been studied for band-gap creation, magnetic property tuning, and band structure modification, which were treated at the atomic level [119, 120, 157, 158]. On the contrary, strain-induced effects on electrical resistivity, so called piezoresistivity, was studied from the viewpoint of micro and nano structure of graphene and graphene-based strain sensors. For example, Fu *et al*. [122] first reported the piezoresistive response of a single layer of graphene CVD-grown on a PDMS substrate and Bae *et al*. [159] expanded measurable strain range by patterning graphene with specific graphene configuration and demonstrated its applicability to detect human finger motion. Nevertheless, there have been few systematic investigations on testing devices for stress-strain engineering with chemically converted graphene or reduced graphene oxide.

Graphene-based piezoresistive sensors detect the number and mobility of charge carriers within a material by changing the formation and the number of conductive networks formed by graphene under applied stress. The conductive network can be achieved by either patterned or randomly distributed graphene. Randomly distributed graphene strain sensors are more suitable for large-area sensing applications and provide relatively easy and cost-effective processing methods since they utilize readily accesible rGO [160]. It is also crucial to enable reliable strain sensing in large areas rather than on an atomic scale *via* uniform coating of dispersed rGO for enhancing the sensing capability of distributed sensors.

Here, we demonstrate a rGO coated polymer composite film as a transparent piezoresistive strain sensor. A simple 2D model of a rGO composite film is used to investigate the effects of interfacial bonding between graphene and support materials, areal coverage, and thickness of graphene on the piezoresistive behavior. The strain sensitivity showed a positive relaitonship with the adhesion strength between the conductive network and the support film and a negative relationship with both the density and thickness of conductive network. The optimized graphene-based strain sensor with great optical transparency and wide-area sensing ability shows a gauge factor of 8.67 with an excellent coefficient

of determination (R2) value of 0.99.

5. 2 Experimental

5. 2. 1 Preparation of Reduced Graphene Oxide Coated Epoxy (SU-8) Films

A 300-nm SiO_2 substrate was cleaned using acetone, isopropanol and DI water for 10 min in an ultra-sonication bath. After the substrate was treated with O_2 plasma for 10 min, it was immersed in a 1% APTMS/toluene solution for 5 min at 60℃. The APTMS-treated substrate was cleaned with toluene using ultra-sonication for 5 min, and the residual toluene was removed using nitrogen blowing. The GO solution, which was prepared by the method described in Electronic Supplementary Information, was spin-coated at 3,000 rpm for 30 sec on a SiO_2 substrate to fabricate the GO film. The thickness of the GO film was controlled by the number of spin-coating iterations and measured by ellipsometry (J. A.Woollam Co. Inc, EC-400 and M-2000V).

A 5-μm-thick SU-8 film was obtained by spin-coating a diluted SU-8 2010 solution (weight ratio between SU-8 and PGMEA was 5:1) at 3,000 rpm on a GO-coated SiO_2 substrate. After the SU-8 film was heated for 10 min at 95℃, it was exposed to a 365-nm UV source for 10 min. A post-exposure bake was conducted at 95℃ for 10 min. The SU-8 treated-GO substrate was peeled off from the SiO_2 substrate by immersing it in a 10% HF solution for 6 h and subsequently detaching.

To obtain a Tr-GO coated SU-8 film, the GO film was placed in a furnace at 1,000℃ for 30 minutes under H_2 and Ar conditions. A SU-8 film was fabricated on the heat-treated GO (Tr-GO) by spin-coating and curing, and the 300-nm SiO_2 layer was removed using 10% HF solution. In the case of Hr-GO-coated SU-8 films, the GO/SU-8 film and a glass vial containing 20 mL hydrazine solution were placed on a hot plate and then both were covered with glass bath for 24 hours at 100℃ allowing the hydrazine gas to evaporate (Hr-GO).

5. 2. 2 Characterization

Raman spectra were obtained with Alpha 300s from WITEC. The compositions of GO and rGO sheets were characterized by x-ray photoelectron spectroscopy (XPS) (Thermo Fisher, X-Alpha). The transmittance of the samples was measured by a UV-visible spectrometer (Varian, Cary 100). The SEM images were obtained by a scanning electron microscope (FEI, Nanonova 230). A scratch tester (CSM Instruments, RVT) was used to characterize the adhesion between rGO coatings and substrates. To analyze strain-induced G band peak shifts in Raman spectra and assess the interfacial adhesion between rGO and SU-8, the rGO coated SU-8 film was mechanically stretched while the G band peak shift was observed *in situ*.

An 8 by 30 mm rGO-coated SU-8 film was cut and bonded to a 10-mm-thick acrylic plate using epoxy glue. Electrodes were attached to the film using silver paste, which were connected to an

electrical signal acquisition system (Keithley 2002 digital multimeter). The sample was subjected to three-point bending using a universal materials testing system (Instron, Model 5982), and the piezoresistivity was measured simultaneously. The upper flexural strain limits to ensure linear, elastic deformations of composite films were determined through preliminary experiments, and 0.5% flexural strains were applied at a strain rate of 1% $\cdot$min^{-1}

5. 3 Results and Discussion

5. 3. 1 Reduced Graphene Oxide on SiO2 Wafer

In order to exploit the strain transfer capability in GO sensors, we have prepared rGOs with and without tight bonds between rGO and SU-8 support films. Fig. 5-1 illustrates the fabrication process of SU-8 films coated with thermally reduced graphene oxide (Tr-GO) and chemically reduced graphene oxide (Hr-GO). The details for GO synthesis, coating of GO layers on the surface of SiO$_2$-coated Si wafer, and substrate preparation have been presented in the previous section. The key fabrication step for the graphene-based strain sensor is the reduction process of the freestanding GO/SU-8 composite film either via a thermal or chemical process, since the reasonable electrical conductivity of GO should be secured for a piezoresistive strain sensor, for which measurable electrical conductivity is imperative. In order to obtain a Tr-GO/SU-8 film, the GO film coated on the SiO$_2$ wafer was heated/reduced in a furnace at an elevated temperature under H$_2$ and Ar conditions. A SU-8 film was spin-coated on the Tr-GO, and then the 300-nm-thick SiO$_2$ layer was removed using 10% HF solution, leaving a freestanding Tr-GO/SU-8 film. Since a large fraction of epoxy and -COOH functional groups are reduced and thus inactivated, only physical bonds between Tr-GO and SU-8 film are active, resulting in relatively weak adhesion at the interface.
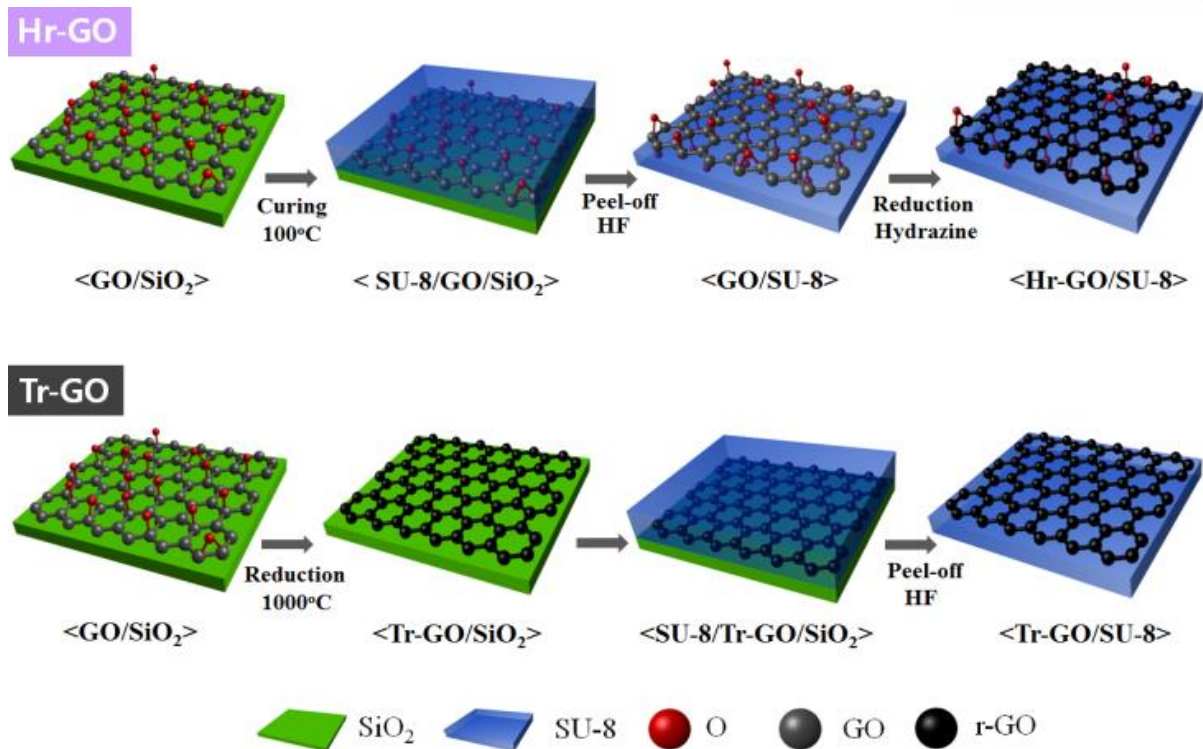
Figure 5-1 Fabrication procedures for Tr-GO- and Hr-GO-coated SU-8 films

The Hr-GO/SU-8 composite films utilized GO that has been chemically reduced by hydrazine after the event of covalent bonding between SU-8 and GO as illustrated in Fig. 5-2. To fabricate the Hr-GO/SU-8 films, a SU-8 solution was spin-coated over GO and thermally cured at 100°C for 10 min, leading to covalent bonds between GO and the SU-8 film. Previous studies reported that epoxy functional groups in SU-8 remain reactive and thus induce crosslinking reactions during heating due to the presence of the acidic curing agent in the films [160]. It is therefore expected that the epoxies in GO participate in crosslinking reactions with the epoxy groups in the SU-8, forming tightly attached chemical bonds at the interface between the GO and SU-8 layers. Finally, The Hr-GO/SU-8 composite films are prepared by the hydrazine reduction process under a sealed container.
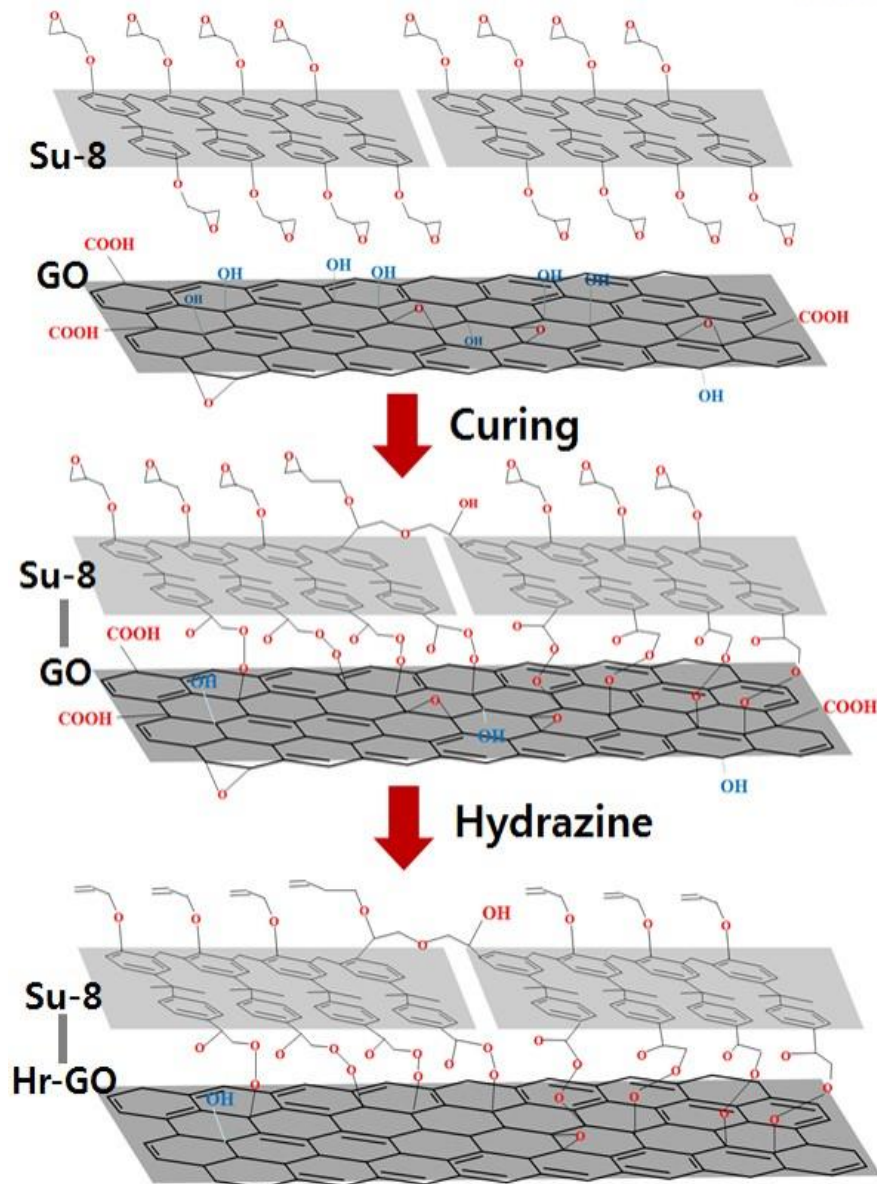
Figure 5-2 Schematic diagram showing the preparation of Hr-GO coated SU-8 film and the mechanism of creating covalent bonds between Hr-GO and SU-8.

The SU-8 films coated with varying rGO densities and thicknesses were fabricated to investigate their effects on the piezoresistive response of rGO coated SU-8 films (Fig. 5-3 and Table 5-1). The 6-7 nm thick rGO films with different coating densities were fabricated by controlling the number of spin-coating of the GO solution (GO 2 mL + water 8 mL). One time coating and three time coating films were designated as "starve coated" and "fully coated" samples, respectively. In addition to the density control of the rGO films, the coating thickness was varied to 13-14 and 21-23 nm ranges by spin coating high-concentration GO solution (GO 2 mL + water 2 mL) 2 and 4 times, respectively.
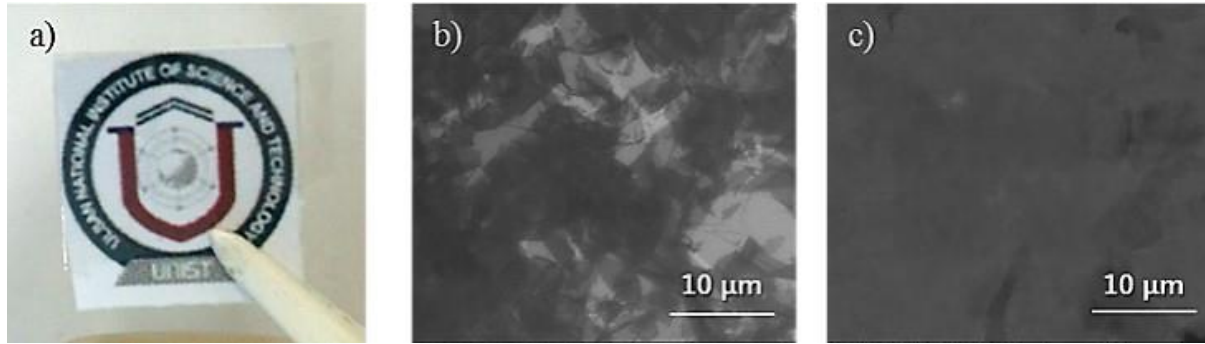
Figure 5-3 (a) Digital photograph of transparent rGO-coated SU-8 film prepared by hydrazine reduction and SEM images of (b) Hr-GO starve coated and (c) Hr-GO fully coated films.

Table 5-2 Comparison of rGO-coated films with various reduction methods, coating densities, and thicknesses.

Coating thickness [nm] [a]	Hydrazine reduction		Thermal reduction	
6 – 7	Hr-GO starve coated	Hr-GO fully coated	Tr-GO starve coated	Tr-GO fully coated
13 – 14	Hr-GO 13 (or 14)		Tr-GO 13 (or 14)	
21 – 23	Hr-GO 21 (or 23)		Tr-GO 21 (or 23)	

Fig. 5-4 (a) shows the optical transparency of SU-8 substrates coated with 13-nm-thick GO, Hr-GO and Tr-GO on a quartz plate measured by a UV–visible absorption spectrometer. Unlike the GO-coated SU-8 film, which exhibited nearly 97% transmittance, rGO films showed 83% transmittance over the 450-800 nm wavelength range regardless of the reduction method. These transmittance values are in good agreement with values reported on rGO coated devices with similar coating thicknesses.35 However, Hr-GO and Tr-GO coated films show different surfaces resistivity values of 2.84 and 0.83 MΩ/sq, respectively. These results indicate the higher degree of crystallinity and more effectively reduced graphene structure in Tr-GO, which agrees well with the Raman spectra and the C/O ratios calculated from XPS (Fig.5-5). As shown in Fig. 5-4 (b), the transmittance of Hr-GO and surface resistivity decrease from 90 to 65% at 550 nm and from 6.29 to 0.52 MΩ/sq, respectively, as the thickness of the film is increased from 6-7 to 21-23 nm due to the tightly bound interconnected conductive networks formed by thicker coatings.
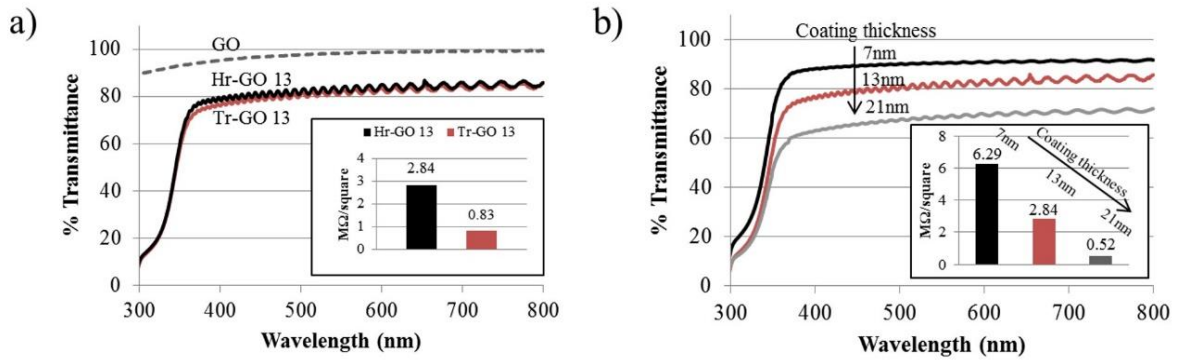
Figure 5-4 Transmittance of (a) GO on Si wafer (dotted line), Hr-GO 13 (black line) and Tr-GO 13 (red line) starve coated film and (b) Tr-GO coated films with different coating thickness (6, 13, 21 nm). The inset images show the surface resistivities of GO and rGO films.
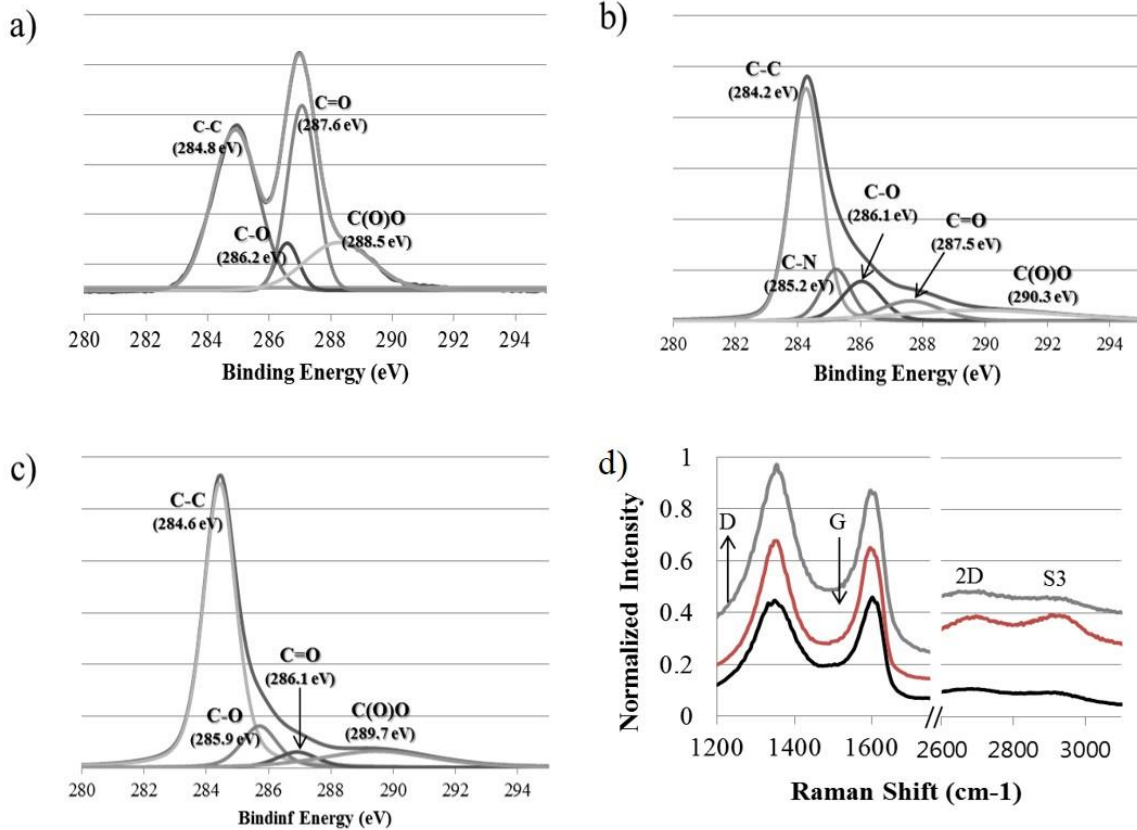
Figure 5-5 Deconvoluted XPS spectra of the C1s region of (a) GO, (b) Hr-GO and (c) Tr-GO. (d) Raman spectra of GO (black line) and rGO (Hr-GO; red line, Tr-GO; grey line) with different reduction methods.

5. 3. 2 Interfacial Bonding Between Reduced Graphene Oxide and *SU-8* Polymer

An acoustics-based scratch test was employed to quantitatively compare the interfacial bond strength in Hr-GO/SU-8 and Tr-GO/SU-8 films. In this test, the coated surfaces were scratched over a length of 7 mm at a rate of 5 mm/min while increasing the normal load linearly from 0 to 50 N, and the acoustic emission signal was measured simultaneously. As can be seen in Fig. 5-6 (a), Hr-GO/SU-8 shows a

50

higher critical load of 39.8 N as compared to that (31.2 N) for Tr-GO/SU-8; this load corresponds to the force required to delaminate the rGO layer from the substrate, resulting in the max-out of the acoustic emission signal. Fig. 5-6 (b) indicates that all of the critical loads measured from the Hr-GO/SU8 films with different rGO thicknesses were higher (in the neighborhood of 40 N) than those obtained from the Tr-GO/SU8 film, suggesting that Hr-GO exhibits stronger adhesion to the SU-8 film than the Tr-GO. The greater adhesion strength between the Hr-GO and SU-8 film can be attributed to the presence of strong chemical bonds in the Hr-GO/SU8 films.
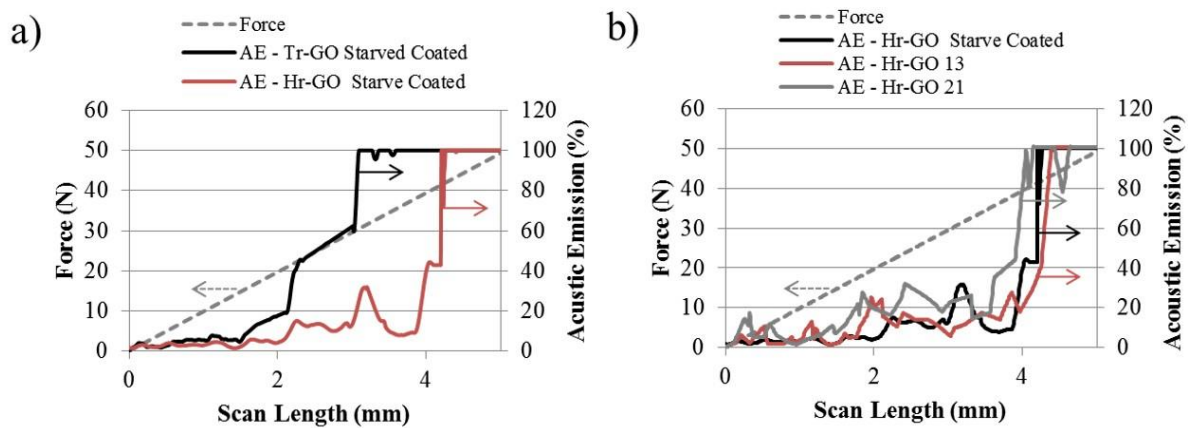
Figure 5-6 Scratch test results from (a) Hr-GO starve coated (red) and Tr-GO starve coated (black) SU-8 composite films. Further tests were carried out with (b) Hr-GO-coated SU-8 films with different coating thicknesses.

Raman spectroscopy is a useful tool to probe the crystallographic orientation of graphene with respect to the strain. In general, the G peak splits into two bands, G^+ and G^- peaks, when the film is under applied strain, and the degree of red shift and splitting of both the G peak and the 2D peak increase with an increase in the applied strain. In the present case, the 2D band of the Raman spectra of graphene, which is clear evidence of strains induced in the graphene, overlapped with the peaks from the SU-8 substrate [119, 161]. Hence, we analyzed the peak shift of the G band to quantify the effect of strain in the graphene. Raman spectra were obtained from five different positions within the composite film under investigation, and the spectra were curve-fitted to obtain the G band frequency. Fig. 5-7 (a) and (b) show the in situ G peak position changes in Hr-GO and Tr-GO starve coated films, respectively, while strain is applied. The G frequency of the Hr-GO starve coated film shifted from 1584.22 to 1573.52 cm^{-1} upon application of the 2.32% uniaxial strain, while that of the Tr-GO starve coated film shifted from 1585.15 to 1578 cm^{-1} upon application of 2.11% strain. A linear dependence of the G band frequency on strain is observed, with a slope of -4.61 ± 0.18 cm^{-1}/% for the Hr-GO starve coated film and -3.28 ± 0.26 cm^{-1}/% for the Tr-GO starve coated film, respectively, as shown in Fig. 5-7 (c). These values are comparable to the strain-induced Raman spectroscopy results of CVD-grown graphene on a PET substrate as reported by Ni *et al*. [119] (-12.1 ~ -14 cm^{-1}/% depending on the number of graphene layers).

The relatively smaller shift of the G band for the Hr-GO and Tr-GO films, compared to the uniformly covered CVD-grown graphene over a large contact area, is likely due to the morphological nature of rGO coated on the surface of an SU-8 film, characterized by wrinkles and relatively low electrical conductivity. However, the greater G frequency shift for the Hr-GO coated film as compared to that for the Tr-GO starve coated film still provides strong evidence of improved adhesion between the chemically reduced GO and SU-8 film.
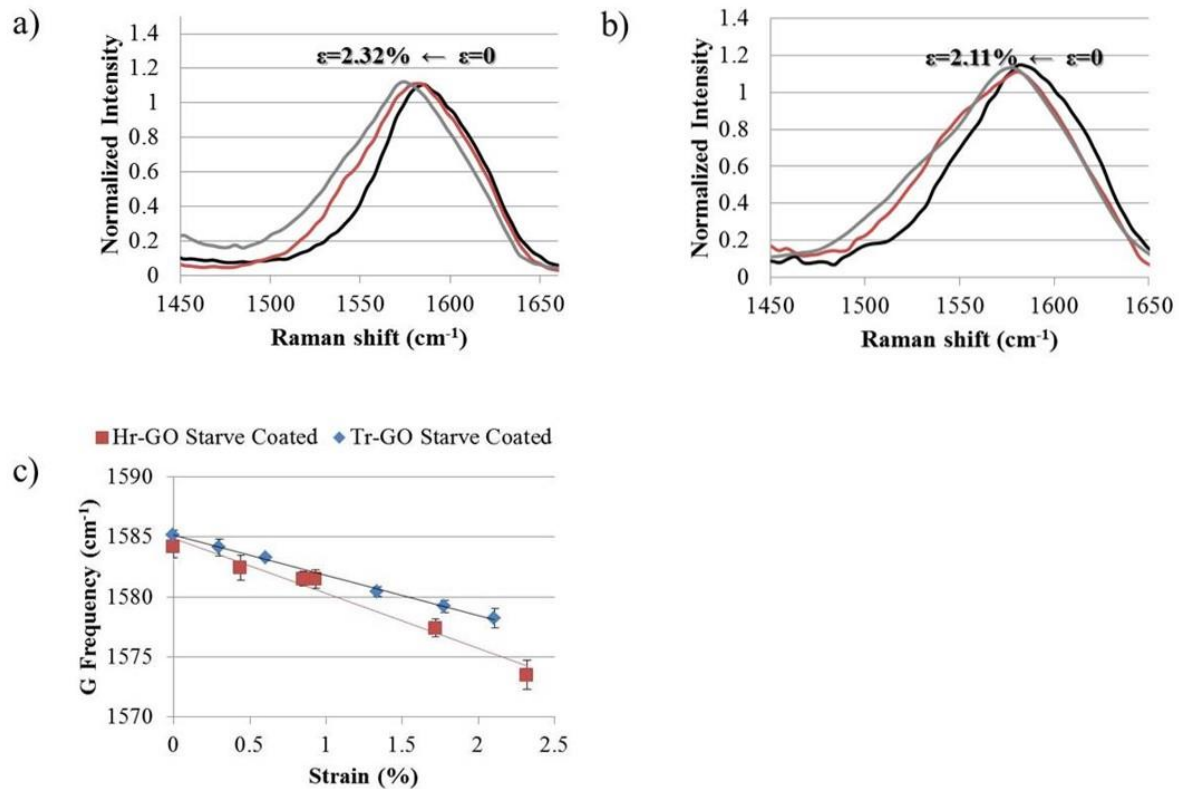
Figure 5-7 The G band frequency of (a) Hr-GO/SU-8 film, (b) Tr-GO/SU-8 film (both starve coated) subjected to uniaxial strain, (c) G frequency plotted with applied strain showing linear trends.

5. 3. 3 Piezoresistive Response of Reduced Graphene Oxide coated Films

As shown in Fig. 5-8 (a) and (b), piezoresistive responses of Hr-GO and Tr-GO coated SU-8 films attached on an acrylic plate were measured using a universal materials testing system under flexure mode and a low-resistance digital multimeter, the combination of which enables in situ measurement of electrical resistance change while flexural strain is induced. As the acrylic plate undergoes three-point bending, the rGO coated film undergoes the identical flexural strain as the bottom surface of the plate, as shown in Fig. 5-8 (c) and (d). Strain was applied to Hr-GO and Tr-GO coated films with a strain rate of 2%/min up to failure. For both types of films, failure occurred at near 3.5% strain.
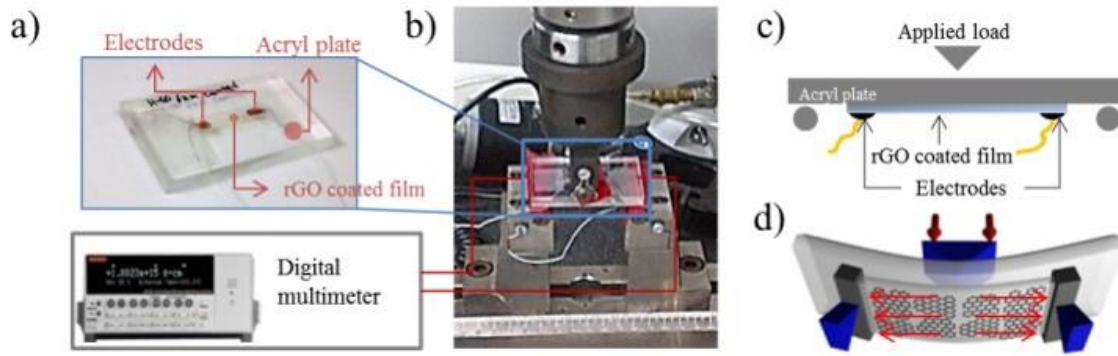
Figure 5-8 (a) rGO coated SU-8 film attached on the acrylic surface. Electrodes were connected to monitor resistivity change. (b) Piezoresistivity measurement setup with flexure test fixture. (c) Loading configuration during piezoresistivity measurement. (d) Bottom view showing quasi-uniaxial strain field in the longitudinal direction.

The piezoresistive responses of rGO coatings with different reduction methods and coating densities are shown in Fig. 5-9, where the linearity is indicated by the coefficient of determination (R^2). From Fig. 5-9 (a), (b) and (c), it is clear that the relationship between resistance change and mechanical strain exhibits a linear trend, implying that the piezoresistivity mainly occurs by the change in conductive networks formed by rGO [149]. However, the discrepancies in gauge factors were observed with varying reduction methods and coating densities. As the areal density of 6-nm-thick Hr-GO coating increases – from starve coated to fully coated – the gauge factor decreased from 8.66 to 7.47 with a R^2 value of 0.99. A similar trend was observed for Tr-GO coatings, where gauge factor decreased from 7.57 to 6.51 with a R^2 value of 0.97. The lower gauge factor and R^2 values obtained for Tr-GO coatings relative to that for Hr-GO coatings are attributed to less efficient strain transfer from SU-8 to Tr-GO due to the weak interfacial bonding between them. It should be noted that the R^2 value of Hr-GO decreased as the coating thickness increased to 14 and 23 nm, that is, the piezoresistive behavior deviated from a linear trend, which is attributed to the lower sensitivity at larger thicknesses. Furthermore, in the case of densely connected conductive networks generated from a fully coated film, it is more difficult to disrupt the conductive network by deflection as compared to the loosely connected conductive networks generated from starve coated films.

The piezoresistive responses of rGO-coated films subjected to 0.5% cyclic flexural strain are shown on the right-hand side in Fig. 5-9. The changes in electrical resistance of both Tr-GO and Hr-GO starve coated films also show linear relationships with cyclic flexural strains, and the linearity is maintained for multiple cycles with no apparent signs of drifting or capacitive charging-discharging. A small difference in sensitivity caused by the strength of interfacial adhesion between the Hr-GO and Tr-GO starve coated films is observed. However, lower sensitivity and linearity with permanent resistance changes, evidenced by the presence of positive residual resistance upon load removal, were observed for samples with larger rGO coating thicknesses. This is due to the ineffective strain transfer from the SU-8 film to the rGO coating and the permanent change in the conformation of distributed rGO caused

by delamination of rGO layers from the SU-8 film. Therefore, the reduction method affects the sensitivity even at small strain amplitudes, while rGO coating thickness affects both the linearity and repeatability.

As shown in piezoresitive response of rGO coated films, rGO can be fabricated in a large scale, which allows for a large and continuous strain sensor for real-time structural health monitoring. Unlike other studies on graphene based piezoresistive sensors, rGO based neurons offer an easier route to be integrated into existing structural neural systems because of their scalable fabrication procedures and continuous strain sensing mechanisms.
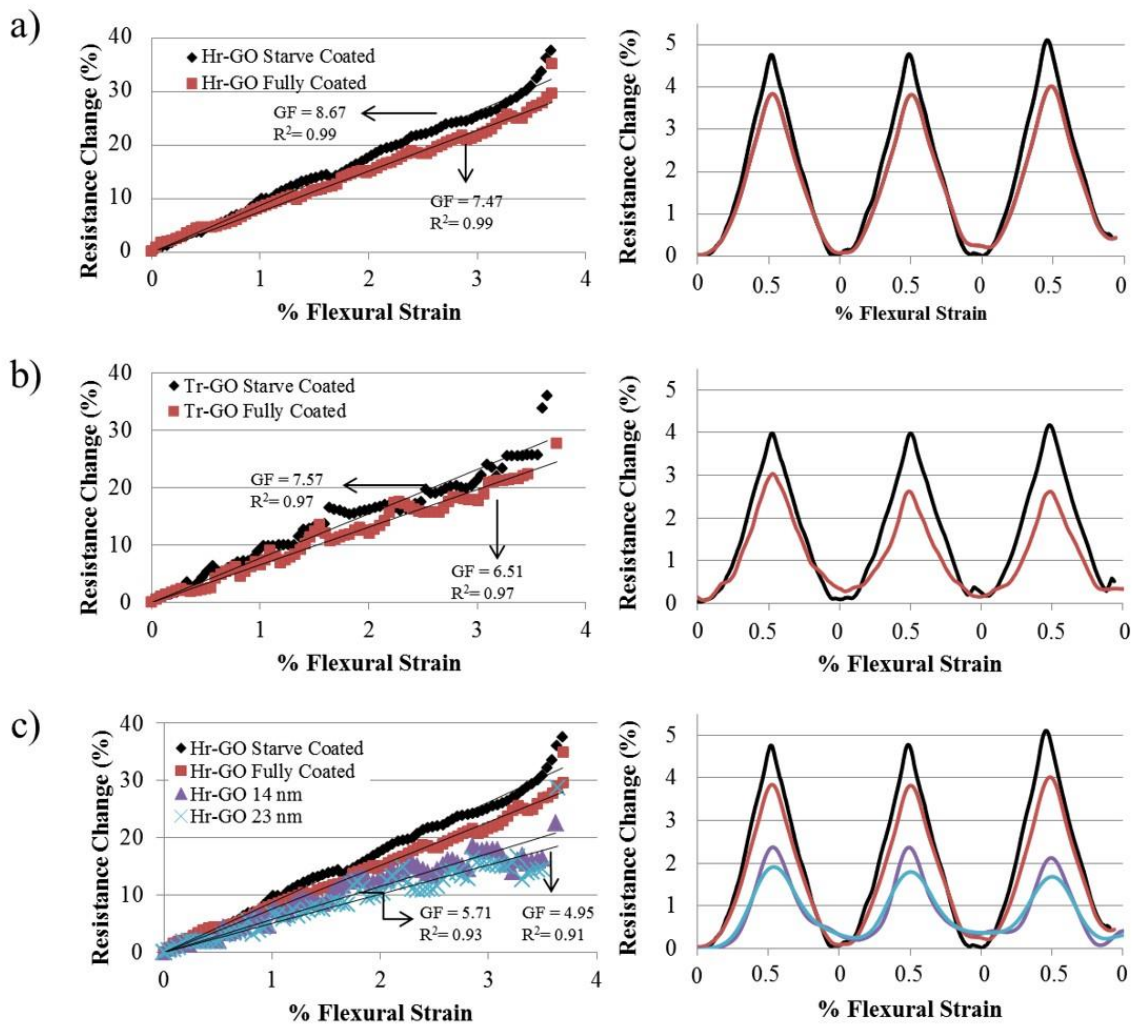
Figure 5-9 Piezoresistive responses of (a) Hr-GO coated films and (b) Tr-GO coated films with different areal coverage (black: starve coated, red: fully coated). Further studies were carried out on (c) Hr-GO/SU-8 films with different Hr-GO thicknesses. The corresponding piezoresistive responses under 0.5% of cyclic flexural strain are shown on the right.

5. 4 Part Summary-Covalently Bonded Interface vs Piezoresistive Behavior

We have fabricated rGO coated SU-8 films employing different reduction methods, coating densities, and thicknesses that can be utilized as transparent, wide-area, piezoresistive graphene sensors. The covalent bonding in Hr-GO coated films resulted from curing between epoxy functional groups, whereas physical bonding was created by the van der Waals attraction between thermally treated rGO and SU-8 films. The relative adhesion strengths were indirectly measured by a scratch test and by observing the G band frequency shift in Raman spectroscopy in situ while strain was applied. Hr-GO and Tr-GO starve coated films show linear dependence of resistance change on applied strain. Stronger adhesion obtained by covalent bonds between Hr-GO and SU-8 substrate allows more effective strain transfer at the interface as the conductive network responds more readily to the strain. However, strain transfer efficiency and therefore electro-mechanical sensitivity are retarded as the rGO coating thickness increases, as the more densely interconnected conductive network and the relatively weaker interactions between rGO layers due to their wrinkled morphologies lead to lower gauge factor and linearity, respectively. Hr-GO starve coated film with a coating thickness of 6 nm showed the highest gauge factor and R^2 values of 8.67 and 0.99, respectively. The systematic approach presented to optimize the fabrication process for rGO coated polymer composite films offers extensive information to design transparent, high-performance, sensitivity-tunable, piezoresitive sensors, which can make inroads into such applications as wide-area strain sensors, self-sensing flexible electronics, and intelligent structural health monitoring.

VI. PART 3. POLYDOPAMINE FUNCTIONALIZED GO – PVA COMPOSITES

6. 1 Part Introduction

Oxygen-containing functional groups are reported to be well suited for composites with a polar polymer matrix, such as PMMA, PAN and polyacrylic acid (PAA), and 'intimate' graphene-polymer interactions and a percolated interphase essential for mechanical enhancement have been reported [162]. Therefore, PVA filled with GO could be a good combination for achieving strong interfacial bonding, as PVA chains should strongly bind on the surface of GO by hydrogen bonding. Based on this rationale, PVA/GO composites have been explored both experimentally and theoretically, and the relationship between hydrogen bonding density and the mechanical properties of the composites has been studied. Zhang *et al*. [163] and Wang *et al*. [164] reported increased tensile modulus, strength, and strain-to-failure at GO loadings lower than 1-1.8 wt.%. Wang et al. reported that the yield strengths of GO/PVA composites increased linearly up to 11.01 MPa (a 136% increase compared to neat PVA) as GO content was increased from 0 to 5 wt.%; a maximum strain-to-failure of 210% (a 27% increase) was reported at 1.5 wt.% loading. Chemically-functionalized graphene sheets covalently bonded to PVA were studied, and yield strength and strain-to-failure of 72 MPa and 191%, respectively, were reported at 0.5wt.% loading. Zhang *et al*. [163], reported tensile strength and strain-to-failure of 3.48 MPa (a 132% increase) and 165% (a 62% increase) at 1 wt.% loading. GO/PVA or chemically functionalized graphene/PVA composites are reported to show this unusual increase in toughness because of their 'molecular level' dispersion and high density of hydrogen bonding. An ideal configuration would be when the edges of the sheets are joined together side by side. However, when a critical content is reached, i.e., 1-1.8 wt.%, the GO sheets begin to stack together driven by the strong Van der Waals force, decreasing the efficiency of the mechanical reinforcement.

Dopamine, a hormone and neurotransmitter, is similar to adhesive proteins [165-167]. At a weak alkaline pH condition, dopamine self-polymerizes to produce an adherent polydopamine coating on a wide range of substrates with the oxidation of catechol groups to the quinone form. It binds strongly to most organic and inorganic surfaces, such as metals, metal oxides, and polymer surfaces. Also, the oxidized quinone form of catechol can undergo reactions with various functional groups, such as thiol, amine, and quinone itself, by Michael addition or the Schiff base reaction to form covalently-grafted functional layers. Moreover, dopamine could be used to reduce GO during its polymerization on the GO surface [168].

In this part, we report a simple and practical approach to synthesize graphene-reinforced PVA composite films by combining GO with polydopamine, (dGO), in an aqueous solution with the simultaneous reduction of GO to reduced graphene oxide sheets. The dGO/PVA composites obtained

exhibited significant improvements in mechanical properties as a result of increased interfacial interactions produced by the combined mechanisms of hydrogen bonding and polymer entanglement between PVA and polydopamine, which binds on the graphene oxide surface. Polydopamine is believed to play a role as an adhesive. With the addition of dGO, we achieved simultaneous improvements in tensile modulus, strength, and strain-to-failure. We also demonstrated that dGO/PVA composite films can be used as structurally robust humidity sensors that use electrical conductivity to measure humidity.

6. 2 Experimental

6. 2. 1 Fabrication of Polydopamine Functionalized Graphene Oxide

75 mg dopamine hydrochloride was added into a 150 mL tris-HCl buffer solution (10 mM), and pH of the solution was tuned to 8.5 using 0.1 M NaOH solution. Then, this solution was mixed with 150 mL of the GO suspension (1.0 mg/mL) at ambient conditions and the mixture stirred for 2 h at room temperature. Finally, the color of the solution turned to dark brown due to the pH-induced oxidative polymerization of dopamine hydrochloride and the reduction of GO.

Dopamine, a hormone and neurotransmitter, is similar to adhesive proteins. At a weak alkaline pH condition, dopamine self-polymerizes to produce an adherent polydopamine coating on a wide range of substrates with the oxidation of catechol groups to the quinone form [165-167]. It binds strongly to most organic and inorganic surfaces, such as metals, metal oxides, and polymer surfaces. Also, the oxidized quinone form of catechol can undergo reactions with various functional groups, such as thiol, amine, and quinone itself, by Michael addition or the Schiff base reaction to form covalently-grafted functional layers. Moreover, dopamine could be used to reduce GO during its polymerization on the GO surface [169].

Synthesis of graphene-reinforced PVA composite films by combining GO with polydopamine, in an aqueous solution with the simultaneous reduction of GO to reduced graphene oxide (rGO) sheets. The dGO/PVA composites obtained exhibited significant improvements in mechanical properties as a result of increased interfacial interactions produced by the combined mechanisms of hydrogen bonding between amine and hydroxyl groups of polydopamine and abundant hydroxyl groups of PVA and polymer entanglement between PVA and polydopamine (Fig. 6-1) [170]. Polydopamine is also believed to play a role of binding with GO sheets *via* hydrogen bonding between amine and hydroxyl groups of polydopamine and hydroxyl groups of GO as well as π-π of GO interaction between catechol and small graphitic domains of GO [171]. With the addition of dGO, we achieved simultaneous improvements in tensile modulus, strength, and strain-to-failure. We also demonstrated that dGO/PVA composite films can be used as structurally robust humidity sensors that use electrical conductivity to measure humidity.
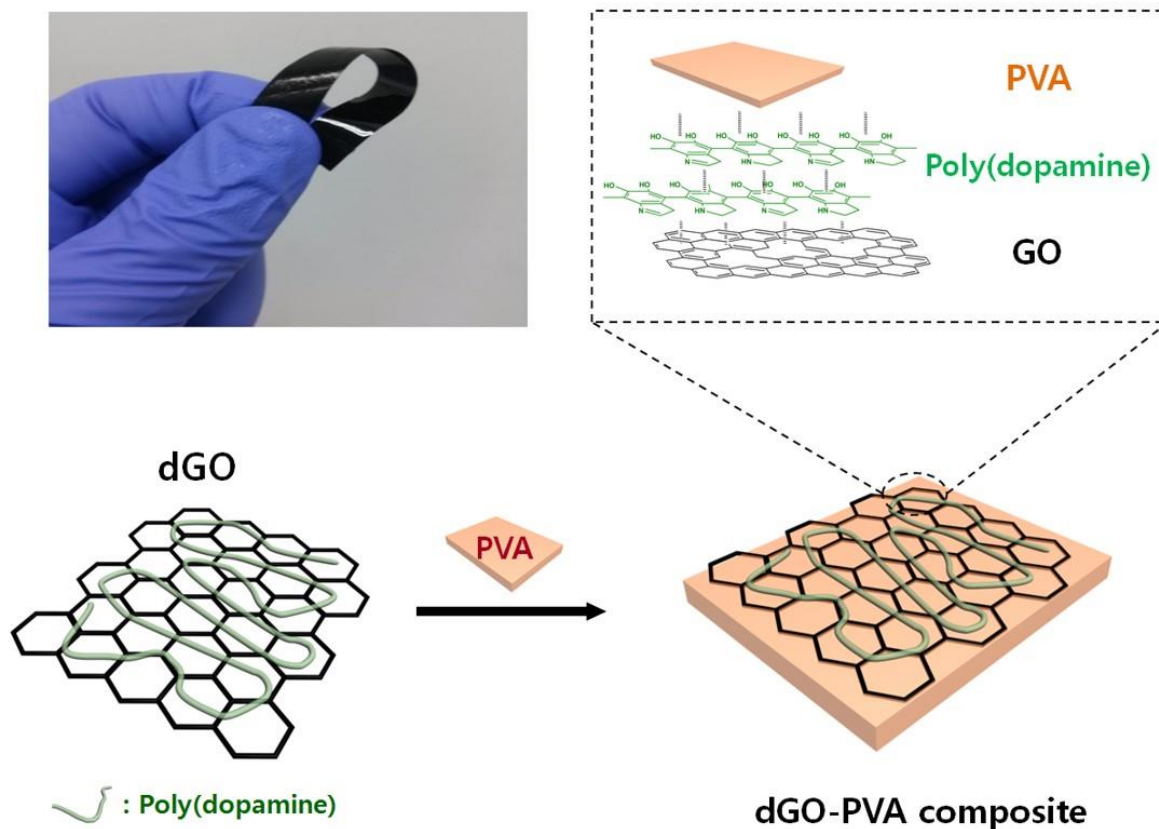
Figure 6-1 A photograph and proposed structure of a dGO/PVA composite film.

6. 2. 2 Fabrication of Polydopamine Functionalized GO/PVA Composite Films

The fabrication procedure for the dGO/PVA composite (GO loading = 0.5 wt.%) was as follows: dGO was dispersed in distilled water (15 mL) in an ultrasonic bath for 60 min at room temperature. PVA (~2 g) was dissolved in distilled water (200 mL) at 90℃. After the PVA-H2O solution had cooled to around 60℃, the dGO aqueous dispersion was gradually poured into the PVA solution and sonicated for an additional 15 min at room temperature. Finally, this homogeneous dGO/PVA solution was poured into a Teflon Petri dish and kept at 60℃ for film formation until its weight equilibrated. The film was peeled from the substrate and was hot pressed at 200℃ in order to eliminate any remaining voids. A series of dGO/PVA composite films with various polydopamine:GO ratios (1:0, 0.5:1, 1:1) was similarly prepared. In all these samples, the GO content was kept constant at 0.5 wt.%. For comparison, GO/PVA composite films were prepared according to the same procedure with a loading of 0.5 wt.%. As a reference sample, a pure PVA film was prepared by the hot casting technique.

6. 2. 3 Characterization

Tensile properties, including modulus, strength, and strain-to-failure, of the films fabricated were measured using a dynamical mechanical analyzer (DMA Q800, TA Instruments), operated under a quasi-static, strain-controlled mode at a constant strain rate of 20%/min. Specimens measuring 45 mm by 12 mm with a thickness of 80 μm were laser-cut (VersaLaser VLS2.30, Universal Laser Systems)

and installed in a film tensile fixture. Tensile tests were performed until the specimens ruptured. Load and elongation were measured simultaneously.

To assess the potential applicability of dGO/PVA composite films as humidity sensors, water uptake, quantified by swelling ratio, and humidity sensitivity were measured. Vacuum-dried film samples were immersed in distilled water until saturated and their weight became constant. The samples were then removed from the water, and their surfaces were blotted with a filter paper before being weighed. The swelling ratios of the films were calculated using the following formula:

$$\text{Swelling ratio} = \frac{W - W_0}{W_0} \times 100 (\%) \qquad (4)$$

where W_0 and W are the weights of the sample before and after immersing in water, respectively.

A strip of a dGO/PVA composite film was installed in an in-house-fabricated fixture devised to measure humidity sensitivity, as shown in Fig 9. The fixture was placed in a relative humidity(RH)-controlled chamber and soaked at a pre-defined RH until equilibrium was reached. RH was varied step-wise in a cyclic mode, while the change in film resistance was measured in situ, using a high-resistance digital multimeter (6517B, Keithley Instruments) at an applied voltage of 3V.

6. 3 Results and Discussion

6. 3. 1 Polydopamine Functionalized Graphene Oxide

dGO was prepared by mixing an aqueous suspension of GO and a solution of dopamine hydrochloride in a buffer solution (10 mM Tris-HCl, pH 8.5). In a basic aqueous solution, polydopamine is spontaneously formed by oxidative polymerization. The solutions were prepared with different GO/polydopamine ratios such as 0.25:1, 0.5:1, and 1:1 (w/w). It was confirmed from SEM images that the dGO sheets were well-dispersed in deionized water. The increase in thickness of the GO sheets by coating them with polydopamine was determined by atomic force microscopy (AFM). Fig. 6-2 shows the morphology and thickness of GO and dGO sheets. The thickness of as-prepared GO sheets was around 0.89 nm, which is thicker than pristine graphene due to the functional groups on the graphene surfaces produced by the oxidation (Figs 6-2 (a) and (b)) [90, 172]. On the other hand, the average thickness of dGO was around 2.24 nm (Figs 2(c) and (d)), indicating that the increase in thickness of 1.35 nm is due to the presence of polydopamine on the GO sheets. Note that polydopamine has a very similar structure to eumelanin which is characterized by an interconnected layered structure along the z-axis with a graphite-like stacking spacing of 3.4-3.8Å [173-176].
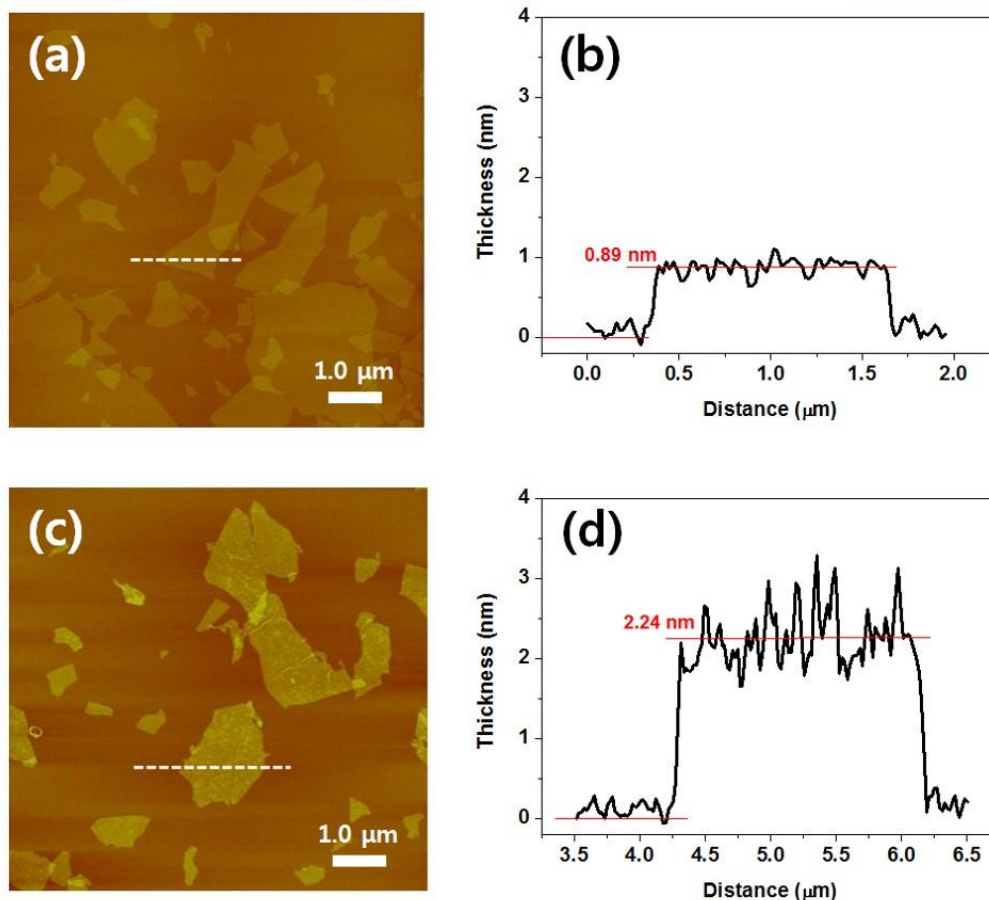
Figure 6-2 (a) and (b) AFM image and height profile of GO. (c) and (d) AFM image and height profile of dGO. GO and dGO (dopamine:GO = 0.5:1) samples were spin-coated on a Si wafer for AFM measurements.

The polydopamine coating on the GO sheets was also proved by XPS. XPS survey spectra of GO and dGO samples in Fig. 6-3 (a) showed that N 1s peak at 398 eV was observed in only the dGO sample. The N 1s peak originates from amine groups of the polydopamine layer on GO sheets. From the XPS spectrum of the dGO sample, the nitrogen/carbon atomic ratio (N/C) was calculated to be 0.095. It has been reported that the theoretical value of N/C in dopamine is 0.125 and the N/C value in polydopamine layers on different substrates is between 0.1 and 0.1329. So, if we consider the GO layer as a substrate, the N/C value of 0.095 in our sample is quite reasonable. Fig. 6-3 (b) shows that in the C 1s binding region a peak due to oxygen-containing groups between 286 to 290 eV in the GO sample has been mostly removed in the dGO sample, indicating partial reduction of GO by the adsorption and polymerization of dopamine. Indeed, it has been known that GO can be reduced by released electrons during oxidative polymerization of catecholeamines such as dopamine and norepinephrine [169].
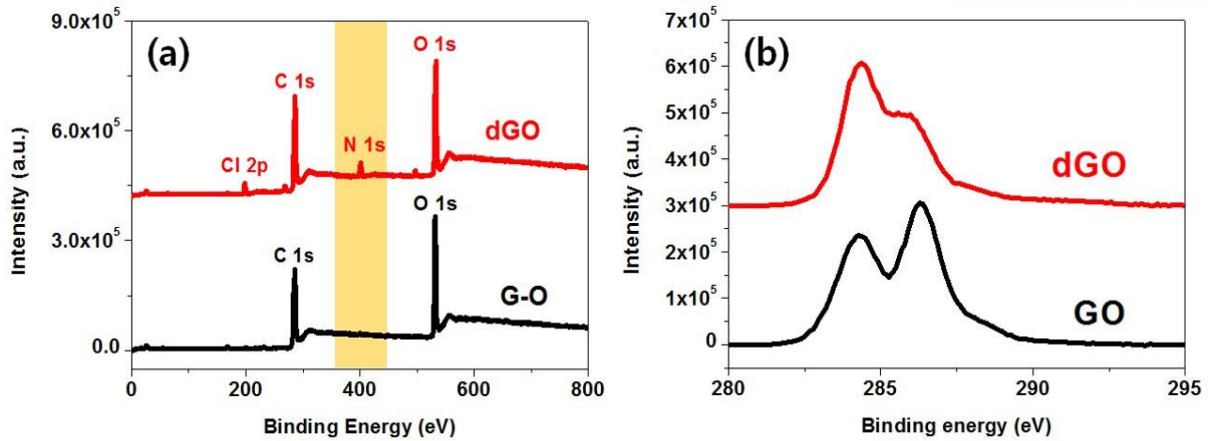
Figure 6-3 (a) XPS survey spectra and (b) C1s binding energy region of GO and dGO spin-coated on a Si wafer. An additional Cl 2p peak in (a) originates from dopamine hydrochloride (HCl) which was used as the precursor of polydopamine.

We measured attenuated total reflectance Fourier transform infrared (ATR-FTIR) spectra of GO and dGO as shown in Fig.6-4. The typical FTIR spectrum of GO shows O−H stretching vibrations in the region of 3,000 to 3,400 cm^{-1}, C=O stretching vibrations from carbonyl and carboxylic groups at 1,720 cm^{-1}, skeletal vibrations from unoxidized graphitic domains at 1,620 cm^{-1}, C−OH stretching vibrations at 1,160 cm^{-1},and C−O stretching vibrations at 1,040 cm^{-1} [90, 177]. On the other hand, the FT-IR spectrum of the dGO sample showed a newly developed peak at 1,500 cm-1, corresponding to the N−H bending mode of aromatic secondary amine in dGO [178]. This result confirms that the polydopamine on the GO sheets possesses aromatic, nitrogenous species, such as the indole- or indoline- type structures widely proposed in polydopamine and eumelanins [173]. Note that the region between 3,000 and 3,400 cm^{-1} could not be used to identify the N−H stretching mode of secondary amine due to the broad band in the region possibly caused by strong hydrogen bonds between polydopamine and oxygen-containing groups in GO sheets.
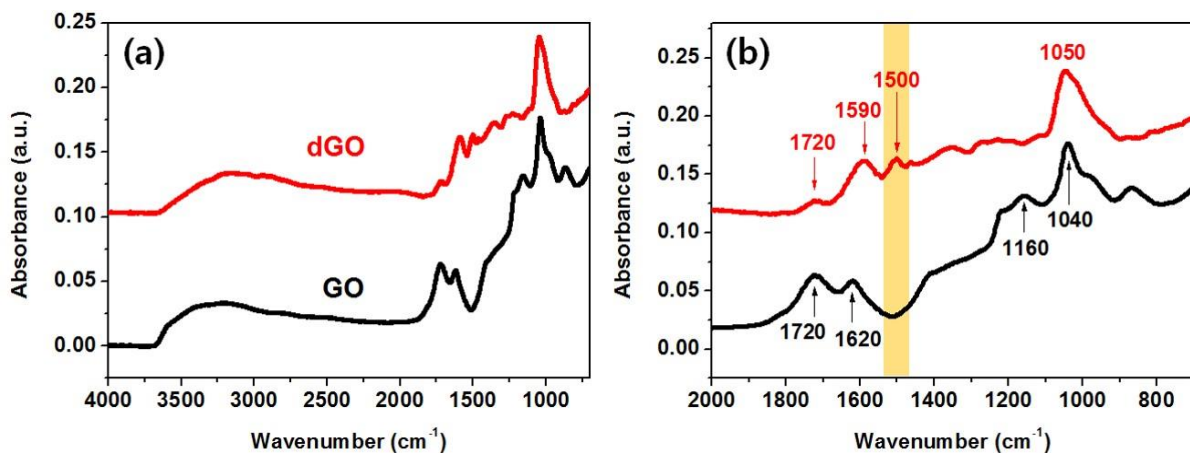
Figure 6-4 (a) ATR-FTIR spectra of GO and dGO samples in the region between 4000 and 700 cm^{-1} and (b) magnified wave number range of 2,000 to 700 cm^{-1} of GO and dGO. To obtain a thick film of GO and dGO for ATR-FTIR measurement, each solution was repeatedly coated onto a Si wafer by drop casting.

6. 3. 2 Tensile Properties

The mechanical properties of a composite reflect the state of its homogeneity and the interfacial interactions between its constituents. Typical stress-strain behaviors of dGO/PVA composites with different polydopamine:GO ratios and dGO contents are shown in Fig. 6-5 (a) and (b) and summarized in Tables 6-1 and 6-2. Previous research confirmed that GO has a significant effect on the mechanical properties of PVA composites[179]. In particular, Wang *et al*. [164] showed that PVA is toughened by GO and rGO at very low loadings (~0.5 wt.%). Fig. 6-5 (a) shows both reinforcement and toughening. From Table 6-1, the average tensile modulus increases from 2.1 GPa for neat PVA to 3.31GPa for a 0.5 wt.% GO/PVA composite. In addition, the tensile strength also increases from 41.48 to 53.37 MPa, and the maximum strain-to-failure increases from 97.15 to 161.28%.

It is obvious that dGO is a more effective reinforcement for PVA compared to as-synthesized GO. Table 6-1 shows that the addition of 0.5 wt.% dGO to polydopamine:GO with a weight ratio of 0.5:1 results in the highest tensile strength of 82.9 MPa and a strain-to-failure of 184%. At a polydopamine:GO ratio of 1:1, the mechanical properties of the material were slightly decreased compared to that for the 0.5:1 ratio; however, they were still higher than the those of the as-prepared GO/PVA composite at the same loading.

The dGO/PVA composites obtained exhibited significant improvements in mechanical properties because of increased interfacial interactions produced by the combined mechanisms of hydrogen bonding between amine and hydroxyl groups of polydopamine and abundant hydroxyl groups of PVA and polymer entanglement between PVA and polydopamine (Fig 6-1). Polydopamine is also believed to play a role of binding with GO sheets *via* hydrogen bonding between amine and hydroxyl groups of polydopamine and hydroxyl groups of GO as well as π-π of GO interaction between catechol and small graphitic domains of GO [171].

Fig 6-5 (b) and Table 6-2 show that when dGO content in polydopamine:GO= 0.5:1 increases above 0.5 wt.% , the ultimate tensile strength and maximum strain-to-failure decrease while the tensile modulus increases. As described by Wang *et al*. [180], as the graphene sheets added and join together side by side thereby reached ideal condition of graphene dispersion in the polymer matrix. After this critical content, graphene sheets are stack together since the distance between two sheets being so small then van der Waals force become essential. This may be attributed to the fact that at dGO contents above 0.5 wt.%, dGO re-stacking begins to dominate over the reinforcing effect, which adversely affects these parameters. On the other hand, the tensile modulus increases because it is more dependent on the wt.% of dGO and is much less sensitive to interfacial bonding.
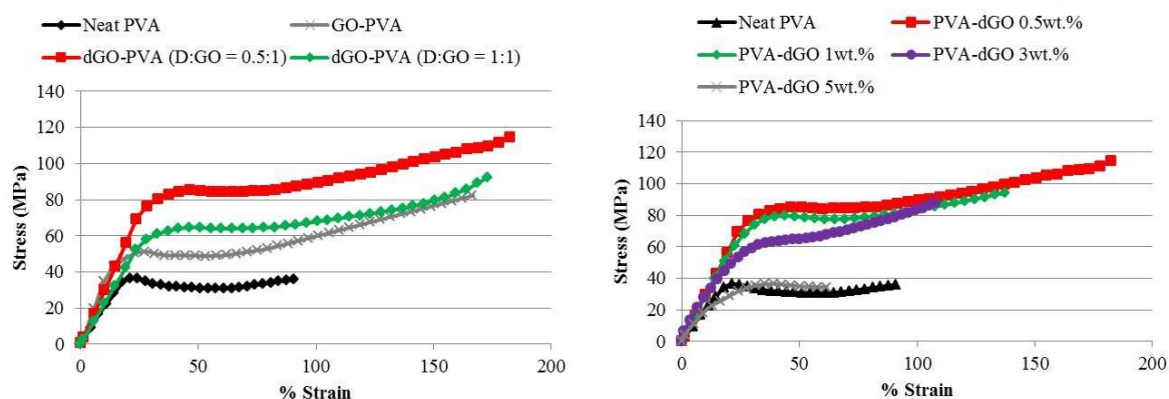
Figure 6-5 Stress-strain curves of: (a) neat PVA, GO/PVA, dGO/PVA composite films at 0.5 wt.% GO or dGO loading and (b) dGO/PVA composite films with various dGO loadings (polydopamine:GO = 0.5:1).

Table 6-3 Tensile properties of GO/PVA and dGO/PVA composites. (at 0.5 wt.% GO loading)

Film type	Neat PVA	GO/PVA	dGO/PVA (D:GO = 0.5:1)	dGO/PVA (D:GO = 1:1)
E(GPa)	2.10	3.31	2.92	2.48
UTS (MPa)	41.48	53.37	82.92	62.47
Strain-to-failure (%)	97.15	161.28	183.68	172.75

Table 6-4 Tensile properties of dGO/PVA composites. (polydopamine:GO = 0.5:1)

dGO content (wt.%)	0	0.5	1	3	5
E(GPa)	2.10	2.92	3.12	3.34	1.95
UTS (MPa)	41.48	82.92	80.92	80.92	39.12
Strain-to-failure (%)	97.15	183.68	132.51	119.95	52.82

6. 3. 3 Swelling Ratio and Water Resistance

To measure the effect of dGO on the swelling behavior of PVA films, water uptake of the composite films was measured as a function of time. As shown in Fig 6-6 (a), the general observation is that all the samples show a relatively drastic increase in water adsorption up to ~5 hr, where it begins to level off. It is evident that the extent of water uptake decreases with increasing dGO content, indicative of dGO serving as a moisture barrier. GO is hydrophilic and contains numerous hydroxyl groups, which accelerate water adsorption when exposed to moisture. However, GO provides nano-dispersed sites whose interactions with the surrounding PVA molecules restrain the swelling of GO/PVA composites, leading to a lower swelling ratio. Zhang *et al*. [163] reported a critical maximum swelling ratio of ~170% at 0.6 wt.% GO. However, our dGO/PVA composites show a lower maximum swelling ratio (around

120% at 3 or 5 wt.% dGO) compared to a neat PVA film. Hence, it is believed that strong adhesion of polydopamine to PVA chains can prevent swelling of the composites. Thus, a larger interfacial area was physically crosslinked by dGO in PVA films as shown in Fig 6-1. Also, water-dipping tests for the composite films in Figs 6-6 (b) and (c) show interesting results in that composites with 3 and 5 wt.% of dGO exhibited no weight loss after 12 hours, whereas the neat PVA film dissolved in water and essentially disappeared.
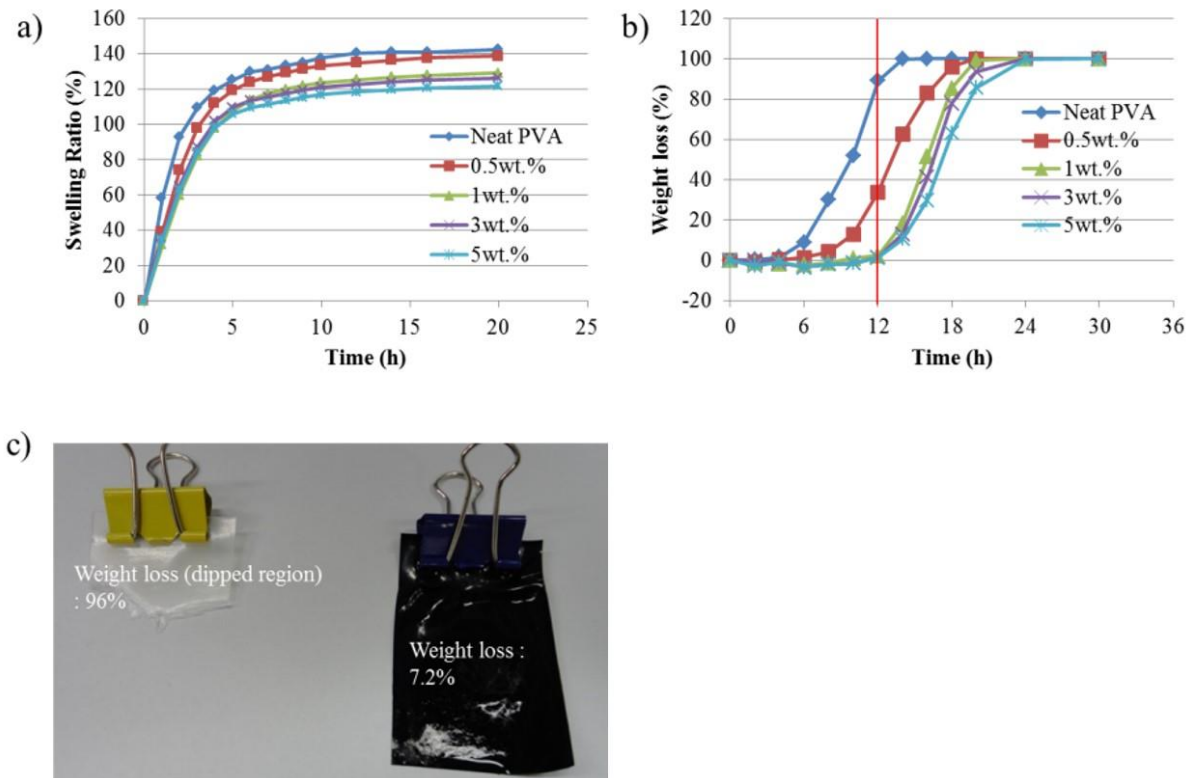
Figure 6-6 (a) Swelling ratio, (b) weight losses measured from water-dipping tests performed on dried dGO/PVA (polydopamine:GO=0.5:1) composite films with various GO contents. (c) Optical photograph shows difference in weight loss between neat PVA and dGO/PVA films after 12 hours of dipping in water at room temperature.

6. 3. 4 Conductometric Humidity Sensing

PVA films with a dGO filler can serve as an effective humidity sensor due to their ability to absorb moisture to a moderate level while maintaining their structural integrity, with dGO serving as a moisture barrier as shown in Fig 6-6. The swelling of the polymer matrix due to moisture absorption leads to an increase in electrical resistance as the electrical conductive network formed by dGO nanosheets becomes disrupted.

Electrical resistance versus RH is plotted for 3 and 5 wt.% dGO/PVA films in Figs 6-7 (a) and (b). On the basis of the compositions of the composites, the mechanism behind the change in resistance when subjected to humidity can be explained as follows. In dGO/PVA composites, PVA acts as an

insulating matrix. Meanwhile, polymerization of polydopamine facilitates partial chemical reduction of GO, which imparts electrical conductivity in dGO/PVA composite films. When the surface of a dGO/PVA film is exposed to water molecules, adsorption occurs and capillary condensation of water produces a proton (H^+) as shown in Eq. (5).

$$H_2O = H^+ + OH^- \quad\quad\quad\quad (5)$$

This proton can be a carrier for the improvement of electrical conduction in dGO/PVA films, and more protons are produced when the sensing material is exposed to more humidity in the testing system [181]. In Fig 6-7 (a), the resistance of dGO/PVA films is plotted with stepwise dehumidification from a RH of 94.5 to 41.2%. From a comparison of 3 and 5 wt.% dGO/PVA composite films, it is clear that the 3 wt.% film shows a more drastic increase in resistance below 50% RH. This is attributed to the fact that at 3 wt.% the loosely interconnected dGO conductive network is more susceptible to proton removal by dehumidification, compared to the 5 wt.% material. In both stepwise dehumidification and continuous humidification cases, nonlinear resistance changes with respect to RH were observed, and the samples were more moisture-sensitive at lower RH values. This may be due to the fact that proton saturation for conduction is more readily reached in low-humidity regions and is in good agreement with other reported results from PVA-based humidity sensors [182, 183].
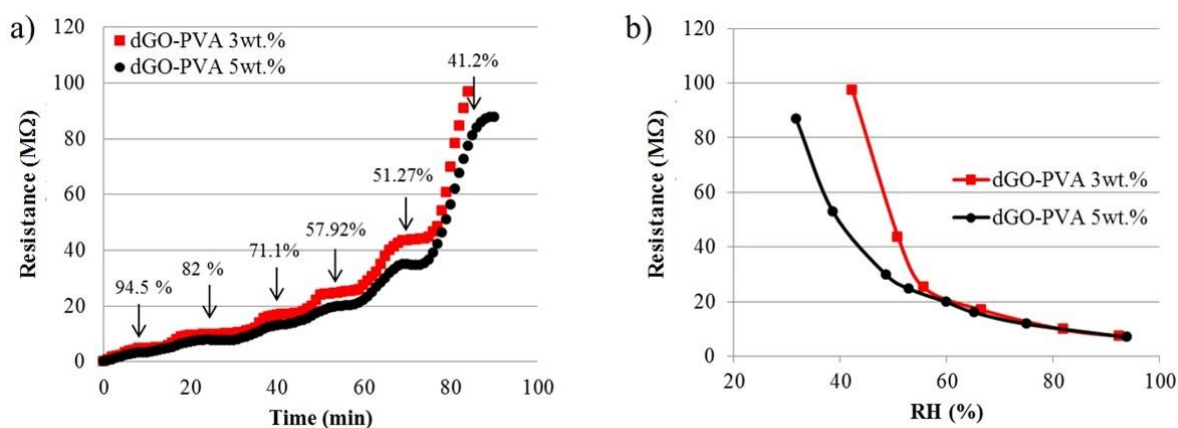
Figure 6-7 Variation of resistance with respect to (a) stepwise dehumidification and (b) linear humidification for different dGO loadings.

To characterize the repeatability and response of dGO/PVA films, dynamic adsorption-desorption cycles between 40 and 60% RH were used. Fig 6-8 shows the time response and recovery curve of a 5 wt.% dGO/PVA film subjected to humidification-dehumidification cycles with a period of 10 min. The sample showed excellent sensing repeatability, and the difference in maximum resistance was less than 1% over 4 cycles. It is expected that the humidity sensing repeatability under cyclic input will be valid outside the range of 40-60% RH, although the sensitivity will be lower above 60% RH.

Barkauskas *et al.* [184] showed the extremely narrow humidity sensing range of PVA (between 98 and 99% RH, or 1.17% ΔRH) could be widened to 43.4% ΔRH by using different substrates, aging and the addition of carbon black. To overcome this issue of a limited sensing range, Li *et al.*[183] used polyaniline as a main sensor material, which was combined with PVA for water absorption. Yang *et al.*[185] added electrolytes, such as sodium chloride (NaCl) to a PVA matrix to increase both the sensitivity and sensitivity range of the PVA films. Both approaches suffer from limitations in long term stability and mechanical properties because of electrolyte loss and oxidation. However, we broadened the sensitivity range of PVA-based humidity sensors to 58.3% ΔRH without sacrificing structural integrity and long-term performance.
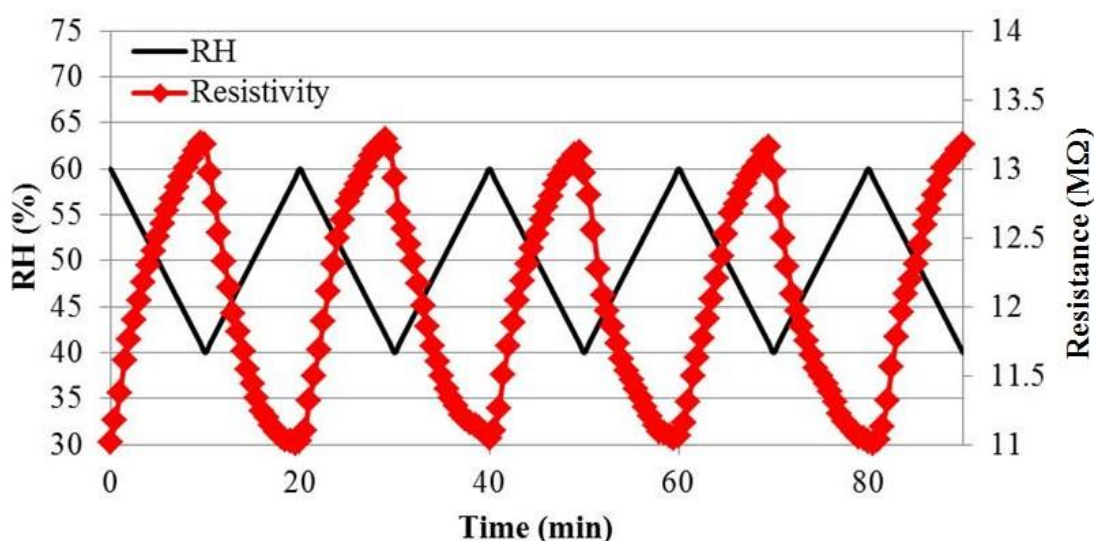
Figure 6-8 Resistance reversibility in the response of a 5 wt.% dGO/PVA film at 30 ℃.

6. 4 Part Summary – Non-covalently Bonded Interface *vs* Piezoresistive Behavior

This chapter presented a simple approach to produce GO modified with polydopamine in aqueous solution followed by spontaneous reduction of GO during the polymerization of dopamine to yield dGO. A combination of hydrogen bonding, strong adhesion of polydopamine at the interface of PVA and GO, and reinforcing effects of GO resulted in simultaneous increases in tensile modulus, ultimate tensile strength, and strain-to-failure of 39, 100, and 89%, respectively, at a 0.5 wt.% dGO loading. It was also demonstrated that dGO can serve as an effective moisture barrier in inherently water-soluble PVA and enables dGO/PVA composite films to be used as robust, cost-effective, easy-to-use humidity sensors over the relative humidity range of 40-100%. It was shown that the dGO concentration in PVA, which governs proton generation, can serve as an effective parameter to control the moisture sensitivity and that the composite films are robust under cyclic humidification-dehumidification conditions.

VII.   PART 4. FUNCTIONALIZED GRAPHENE OXIDE HYDROGEL

7. 1 Part Introduction

The 3D architectures made of 2D graphene sheets played a crucial role in its several applications and performance. In recent years, much effort has been devoted to develop methods for fabrication and potential applications of 3D structured graphene hygrogel [186]. Although several methods for the formation of 3D graphene sheet network into hydrogel have been reported, relatively few researches have paid attention to their structural properties or methodical approach for control of the microstructure, particularly the precise control of pore size and distribution. Several attempts to synthesis graphene hydrogel studied and determined that the distinction on the 3D architectures clearly resulted in its primary characteristics such as electrical conductivity, mechanical integrity or chemical or catalytic activity [187-189]. From the discovery of 3D network of rGO *via* hydrothermal process reported by Shi *et al*. [186], the 3D graphene hydrogel framework of flexible graphene sheets was fabricated upon basic mechanism known as physical cross-linking. Other strategy used so far was using polymers and organics as cross-linking agents [186, 190].

In this chapter, our research conducted on conducting cylindrical structure of spongy like reduced graphene oxide hydrogels (rGOHs) using ethylene diamine– and ascorbic acid–functionalized GO *via* hydrothermal method. Such materials have typically been studied for applications in electronic and catalysis devices [190]. However, it is still a challenge to fabricate graphene hydrogel with controlled pore size thereby controlled mechanical and electrical response. These compressible light weight graphene hydrogel with various porosity, surface area and electrical conductivity controlled by several experimental parameters including chemical modification, GO concentration and degree of reduction. The result shows electrical conduction network formed by bridged graphene platelets were densified by applied compressive strain and their response to strain were varied with porosity of graphene hydrogel. This piezoresistive behavior allows the graphene hydrogel to act as strain sensors capable of measuring compressive strains up to 16%, with controlled sensitivity and mechanical robustness.

Before the entering into details, I'd like to make an additional remark that this research was conducted in collaboration with the University of Ulsan especially the technology involved with fabrication of functionalized GOHs and its basic characterization.

7. 2 Experimental

7. 2. 1 Fabrication of Functionalized Graphene Oxide and Hydrogel

One milliliter of an aqueous solution of EDA was slowly added into 10 mL GO suspensions with

GO concentrations of 5, 10, and 15 mg mL^{-1} and ultrasonicated for 2 h at 10 ℃. The hydrogel formation by the crosslinking reaction between GO and EDA was performed for 8 h at 80℃ [190].

The obtained GOH, solution was placed into 2 L deionized water for 1 h in order to wash the unreacted EDA under stirring, which was repeated 5 times. All samples were freeze-dried at -37 ℃ for 2 days in order to remove water without destroying their structures. The fabricated samples were named after the GO concentration. EDA-rGOH-5, EDA-rGOH-10, and EDA-rGOH-15 indicate the 5, 10, and 15 mg·mL^{-1} of GO content in aqueous solution, respectively.

Fig. 7-1 (a) shows EDA-rGOH-5 after crosslinking, and its porous microstructure observed by SEM is shown in Fig. 7-1 (b).

To fabricate rGOH with VC, all steps were the same as the EDA-rGOH case, except that 10 mg of VC was dispersed into 10 mL GOs with concentrations of 5 mg·mL^{-1} initially, and the reaction was performed for 24 hr at 80℃, which was named as VC-rGOH-5 [191].
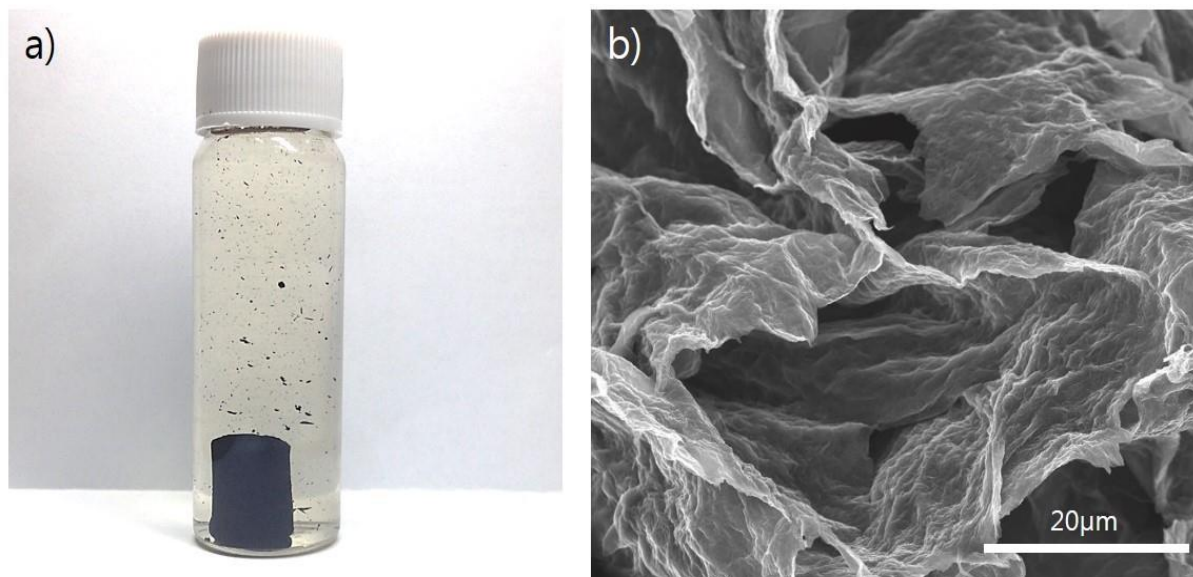
Figure 7-1 (a) EDA-rGOH-5 contained in water after crosslinking reaction and (b) SEM image shows its porous microstructure.

7. 2. 2 Characterization

The crystal structure of sample was characterized by X-ray diffraction system (XRD, Rigaku, D/MAZX 2500V/PC) using a high power X-ray diffractometer with Cu-Kα radiation (35 kV, 20 mA, λ = 1.5418 Å) at a scan rate of 2° (2θ) per minute. XPS (K-Alpha, ThermoFisher Scientific ESCALAB 250Xi) were recorded using an Al Kα X-ray source (1486.6 eV), and Raman spectra were measured from 200 to 3,500 cm^{-1} using a DXR Raman microscope (Thermo Scientific) with a 633 nm incident laser source. The bulk structures of the composites were analyzed using cross-sectional images obtained by a field emission-scanning electron microscope (FE-SEM, JOEL JSM-6500FE). The specific surface area was measured with surface area and porosity analyzer (Micromeritics, ASAP 2020) and calculated

using the BET equation. The electrical responses of graphene hydrogels subjected to compressive stresses were measured using a universal materials testing system under compressive test mode. A digital multimeter was used to enable *in situ* measurement of electrical resistance change while compressive strains are induced.

7. 3 Results and Discussion

7. 3. 1 Functionalized Graphene Oxide

XPS was used to analyze the chemical composition and oxidation status of carbon in EDA-rGOHs and VC-rGOH. As shown in Fig. 7-2, the N 1s peak was observed at 399.1 eV in the EDA-rGOHs by the reaction between EDA and GO, which was not the case for VC-rGOH. The single N 1s peak indicated that nearly all of the nitrogen atoms exist in the form of C-NH-C bonds, which confirms the reaction between amine of EDA and epoxy or carboxyl acid of GO. As shown in Fig. 7-1 (a), VC-rGOH-5 shows five characteristic C 1s peaks at 284.5, 285.5, 286.7, 287.9 and 289.1 eV which correspond to sp2 C, sp3 C, C-O (epoxy and alkoxy), C=O (carbonyl) and –O–C=O (carboxylic acid), respectively [192-194]. From the Fig. 7-2 (b-c), the absence of carboxylic acid in EDA-rGOHs also indicates the formation of amide group by the reaction between amine in EDA and carboxylic acid in GO. Both EDA-rGOHs and VC-rGOH showed significant loss in the oxygen related functional groups, but EDA-rGOHs possessed more sp^2 C than that of VC-rGOH, which indicates better reduction of functional groups and more restoration of C=C in GO by the EDA [195].

The change of the interlayer spacing of each sample was investigated by XRD. As shown in Fig. 7-3 (a), the characteristic diffraction peaks of graphite, GO, EDA-rGOH, and VC-rGOH appeared at $2\theta = 26.3°$, $2\theta = 9.78°$, $2\theta = 25.0°$, and $2\theta = 25.86°$, which correspond to the interlayer spacings of 3.34 Å, 9.04 Å, 3.56 Å, and 3.44 Å, respectively. The highly increased interlayer spacing of GO after oxidation can be attributed to the enriched functional groups and captured water molecules [196]. The slightly larger interlayer spacing of EDA-rGOH than that of VC-rGOH can be attributed to the EDA linkages present between GO sheets after crosslinking reaction between GO and EDA [195].

As shown in Fig. 7-3 (b), the two distinct peaks around 1358 cm^{-1} and 1595 cm^{-1} in the Raman spectra can be attributed to the diamondoid and graphitic structures of graphene. The intensity ratio of the D and G bands (I_D/I_G) increased from 0.9 for GO [193] to 1.36 for rGOH, which indicates the restoration of the C=C bonds because of the dehydration of the oxygen-related functional groups in GO.
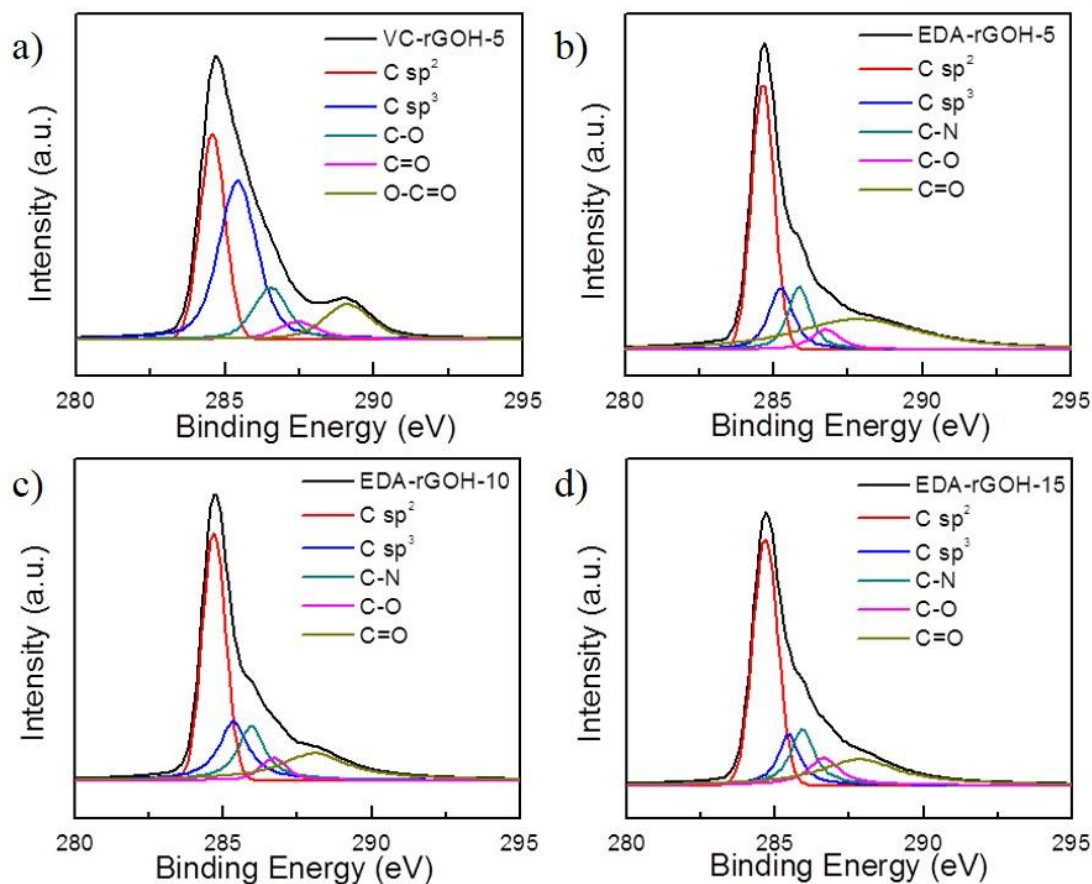
Figure 7-2 C 1s binding region of (a) VC-rGOH-5, (b) EDA-rGOH-5, (c) EDA-rGOH-10 and (d) EDA-rGOH-15 were taken from XPS spectra.
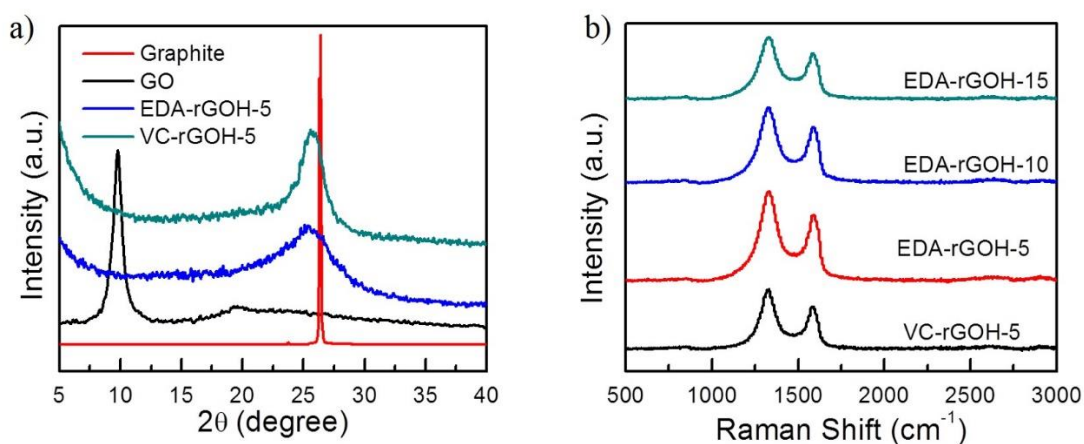
Figure 7-3 (a) Characteristic X-ray diffraction patterns of graphite, GO, EDA-rGOH-5, VC-rGOH-5 and (b) Raman spectra of VC, EDA-rGOH.

7. 3. 2 Morphology and Microstructure of Functionalized Graphene Oxide Hydrogel

The pore structures of EDA-rGOHs and VC-rGOH were analyzed by BET apparatus. As shown in

Fig. 7-4, all samples show distinct H_2 type adsorption and desorption isotherms, indicating the formation

70

of a mesoporous structure that has connected or non-connected ink-bottle pores or cavities due to the crosslinking reaction in EDA-rGOHs and due to the restored π-π interactions between rGO sheets in VC-rGOH [196-198]. As summarized in Table 7-1, the BET surface area and pore volume increased as the GO concentration increased for ethylene-diamine used. With EDA-rGOH-15, the largest surface area obtained for the GO hydrogel in this study was 745 $m^2 \cdot g^{-1}$. The bulk density of VC-rGOH was obtained higher value than EDA-rGOH due to the influence of the interlayer spacing and pore size.

SEM images of EDA-rGOH-5 and VC-rGOH-5 with low and high magnification are shown in Fig. 7-5. From the comparison of its microstructure between EDA-rGOH-5 and VC-rGOH-5, both low and high magnification images clearly indicating larger pore and particle size of EDA-rGOH-5 compared to that of VC-rGOH-5. This observation was also supported by the summarized BET results shown in Table 7-1.
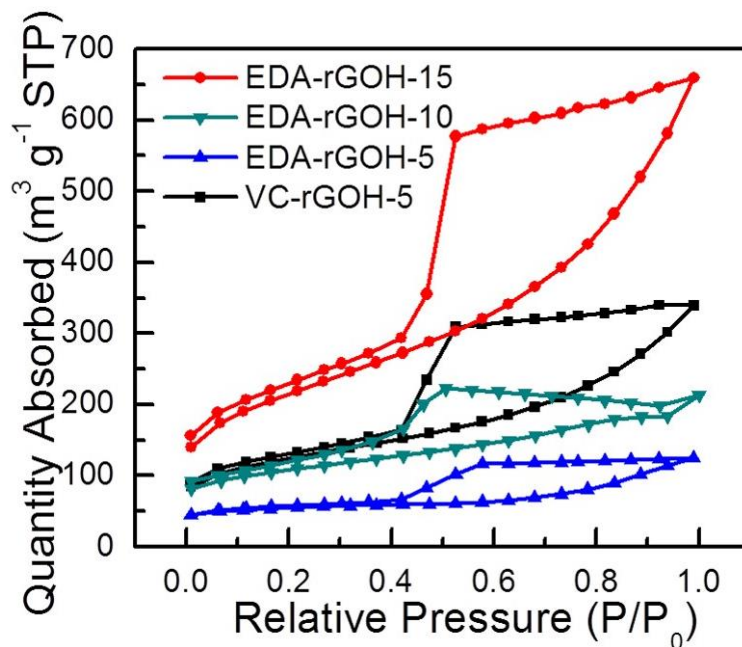

Figure 7-4 Nitrogen gas sorption isotherm for VC-rGOH and EDA-rGOH.

Table 7-2 The BET surface area and pore size of EDA-rGOH and VC-rGOH.

Sample	VC-rGOH-5	EDA-rGOH-5	EDA-rGOH-10	EDA-rGOH-15
BET surface area (m^2/g)	285	174	293	745
Pore size (nm)	46	68	54	47
Bulk density (mg/ml)	20.44	17.52	19.02	19.9
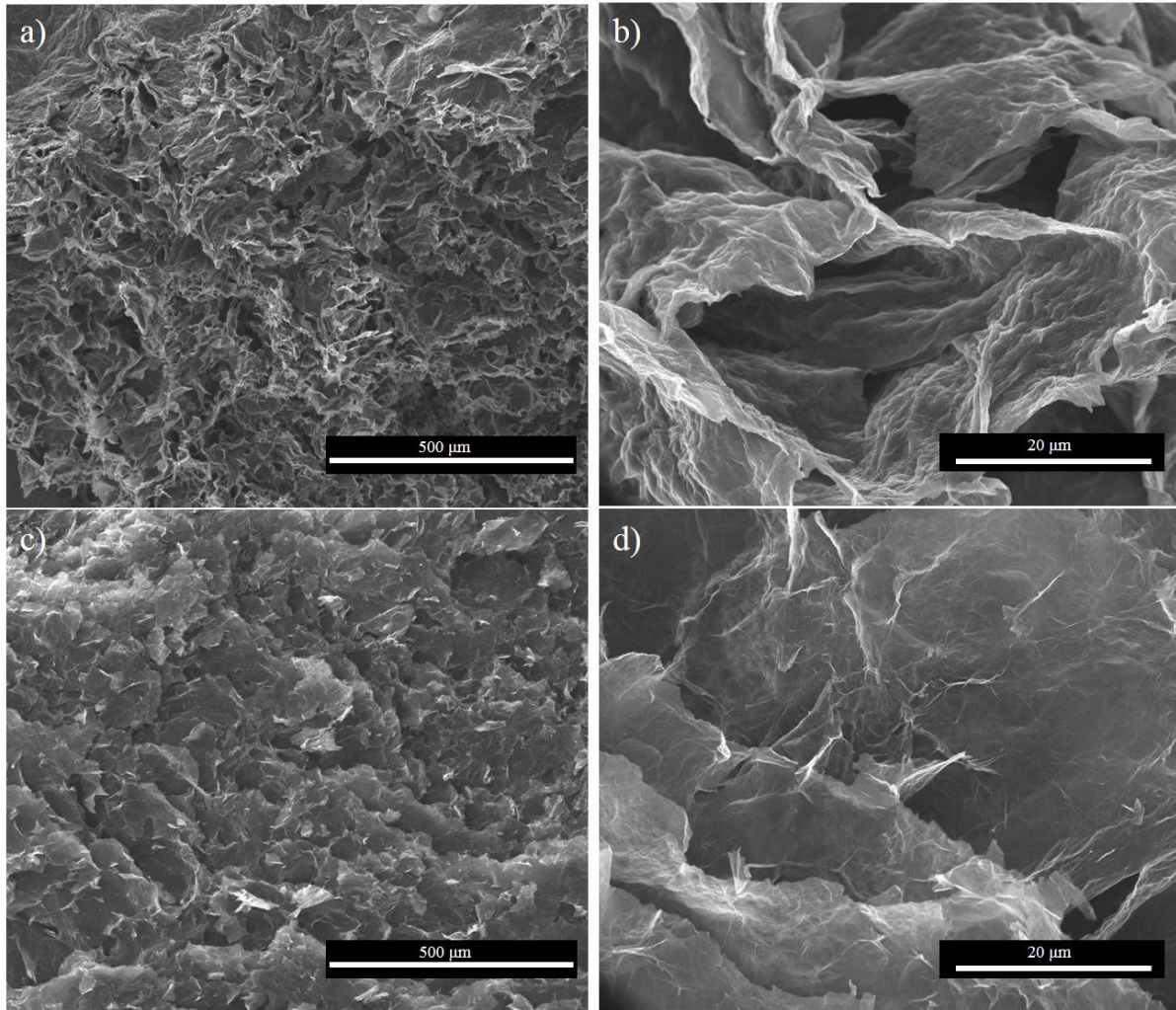
Figure 7-5 High and low magnification SEM images of (a, b) EDA-rGOH-5 and (c, d) VC-rGOH-5.

7. 3. 3 Piezoresistive Behavior of Functionalized Graphene Oxide Hydrogel

Simple attachment and characterization set-up for electromechanical test of rGOH is shown in Fig. 7-6. Electromechanical tests were performed for EDA-rGOH and VC-rGOH hydrogel under static and cyclic compressive strains. The resistance change due to compression-induced densification of porous materials showed unique piezoresistive behavior dependent on pore size and bulk density.

The piezoresistive behavior of EDA-rGOH-5 and VC-rGOH-5 subjected to different cyclic compression frequencies at an amplitude of 2.5% strain is shown in Fig. 7-7. From the (a) slow (6.5% $\cdot$min^{-1}) cyclic compressive strain, both VC-rGOH-5 and EDA-rGOH-5 showing well-matched resistance change without retardation effect. However, with increased frequency of (b) 13 % $\cdot$min^{-1} and (c) 31.25 % $\cdot$min^{-1}, phase difference of EDA-rGOH-5 increased from 0.8 sec for 13% $\cdot$min^{-1} to 1.4 sec for 31.25% $\cdot$min^{-1} while the resistance change pattern of VC-rGOH-5 are preserved without retardation. The phase difference observed from EDA-rGOH-5 clearly reflects its large pore size and low bulk density, which makes it behave less elastically. As shown in Fig. 7-8, a similar pore-size-driven piezoresistive phase difference was observed from EDA-rGOH with different EDA concentration. On

the basis of BET results, more densely populated conductive network formed by higher crosslinking density consequently influenced not only the degree of phase difference but also sensitivity.

Static compressive strain with a strain rate of 6.5% $\cdot cm^{-1}$ was applied to VC and EDA-rGOHs, and their compressive stress as well as resistance change was monitored. As shown in Fig. 7-9 (a), VC-rGOH-5 shows higher compressive modulus and resistance change compared to that of EDA-rGOH-5 because of their pore size and bulk density. Since the porous material generally shows strain hardening behavior under compression, their piezoresistive behavior inconsistently exhibit nonlinear tendency. The initial region of resistance change under compressive strain strongly reflects the bulk density of rGOH; therefore, EDA-rGOH-5 exhibits the highest sensitivity (gauge factor) of 7.98. From Fig. 7-9 (b), EDA-rGOH-10 and 15 shows a similar initial gauge factor around 4.9, which is also similar to that of VC-rGOH-5 (4.87). Hence, it is noted that EDA-rGOH-10, EDA-rGOH-15 and VC-rGOH-5 exhibit similar initial piezoresistive behavior because of their similar bulk density regardless of their surface area and pore size.

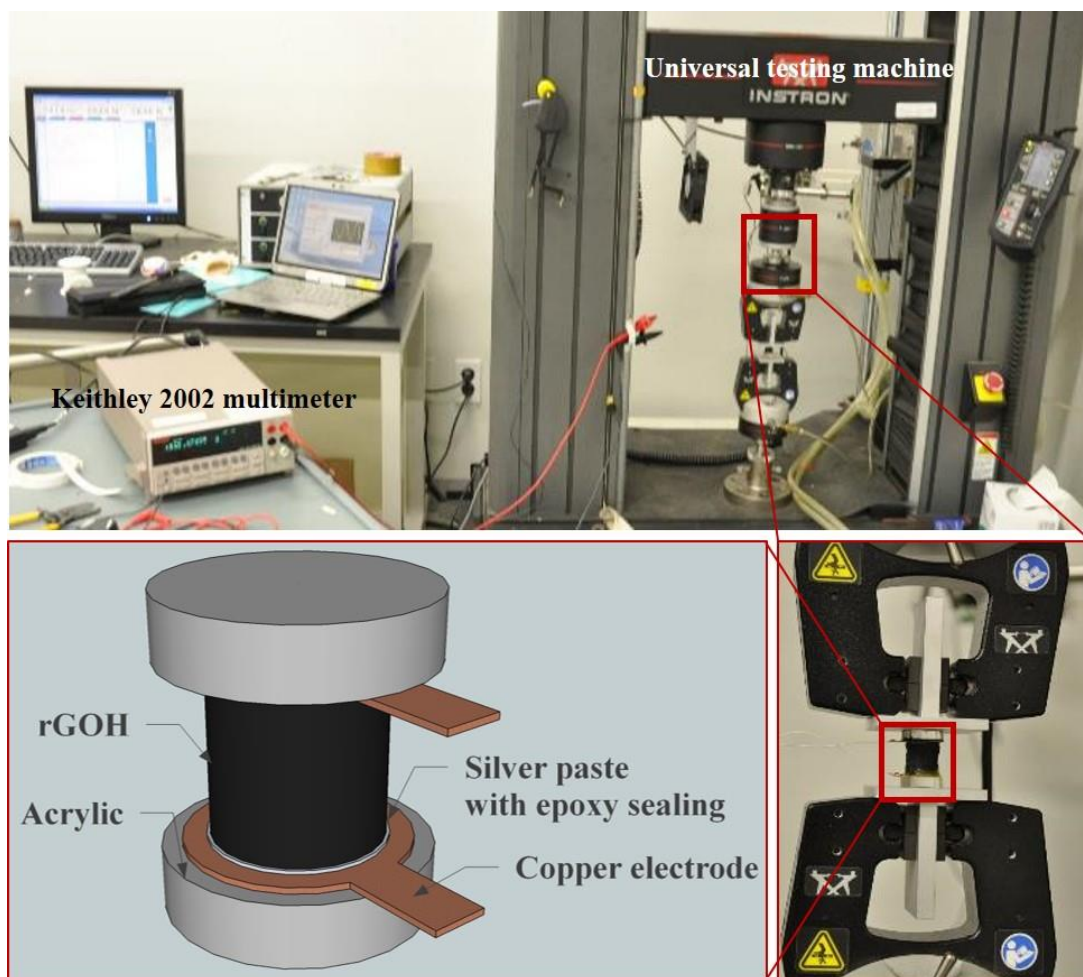**Figure 7-6** Piezoresistive behavior measurement set-up for rGOH.

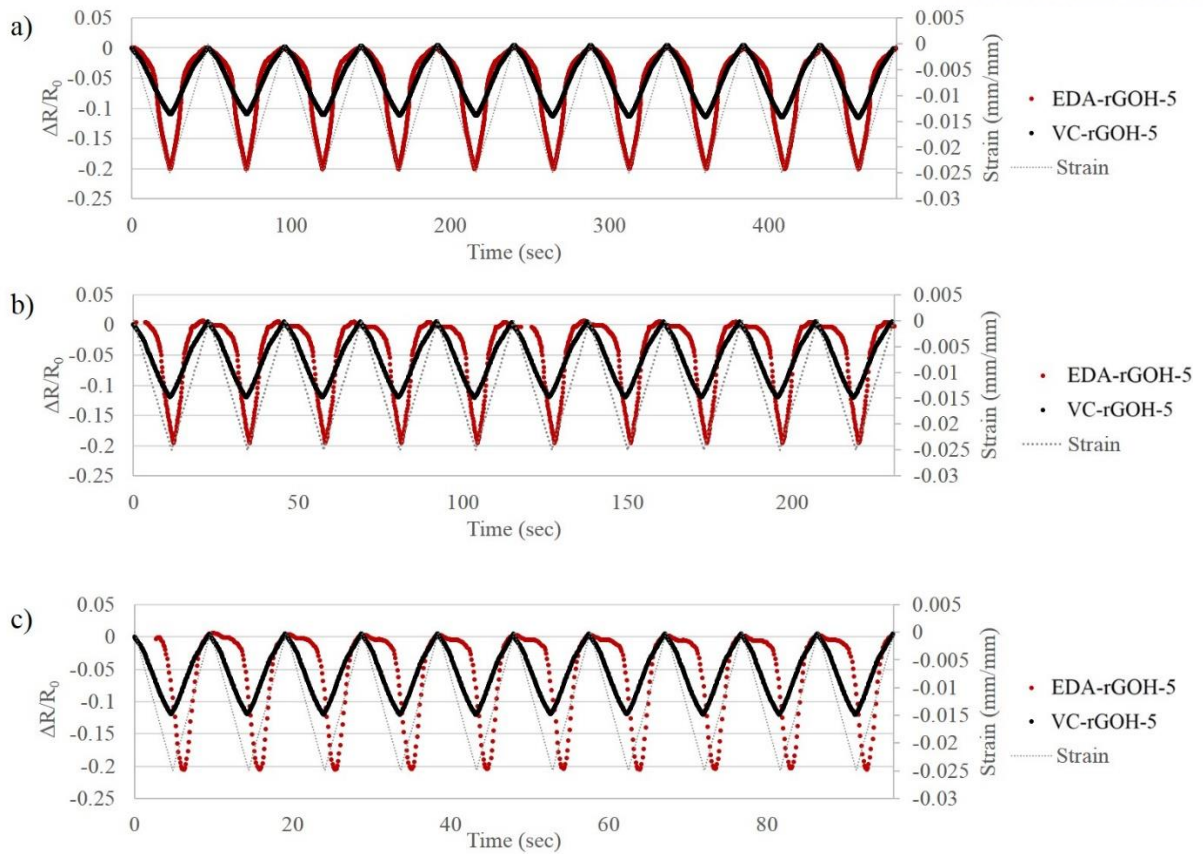**Figure 7-7** Cyclic compressive strain induced resistance change of EDA-rGOH-5 and VC-rGOH-5 with strain frequency of (a) 6.5 % ·min⁻¹, (b) 13 % ·min⁻¹ and (c) 31.25 % ·min⁻¹, respectively.
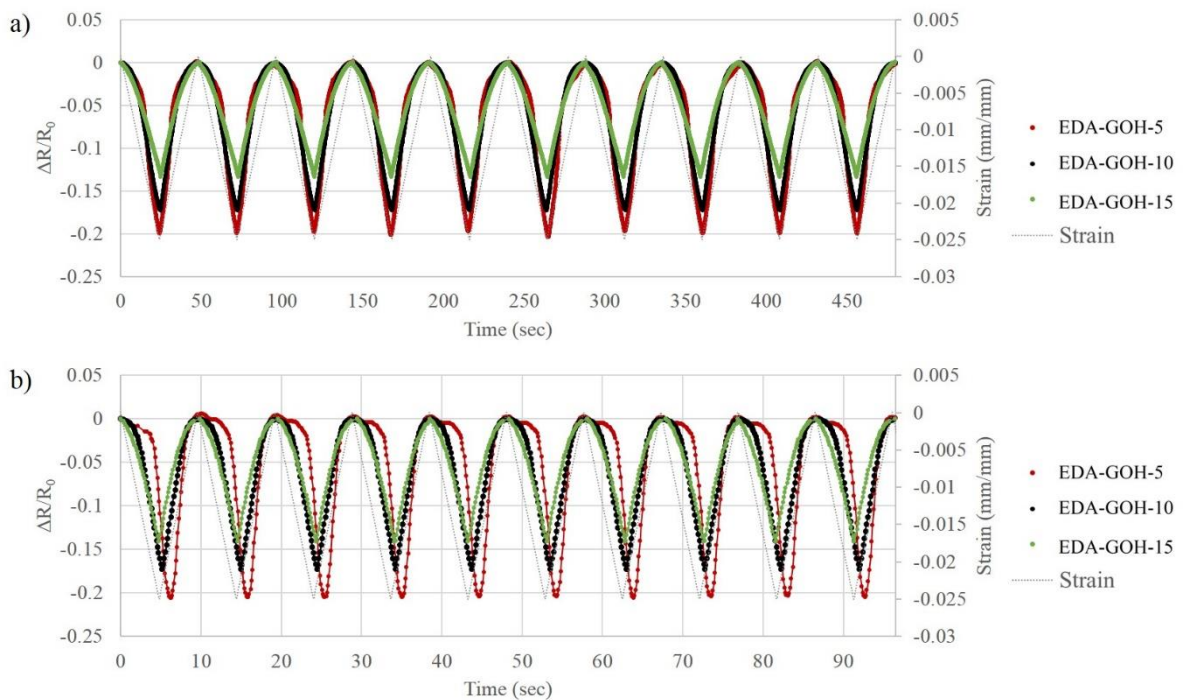

Figure 7-8 Cyclic compressive strain induced resistance change of EDA-rGOHs with strain frequency of (a) 6.5 % ·min⁻¹ and (b) 31.25 % ·min⁻¹.
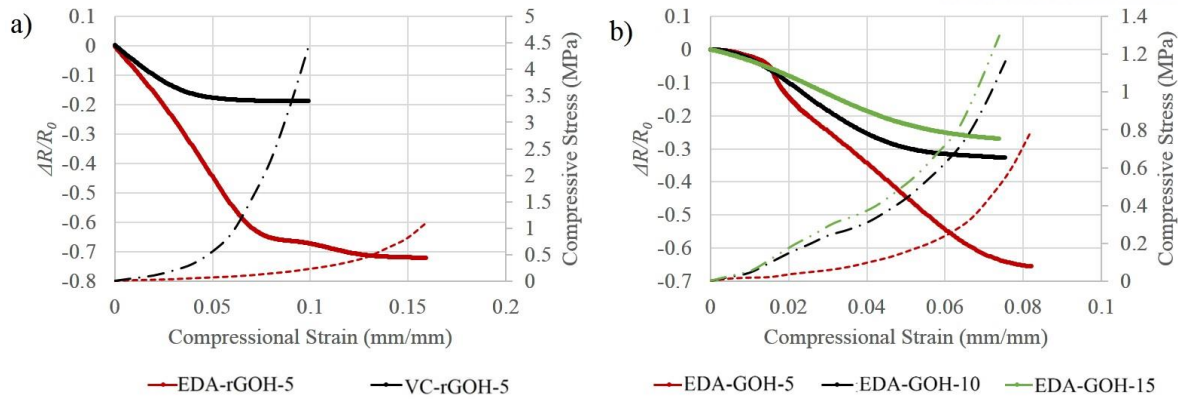
Figure 7-9 Piezoresistive behavior (straight lines) and s-s curve (dashed lines) of (a) EDA and VC functionalized rGOH and (b) EDA-rGOH with EDA concentration under static compressive strain with strain rate of 6.5% ·cm^{-1}.

7. 4 Part Summary – Porosity or Chemical Bonding Density vs Piezoresistive Behavior

EDA and Vitanine C (VC) were used as functionalization and crosslinking agents for fabrication of graphene oxide hydrogel (rGOH). From the C 1s region of XPS spectra, both EDA and VC covalently bridged between GO to form rGOH and increased 2θ peaks observed from the XRD spectra of VC and EDA-rGOH indicating hydrothermal reaction derived not just re-aggregation but also restacking of GO sheets. Raman spectra of VC and EDA-rGOH exhibit increased I_D/I_G ratio of 1.36 compared to that of GO (0.9), which indicates hydrothermal process partially restored sp^2 graphene structure.

The microstructures of VC and EDA-rGOH were characterized using BET and SEM. BET results showed a mesoporous structural characteristic with increased pore volume as the GO concentration increased for ethylene-diamine used. With EDA-rGOH-15, the largest surface area obtained for the GO hydrogel was 745 m^2·g^{-1}. The bulk density of VC-rGOH was higher than that of EDA-rGOH due to the influence of the interlayer spacing and pore size. The difference in the morphology between VC and EDA-rGOH observed using SEM also confirmed their pore size and bulk density.

Mechanical behavior under cyclic and static compressive strain and porosity of rGOHs consequently resulted in their piezoresistive behavior. Because the large pore size and high bulk density, EDA-rGOH-5 exhibited the highest phase difference of 1.4 sec from the cyclic compressive strain as well as the highest gauge factor of 7.98 from initial region of the piezoresistive behavior under static compressive strain.

VIII. CONCLUSIONS

This thesis presented a systematic approach to design and optimize wide-area structural sensing systems for various applications. Four complementary and unique experiments were conducted with consideration of mechanical durability, accuracy, cost effectiveness and sensor dimensionality. This chapter presents general conclusions, limitations, as well as future work.

8. 1 Conclusions

The knowledge base associated with the CNMs and their composites has expanded greatly in recent years. This field of research has been aimed at both tailoring their mechanical and physical properties as well as developing intelligent systems that enable sensor and actuator systems. Significant challenges exist in the development of such smart materials that are capable of self-sensing and active response, for example, efficient growth of macroscopic-length CNTs, controlled growth of CNTs on desired substrates, durability and accuracy of nanotube based sensors, homogeneous dispersion of CNTs in polymer matrices and the control of their alignment, and the large scale fabrication of sensors based on nanocomposites.

Furthermore, for the development of CNM-based composite strain sensing systems with large-area and multi-dimensional sensing capabilities, fundamental knowledge on their structure-property relations is also necessary. In a nanocomposite for macroscopic applications, the characteristic length scale can range from several nanometers to several orders of magnitude, hence highlighting the need to develop on the basis of both individual and colligative properties to bridge these scales toward optimization. For example, from the electromechanical coupling of individual CNMs to the broad range of composite deformation, the behavior of CNM-based strain sensors involved multiple phenomena at length scale hierarchies ranging from the atomic and nanoscale to the macroscopic scale.

Based on this fact, we designed and conducted four types of research from the different nanoscale characteristics, such as nanomaterials shape, polymer-CNM interface or porosity to macroscopic characteristics such as piezoresistive behavior and humidity driven resistance change.

In Chapter 4, the effects of CNM shape and dimensions on piezoresistive behavior were studied using CNT-xGnP hybrid sheets. The free-standing CNM hybrid sheets, consisting of MWCNTs, xGnPs of different lengths and lateral dimensions, have been prepared using various material combinations and compositions. When subjected to tensile strains, the carbon nanomaterial sheets showed piezoresistive behavior, characterized by a change in electrical resistance with applied strain. Simultaneous measurement of resistance changes among multiple electrodes placed on the periphery of the hybrid sheets showed the dependence of resistance changes on strain direction, which potentially allows multi-directional strain sensing and deformation geometry reconstruction in 2D. Various combinations of MWCNT length, xGnP size and MWCNT-to-xGnP ratio result in different specific

surface areas and nanoparticle interactions, which serve as critical factors for controlling the sensitivity of hybrid sheets. The smaller the nanoplatelet size and the higher the content as compared to MWCNT, the higher the sensitivity. These inherently porous sheets were impregnated with polycarbonate by infiltrating a polycarbonate–chloroform solution through the sheets. SEM analyses revealed that combining nanomaterials of various sizes and dimensions can serve as a means to control the porous network structure, which allows controlled polymer impregnation and tailored strain sensitivity. The wide-area strain sensing ability of the polymer-impregnated composite sheets was demonstrated by subjecting the composites with multiple electrodes to a flexural load and measuring the piezoresistivity *in situ.* The study demonstrated successful hybridization of 1D fiber-like and 2D platelet-like carbon nanomaterials into freestanding sheets with controlled nanostructure and properties, which can be used as preforms for easy-to-handle, high-carbon-content, multi-functional composite sheets.

In Chapter 5, rGO-coated epoxy films with covalently bonded interface between rGO and epoxy were studied. The effects of interfacial bonding on piezoresistive behavior were mainly studied. The key finding in this chapter is that strain sensitivity was tuned by controlling the thickness and density of the graphene layer as well as the interfacial adhesion force between graphene and the substrate. Chemically reducing the graphene oxide, thereby maximizing its adhesion to the substrate, while minimizing the coating density and thickness, resulted in excellent transparency and high gauge factors. The fabrication method presented allows design optimization of transparent, high-performance, and sensitivity-tunable piezoresistive sensors, which can make inroads into such applications as wide-area strain sensors, self-sensing flexible electronics, and intelligent structural health monitoring.

Chapter 6 demonstrated polydopamine treated GO – PVA composite films with increased water resistance and tensile toughness mainly because of their strong hydrogen bonding between dGO and PVA matrix. Percolated conductive networks formed by partially reduced dGO enables conductometric humidity sensor. Experimental procedure for preparation of dGO was simply carried out with the aqueous solution and then chemically reduced to yield polydopamine treated reduced GO. A combination of hydrogen bonding, strong adhesion of polydopamine at the interface of PVA and GO sheets, and reinforcement by GO resulted in increases in tensile modulus, ultimate tensile strength, and strain-to-failure by 39, 100, and 89%, respectively, at 0.5 wt % dGO loading of the PVA. The dGO serves as a moisture barrier for water-soluble PVA, and the dGO/PVA composite films were shown to be effective humidity sensors over the relative humidity range 40-100%.

Finally, we focused on the controlled pore size and density of graphene hydrogel using different crosslinking agents and concentrations. The pore size and density characterized using BET exhibit mesoporous interconnected nanometer scale domains, and size was decreased with crosslinking agent concentration and reactivity. Mechanical behavior under cyclic and static compressive strain and porosity of rGOHs consequently resulted in their piezoresistive behavior. Because of large pore size and high bulk density, EDA-rGOH-5 exhibited the highest phase difference of 1.4 sec from the cyclic

compressive strain as well as the highest gauge factor of 7.98 from initial region of the piezoresistive behavior under static compressive strain.

8. 2 Future Work

The last enhancement for this experimental approach is to support experimental results using theoretically well-defined computational modeling. In spite of existing empirical results, the fundamental understanding of piezoresistive behavior in a CNM based polymer nanocomposite is still lacking, largely due to less effort being put into theoretical and numerical investigations.

Reference

1. Thostenson, E. T.; Li, C.; Chou, T.-W. Nanocomposites in context. *Composites Science and Technology* 2005, 65, 491-516.

2. Hussain, F.; Hojjati, M.; Okamoto, M.; Gorga, R. E. Review article: Polymer-matrix Nanocomposites, Processing, Manufacturing, and Application: An Overview. *Journal of Composite Materials* 2006, 40, 1511-1575.

3. Kumar, S. K.; Krishnamoorti, R. Nanocomposites: Structure, Phase Behavior, and Properties. *Annual Review of Chemical and Biomolecular Engineering* 2010, 1, 37-58.

4. Ma, P.-C.; Siddiqui, N. A.; Marom, G.; Kim, J.-K. Dispersion and functionalization of carbon nanotubes for polymer-based nanocomposites: A review. *Composites Part A: Applied Science and Manufacturing* 2010, 41, 1345-1367.

5. Li, Y.; Wang, W.; Liao, K.; Hu, C.; Huang, Z.; Feng, Q. Piezoresistive effect in carbon nanotube films. *Chin. Sci. Bull.* 2003, 48, 125-127.

6. Dang, Z.-M.; Jiang, M.-J.; Dan, X.; Yao, S.-H.; Zhang, L.-Q.; Bai, J. Supersensitive linear piezoresistive property in carbon nanotubes/silicone rubber nanocomposites. *Journal of Applied Physics* 2008, 104, 024114-024114-6.

7. Gang Yin; Ning Hu; Karube, Y.; Yaolu Liu; Yuan Li; Fukunaga, H. A carbon nanotube/polymer strain sensor with linear and anti-symmetric piezoresistivity. *Journal of Composite Materials* 2011, 45, 1315-1323.

8. Kang, I.; Heung, Y. Y.; Kim, J. H.; Lee, J. W.; Gollapudi, R.; Subramaniam, S.; Narasimhadevara, S.; Hurd, D.; Kirikera, G. R.; Shanov, V.; Schulz, M. J.; Shi, D.; Boerio, J.; Mall, S.; Ruggles-Wren, M. Introduction to carbon nanotube and nanofiber smart materials. *Composites Part B: Engineering* 2006, 37, 382-394.

9. Merkoçi, A.; Pumera, M.; Llopis, X.; Pérez, B.; del Valle, M.; Alegret, S. New materials for electrochemical sensing VI: Carbon nanotubes. *TrAC Trends in Analytical Chemistry* 2005, 24, 826-838.

10. Wang, J. Carbon-Nanotube Based Electrochemical Biosensors: A Review. *Electroanalysis* 2005, 17, 7-14.

11. Ramasubramaniam, R.; Chen, J.; Liu, H. Homogeneous carbon nanotube/polymer composites for electrical applications. *Applied Physics Letters* 2003, 83, 2928-2930.

12. Qu, S.; Wong, S.-C. Piezoresistive behavior of polymer reinforced by expanded graphite. *Composites Science and Technology* 2007, 67, 231-237.

13. Loh, K. J.; Lynch, J. P.; Shim, B. S.; Kotov, N. A. Tailoring Piezoresistive Sensitivity of Multilayer Carbon Nanotube Composite Strain Sensors. *Journal of Intelligent Material Systems and Structures* 2008, 19, 747-764.

14. Hu, N.; Karube, Y.; Arai, M.; Watanabe, T.; Yan, C.; Li, Y.; Liu, Y.; Fukunaga, H. Investigation on sensitivity of a polymer/carbon nanotube composite strain sensor. *Carbon* 2010, 48, 680-687.

15. Inpil, K.; Mark, J. S.; Jay, H. K.; Vesselin, S.; Donglu, S. A carbon nanotube strain sensor for structural health monitoring. *Smart Materials and Structures* 2006, 15, 737.

16. Böger, L.; Wichmann, M. H. G.; Meyer, L. O.; Schulte, K. Load and health monitoring in glass fibre reinforced composites with an electrically conductive nanocomposite epoxy matrix. *Composites Science and Technology* 2008, 68, 1886-1894.

17. Alexopoulos, N. D.; Bartholome, C.; Poulin, P.; Marioli-Riga, Z. Structural health monitoring of glass fiber

reinforced composites using embedded carbon nanotube (CNT) fibers. *Composites Science and Technology* 2010, 70, 260-271.

18. Eswaraiah, V.; Balasubramaniam, K.; Ramaprabhu, S. Functionalized graphene reinforced thermoplastic nanocomposites as strain sensors in structural health monitoring. *Journal of Materials Chemistry* 2011, 21, 12626-12628.

19. Bautista-Quijano, J. R.; Avilés, F.; Aguilar, J. O.; Tapia, A. Strain sensing capabilities of a piezoresistive MWCNT-polysulfone film. *Sensors and Actuators A: Physical* 2010, 159, 135-140.

20. Alamusi; Hu, N.; Fukunaga, H.; Atobe, S.; Liu, Y.; Li, J. Piezoresistive Strain Sensors Made from Carbon Nanotubes Based Polymer Nanocomposites. *Sensors* 2011, 11, 10691-10723.

21. Rein, M. D.; Breuer, O.; Wagner, H. D. Sensors and sensitivity: Carbon nanotube buckypaper films as strain sensing devices. *Composites Science and Technology* 2011, 71, 373-381.

22. Zhang, W.; Suhr, J.; Koratkar, N. Carbon Nanotube/Polycarbonate Composites as Multifunctional Strain Sensors. *Journal of Nanoscience and Nanotechnology* 2006, 6, 960-964.

23. Kang, I.; Joung, K. Y.; Choi, G.-R.; Schulz, M. J.; Choi, Y.-S.; Hwang, S.-H.; Ko, H. S. The Bulk Piezoresistive Characteristics of Carbon Nanotube Composites for Strain Sensing of Structures. *Journal of Nanoscience and Nanotechnology* 2007, 7, 3736-3739.

24. Myounggu, P.; Hyonny, K.; Jeffrey, P. Y. Strain-dependent electrical resistance of multi-walled carbon nanotube/polymer composite films. *Nanotechnology* 2008, 19, 055705.

25. Kim, Y.-J.; Cha, J. Y.; Ham, H.; Huh, H.; So, D.-S.; Kang, I. Preparation of piezoresistive nano smart hybrid material based on graphene. *Current Applied Physics* 2011, 11, S350-S352.

26. Thostenson, E. T.; Ren, Z.; Chou, T.-W. Advances in the science and technology of carbon nanotubes and their composites: a review. *Composites Science and Technology* 2001, 61, 1899-1912.

27. Gojny, F. H.; Wichmann, M. H. G.; Köpke, U.; Fiedler, B.; Schulte, K. Carbon nanotube-reinforced epoxy-composites: enhanced stiffness and fracture toughness at low nanotube content. *Composites Science and Technology* 2004, 64, 2363-2371.

28. Suhr, J.; Koratkar, N.; Keblinski, P.; Ajayan, P. Viscoelasticity in carbon nanotube composites. *Nat Mater* 2005, 4, 134-137.

29. Thostenson, E. T.; Li, W. Z.; Wang, D. Z.; Ren, Z. F.; Chou, T. W. Carbon nanotube/carbon fiber hybrid multiscale composites. *Journal of Applied Physics* 2002, 91, 6034-6037.

30. Wang, L.; Dang, Z.-M. Carbon nanotube composites with high dielectric constant at low percolation threshold. *Applied Physics Letters* 2005, 87, -.

31. Du, F.; Fischer, J. E.; Winey, K. I. Effect of nanotube alignment on percolation conductivity in carbon nanotube/polymer composites. *Physical Review B* 2005, 72, 121404.

32. Vigolo, B.; Coulon, C.; Maugey, M.; Zakri, C.; Poulin, P. An Experimental Approach to the Percolation of Sticky Nanotubes. *Science* 2005, 309, 920-923.

33. Huang, H.; Liu, C. H.; Wu, Y.; Fan, S. Aligned Carbon Nanotube Composite Films for Thermal Management. *Advanced Materials* 2005, 17, 1652-1656.

34. Biercuk, M. J.; Llaguno, M. C.; Radosavljevic, M.; Hyun, J. K.; Johnson, A. T.; Fischer, J. E. Carbon nanotube composites for thermal management. *Applied Physics Letters* 2002, 80, 2767-2769.

35. Wei, B. Q.; Vajtai, R.; Ajayan, P. M. Reliability and current carrying capacity of carbon nanotubes. *Applied*

Physics Letters 2001, 79, 1172-1174.

36. Baughman, R. H.; Cui, C.; Zakhidov, A. A.; Iqbal, Z.; Barisci, J. N.; Spinks, G. M.; Wallace, G. G.; Mazzoldi, A.; De Rossi, D.; Rinzler, A. G.; Jaschinski, O.; Roth, S.; Kertesz, M. Carbon Nanotube Actuators. *Science* 1999, 284, 1340-1344.

37. Tombler, T. W.; Zhou, C.; Alexseyev, L.; Kong, J.; Dai, H.; Liu, L.; Jayanthi, C. S.; Tang, M.; Wu, S.-Y. Reversible electromechanical characteristics of carbon nanotubes under local-probe manipulation. *Nature* 2000, 405, 769-772.

38. Nardelli, M. B.; Bernholc, J. Mechanical deformations and coherent transport in carbon nanotubes. *Physical Review B* 1999, 60, R16338-R16341.

39. Bigg, D. M.; Stutz, D. E. Plastic composites for electromagnetic interference shielding applications. *Polymer Composites* 1983, 4, 40-46.

40. Sandler, J. K. W.; Kirk, J. E.; Kinloch, I. A.; Shaffer, M. S. P.; Windle, A. H. Ultra-low electrical percolation threshold in carbon-nanotube-epoxy composites. *Polymer* 2003, 44, 5893-5899.

41. Moisala, A.; Li, Q.; Kinloch, I. A.; Windle, A. H. Thermal and electrical conductivity of single- and multi-walled carbon nanotube-epoxy composites. *Composites Science and Technology* 2006, 66, 1285-1288.

42. Bryning, M. B.; Islam, M. F.; Kikkawa, J. M.; Yodh, A. G. Very Low Conductivity Threshold in Bulk Isotropic Single-Walled Carbon Nanotube–Epoxy Composites. *Advanced Materials* 2005, 17, 1186-1191.

43. Thostenson, E. T.; Chou, T.-W. Processing-structure-multi-functional property relationship in carbon nanotube/epoxy composites. *Carbon* 2006, 44, 3022-3029.

44. Stauffer, D. A. A. *Introduction to percolation theory*. Taylor & Francis: London; Philadelphia, 1998.

45. Li, C.; Chou, T.-W. Continuum percolation of nanocomposites with fillers of arbitrary shapes. *Applied Physics Letters* 2007, 90, -.

46. Coleman, J. N.; Curran, S.; Dalton, A. B.; Davey, A. P.; McCarthy, B.; Blau, W.; Barklie, R. C. Percolation-dominated conductivity in a conjugated-polymer-carbon-nanotube composite. *Physical Review B* 1998, 58, R7492-R7495.

47. Schadler, L. S.; Giannaris, S. C.; Ajayan, P. M. Load transfer in carbon nanotube epoxy composites. *Applied Physics Letters* 1998, 73, 3842-3844.

48. Qian, D.; Dickey, E. C.; Andrews, R.; Rantell, T. Load transfer and deformation mechanisms in carbon nanotube-polystyrene composites. *Applied Physics Letters* 2000, 76, 2868-2870.

49. Gojny, F. H.; Wichmann, M. H. G.; Fiedler, B.; Kinloch, I. A.; Bauhofer, W.; Windle, A. H.; Schulte, K. Evaluation and identification of electrical and thermal conduction mechanisms in carbon nanotube/epoxy composites. *Polymer* 2006, 47, 2036-2045.

50. Kilbride, B. E.; Coleman, J. N.; Fraysse, J.; Fournet, P.; Cadek, M.; Drury, A.; Hutzler, S.; Roth, S.; Blau, W. J. Experimental observation of scaling laws for alternating current and direct current conductivity in polymer-carbon nanotube composite thin films. *Journal of Applied Physics* 2002, 92, 4024-4030.

51. McNally, T.; Pötschke, P.; Halley, P.; Murphy, M.; Martin, D.; Bell, S. E. J.; Brennan, G. P.; Bein, D.; Lemoine, P.; Quinn, J. P. Polyethylene multiwalled carbon nanotube composites. *Polymer* 2005, 46, 8222-8232.

52. Ahmad, K.; Pan, W.; Shi, S.-L. Electrical conductivity and dielectric properties of multiwalled carbon nanotube and alumina composites. *Applied Physics Letters* 2006, 89, -.

53. Stadermann, M.; Papadakis, S. J.; Falvo, M. R.; Novak, J.; Snow, E.; Fu, Q.; Liu, J.; Fridman, Y.; Boland, J. J.; Superfine, R.; Washburn, S. Nanoscale study of conduction through carbon nanotube networks. *Physical Review B* 2004, 69, 201402.

54. Buldum, A.; Lu, J. P. Contact resistance between carbon nanotubes. *Physical Review B* 2001, 63, 161403.

55. Holm, R. The Electric Tunnel Effect across Thin Insulator Films in Contacts. *Journal of Applied Physics* 1951, 22, 569-574.

56. Li, C.; Thostenson, E. T.; Chou, T.-W. Dominant role of tunneling resistance in the electrical conductivity of carbon nanotube–based composites. *Applied Physics Letters* 2007, 91, -.

57. Martin, C. A.; Sandler, J. K. W.; Shaffer, M. S. P.; Schwarz, M. K.; Bauhofer, W.; Schulte, K.; Windle, A. H. Formation of percolating networks in multi-wall carbon-nanotube–epoxy composites. *Composites Science and Technology* 2004, 64, 2309-2316.

58. Li, J.; Ma, P. C.; Chow, W. S.; To, C. K.; Tang, B. Z.; Kim, J. K. Correlations between Percolation Threshold, Dispersion State, and Aspect Ratio of Carbon Nanotubes. *Advanced Functional Materials* 2007, 17, 3207-3215.

59. Haggenmueller, R.; Gommans, H. H.; Rinzler, A. G.; Fischer, J. E.; Winey, K. I. Aligned single-wall carbon nanotubes in composites by melt processing methods. *Chemical Physics Letters* 2000, 330, 219-225.

60. Choi, E. S.; Brooks, J. S.; Eaton, D. L.; Al-Haik, M. S.; Hussaini, M. Y.; Garmestani, H.; Li, D.; Dahmen, K. Enhancement of thermal and electrical properties of carbon nanotube polymer composites by magnetic field processing. *Journal of Applied Physics* 2003, 94, 6034-6039.

61. Du, F.; Fischer, J. E.; Winey, K. I. Coagulation method for preparing single-walled carbon nanotube/poly(methyl methacrylate) composites and their modulus, electrical conductivity, and thermal stability. *Journal of Polymer Science Part B: Polymer Physics* 2003, 41, 3333-3338.

62. Novoselov, K. S.; Geim, A. K.; Morozov, S. V.; Jiang, D.; Zhang, Y.; Dubonos, S. V.; Grigorieva, I. V.; Firsov, A. A. Electric Field Effect in Atomically Thin Carbon Films. *Science* 2004, 306, 666-669.

63. Scarpa, F.; Adhikari, S.; Phani, A. S. Effective elastic mechanical properties of single layer graphene sheets. *Nanotechnology* 2009, 20, 065709.

64. Castro Neto, A. H.; Guinea, F.; Peres, N. M. R.; Novoselov, K. S.; Geim, A. K. The electronic properties of graphene. *Reviews of Modern Physics* 2009, 81, 109-162.

65. Xu, X.; Pereira, L. F. C.; Wang, Y.; Wu, J.; Zhang, K.; Zhao, X.; Bae, S.; Tinh Bui, C.; Xie, R.; Thong, J. T. L.; Hong, B. H.; Loh, K. P.; Donadio, D.; Li, B.; Ö zyilmaz, B. Length-dependent thermal conductivity in suspended single-layer graphene. *Nat Commun* 2014, 5.

66. Huang, X.; Qi, X.; Boey, F.; Zhang, H. Graphene-based composites. *Chemical Society Reviews* 2012, 41, 666-686.

67. Kuilla, T.; Bhadra, S.; Yao, D.; Kim, N. H.; Bose, S.; Lee, J. H. Recent advances in graphene based polymer composites. *Progress in Polymer Science* 2010, 35, 1350-1375.

68. Jang, B. Z.; Zhamu, A. Processing of nanographene platelets (NGPs) and NGP nanocomposites: a review. *J Mater Sci* 2008, 43, 5092-5101.

69. Hansma, P. K.; Turner, P. J.; Ruoff, R. S. Optimized adhesives for strong, lightweight, damage-resistant, nanocomposite materials: new insights from natural materials. *Nanotechnology* 2007, 18, 044026.

70. RamanathanT; Abdala, A. A.; StankovichS; Dikin, D. A.; Herrera Alonso, M.; Piner, R. D.; Adamson, D. H.; Schniepp, H. C.; ChenX; Ruoff, R. S.; Nguyen, S. T.; Aksay, I. A.; Prud'Homme, R. K.; Brinson, L. C.

82

Functionalized graphene sheets for polymer nanocomposites. *Nat Nano* 2008, 3, 327-331.

71. Yu, A.; Ramesh, P.; Itkis, M. E.; Bekyarova, E.; Haddon, R. C. Graphite Nanoplatelet−Epoxy Composite Thermal Interface Materials. *The Journal of Physical Chemistry C* 2007, 111, 7565-7569.

72. Liu, Z.-B.; Xu, Y.-F.; Zhang, X.-Y.; Zhang, X.-L.; Chen, Y.-S.; Tian, J.-G. Porphyrin and Fullerene Covalently Functionalized Graphene Hybrid Materials with Large Nonlinear Optical Properties. *The Journal of Physical Chemistry B* 2009, 113, 9681-9686.

73. Booth, T. J.; Blake, P.; Nair, R. R.; Jiang, D.; Hill, E. W.; Bangert, U.; Bleloch, A.; Gass, M.; Novoselov, K. S.; Katsnelson, M. I.; Geim, A. K. Macroscopic Graphene Membranes and Their Extraordinary Stiffness. *Nano Letters* 2008, 8, 2442-2446.

74. Watcharotone, S.; Dikin, D. A.; Stankovich, S.; Piner, R.; Jung, I.; Dommett, G. H. B.; Evmenenko, G.; Wu, S.-E.; Chen, S.-F.; Liu, C.-P.; Nguyen, S. T.; Ruoff, R. S. Graphene−Silica Composite Thin Films as Transparent Conductors. *Nano Letters* 2007, 7, 1888-1892.

75. Lee, J. H.; Marroquin, J.; Rhee, K. Y.; Park, S. J.; Hui, D. Cryomilling application of graphene to improve material properties of graphene/chitosan nanocomposites. *Composites Part B: Engineering* 2013, 45, 682-687.

76. Guo, J.; Ren, L.; Wang, R.; Zhang, C.; Yang, Y.; Liu, T. Water dispersible graphene noncovalently functionalized with tryptophan and its poly(vinyl alcohol) nanocomposite. *Composites Part B: Engineering* 2011, 42, 2130-2135.

77. Ansari, M. O.; Yadav, S. K.; Cho, J. W.; Mohammad, F. Thermal stability in terms of DC electrical conductivity retention and the efficacy of mixing technique in the preparation of nanocomposites of graphene/polyaniline over the carbon nanotubes/polyaniline. *Composites Part B: Engineering* 2013, 47, 155-161.

78. Jeon, G. W.; An, J.-E.; Jeong, Y. G. High performance cellulose acetate propionate composites reinforced with exfoliated graphene. *Composites Part B: Engineering* 2012, 43, 3412-3418.

79. Huang, X.; Yin, Z.; Wu, S.; Qi, X.; He, Q.; Zhang, Q.; Yan, Q.; Boey, F.; Zhang, H. Graphene-Based Materials: Synthesis, Characterization, Properties, and Applications. *Small* 2011, 7, 1876-1902.

80. Kim, K. S.; Zhao, Y.; Jang, H.; Lee, S. Y.; Kim, J. M.; Kim, K. S.; Ahn, J.-H.; Kim, P.; Choi, J.-Y.; Hong, B. H. Large-scale pattern growth of graphene films for stretchable transparent electrodes. *Nature* 2009, 457, 706-710.

81. Li, X.; Cai, W.; An, J.; Kim, S.; Nah, J.; Yang, D.; Piner, R.; Velamakanni, A.; Jung, I.; Tutuc, E.; Banerjee, S. K.; Colombo, L.; Ruoff, R. S. Large-Area Synthesis of High-Quality and Uniform Graphene Films on Copper Foils. *Science* 2009, 324, 1312-1314.

82. Wang, Y.; Xu, X.; Lu, J.; Lin, M.; Bao, Q.; Özyilmaz, B.; Loh, K. P. Toward High Throughput Interconvertible Graphane-to-Graphene Growth and Patterning. *ACS Nano* 2010, 4, 6146-6152.

83. Emtsev, K. V.; Bostwick, A.; Horn, K.; Jobst, J.; Kellogg, G. L.; Ley, L.; McChesney, J. L.; Ohta, T.; Reshanov, S. A.; Rohrl, J.; Rotenberg, E.; Schmid, A. K.; Waldmann, D.; Weber, H. B.; Seyller, T. Towards wafer-size graphene layers by atmospheric pressure graphitization of silicon carbide. *Nat Mater* 2009, 8, 203-207.

84. Choucair, M.; Thordarson, P.; Stride, J. A. Gram-scale production of graphene based on solvothermal synthesis and sonication. *Nat Nano* 2009, 4, 30-33.

85. Wang, X.; Zhi, L.; Tsao, N.; Tomović, Ž.; Li, J.; Müllen, K. Transparent Carbon Films as Electrodes in Organic Solar Cells. *Angewandte Chemie International Edition* 2008, 47, 2990-2992.

86. Hernandez, Y.; Nicolosi, V.; Lotya, M.; Blighe, F. M.; Sun, Z.; De, S.; McGovern, I. T.; Holland, B.; Byrne, M.; Gun'Ko, Y. K.; Boland, J. J.; Niraj, P.; Duesberg, G.; Krishnamurthy, S.; Goodhue, R.; Hutchison, J.; Scardaci, V.; Ferrari, A. C.; Coleman, J. N. High-yield production of graphene by liquid-phase exfoliation of graphite. *Nat Nano* 2008, 3, 563-568.

87. Lotya, M.; Hernandez, Y.; King, P. J.; Smith, R. J.; Nicolosi, V.; Karlsson, L. S.; Blighe, F. M.; De, S.; Wang, Z.; McGovern, I. T.; Duesberg, G. S.; Coleman, J. N. Liquid Phase Production of Graphene by Exfoliation of Graphite in Surfactant/Water Solutions. *Journal of the American Chemical Society* 2009, 131, 3611-3620.

88. Li, C.; Thostenson, E. T.; Chou, T.-W. Sensors and actuators based on carbon nanotubes and their composites: A review. *Composites Science and Technology* 2008, 68, 1227-1249.

89. Liu, N.; Luo, F.; Wu, H.; Liu, Y.; Zhang, C.; Chen, J. One-Step Ionic-Liquid-Assisted Electrochemical Synthesis of Ionic-Liquid-Functionalized Graphene Sheets Directly from Graphite. *Advanced Functional Materials* 2008, 18, 1518-1525.

90. Li, D.; Muller, M. B.; Gilje, S.; Kaner, R. B.; Wallace, G. G. Processable aqueous dispersions of graphene nanosheets. *Nat Nano* 2008, 3, 101-105.

91. Fan, X.; Peng, W.; Li, Y.; Li, X.; Wang, S.; Zhang, G.; Zhang, F. Deoxygenation of Exfoliated Graphite Oxide under Alkaline Conditions: A Green Route to Graphene Preparation. *Advanced Materials* 2008, 20, 4490-4493.

92. Liu, J.; Fu, S.; Yuan, B.; Li, Y.; Deng, Z. Toward a Universal "Adhesive Nanosheet" for the Assembly of Multiple Nanoparticles Based on a Protein-Induced Reduction/Decoration of Graphene Oxide. *Journal of the American Chemical Society* 2010, 132, 7279-7281.

93. Fernández-Merino, M. J.; Guardia, L.; Paredes, J. I.; Villar-Rodil, S.; Solís-Fernández, P.; Martínez-Alonso, A.; Tascón, J. M. D. Vitamin C Is an Ideal Substitute for Hydrazine in the Reduction of Graphene Oxide Suspensions. *The Journal of Physical Chemistry C* 2010, 114, 6426-6432.

94. Salas, E. C.; Sun, Z.; Lüttge, A.; Tour, J. M. Reduction of Graphene Oxide via Bacterial Respiration. *ACS Nano* 2010, 4, 4852-4856.

95. Moon, I. K.; Lee, J.; Ruoff, R. S.; Lee, H. Reduced graphene oxide by chemical graphitization. *Nat Commun* 2010, 1, 73.

96. Vinodgopal, K.; Neppolian, B.; Lightcap, I. V.; Grieser, F.; Ashokkumar, M.; Kamat, P. V. Sonolytic Design of Graphene−Au Nanocomposites. Simultaneous and Sequential Reduction of Graphene Oxide and Au(III). *The Journal of Physical Chemistry Letters* 2010, 1, 1987-1993.

97. Hassan, H. M. A.; Abdelsayed, V.; Khder, A. E. R. S.; AbouZeid, K. M.; Terner, J.; El-Shall, M. S.; Al-Resayes, S. I.; El-Azhary, A. A. Microwave synthesis of graphene sheets supporting metal nanocrystals in aqueous and organic media. *Journal of Materials Chemistry* 2009, 19, 3832-3837.

98. Zangmeister, C. D. Preparation and Evaluation of Graphite Oxide Reduced at 220 ℃. *Chemistry of Materials* 2010, 22, 5625-5629.

99. Lin, Z.; Yao, Y.; Li, Z.; Liu, Y.; Li, Z.; Wong, C.-P. Solvent-Assisted Thermal Reduction of Graphite Oxide. *The Journal of Physical Chemistry C* 2010, 114, 14819-14825.

100. Matsumoto, Y.; Koinuma, M.; Kim, S. Y.; Watanabe, Y.; Taniguchi, T.; Hatakeyama, K.; Tateishi, H.; Ida, S. Simple Photoreduction of Graphene Oxide Nanosheet under Mild Conditions. *ACS Applied Materials & Interfaces* 2010, 2, 3461-3466.

101. Cote, L. J.; Cruz-Silva, R.; Huang, J. Flash Reduction and Patterning of Graphite Oxide and Its Polymer Composite. *Journal of the American Chemical Society* 2009, 131, 11027-11032.

102. Xie, X.-L.; Mai, Y.-W.; Zhou, X.-P. Dispersion and alignment of carbon nanotubes in polymer matrix: A review. *Materials Science and Engineering: R: Reports* 2005, 49, 89-112.

103. Stankovich, S.; Dikin, D. A.; Dommett, G. H. B.; Kohlhaas, K. M.; Zimney, E. J.; Stach, E. A.; Piner, R. D.; Nguyen, S. T.; Ruoff, R. S. Graphene-based composite materials. *Nature* 2006, 442, 282-286.

104. Liu, Q.; Tu, J.; Wang, X.; Yu, W.; Zheng, W.; Zhao, Z. Electrical conductivity of carbon nanotube/poly(vinylidene fluoride) composites prepared by high-speed mechanical mixing. *Carbon* 2012, 50, 339-341.

105. Yang, D.-Q.; Rochette, J.-F.; Sacher, E. Functionalization of Multiwalled Carbon Nanotubes by Mild Aqueous Sonication. *The Journal of Physical Chemistry B* 2005, 109, 7788-7794.

106. Rastogi, R.; Kaushal, R.; Tripathi, S. K.; Sharma, A. L.; Kaur, I.; Bharadwaj, L. M. Comparative study of carbon nanotube dispersion using surfactants. *Journal of Colloid and Interface Science* 2008, 328, 421-428.

107. Fang, M.; Wang, K.; Lu, H.; Yang, Y.; Nutt, S. Covalent polymer functionalization of graphene nanosheets and mechanical properties of composites. *Journal of Materials Chemistry* 2009, 19, 7098-7105.

108. Chen, G.-X.; Li, Y.; Shimizu, H. Ultrahigh-shear processing for the preparation of polymer/carbon nanotube composites. *Carbon* 2007, 45, 2334-2340.

109. Spitalsky, Z.; Tasis, D.; Papagelis, K.; Galiotis, C. Carbon nanotube–polymer composites: Chemistry, processing, mechanical and electrical properties. *Progress in Polymer Science* 2010, 35, 357-401.

110. Kauffman, D. R.; Star, A. Carbon Nanotube Gas and Vapor Sensors. *Angewandte Chemie International Edition* 2008, 47, 6550-6570.

111. Fowler, J. D.; Allen, M. J.; Tung, V. C.; Yang, Y.; Kaner, R. B.; Weiller, B. H. Practical Chemical Sensors from Chemically Derived Graphene. *ACS Nano* 2009, 3, 301-306.

112. Yoon, H.; Jang, J. Conducting-Polymer Nanomaterials for High-Performance Sensor Applications: Issues and Challenges. *Advanced Functional Materials* 2009, 19, 1567-1576.

113. Bai, H.; Li, C.; Shi, G. Functional Composite Materials Based on Chemically Converted Graphene. *Advanced Materials* 2011, 23, 1089-1115.

114. Wei, B. Q.; Vajtai, R.; Jung, Y.; Ward, J.; Zhang, R.; Ramanath, G.; Ajayan, P. M. Microfabrication technology: Organized assembly of carbon nanotubes. *Nature* 2002, 416, 495-496.

115. Prasad, D.; Zhiling, L.; Satish, N.; Barrera, E. V. Nanotube film based on single-wall carbon nanotubes for strain sensing. *Nanotechnology* 2004, 15, 379.

116. Fiedler, B.; Gojny, F. H.; Wichmann, M. H.; Bauhofer, W.; Schulte, K. In *Can carbon nanotubes be used to sense damage in composites?*, Annales de chimie, Lavoisier: 2004; pp 81-94.

117. Erik, T. T.; Tsu-Wei, C. Real-time in situ sensing of damage evolution in advanced fiber composites using carbon nanotube networks. *Nanotechnology* 2008, 19, 215713.

118. Guinea, F.; Neto, A. C.; Peres, N. Electronic states and Landau levels in graphene stacks. *Physical Review B* 2006, 73, 245426.

119. Ni, Z. H.; Yu, T.; Lu, Y. H.; Wang, Y. Y.; Feng, Y. P.; Shen, Z. X. Uniaxial Strain on Graphene: Raman Spectroscopy Study and Band-Gap Opening. *ACS Nano* 2008, 2, 2301-2305.

120. Levy, N.; Burke, S. A.; Meaker, K. L.; Panlasigui, M.; Zettl, A.; Guinea, F.; Neto, A. H. C.; Crommie, M. F. Strain-Induced Pseudo–Magnetic Fields Greater Than 300 Tesla in Graphene Nanobubbles. *Science*

2010, 329, 544-547.

121. Lee, S.; Lee, K.; Zhong, Z. Wafer scale homogeneous bilayer graphene films by chemical vapor deposition. *Nano letters* 2010, 10, 4702-4707.

122. Fu, X.-W.; Liao, Z.-M.; Zhou, J.-X.; Zhou, Y.-B.; Wu, H.-C.; Zhang, R.; Jing, G.; Xu, J.; Wu, X.; Guo, W.; Yu, D. Strain dependent resistance in chemical vapor deposition grown graphene. *Applied Physics Letters* 2011, 99, 213107-213107-3.

123. Bae, S.-H.; Lee, Y.; Sharma, B. K.; Lee, H.-J.; Kim, J.-H.; Ahn, J.-H. Graphene-based transparent strain sensor. *Carbon* 2012.

124. Balageas, D. Introduction to Structural Health Monitoring. In *Structural Health Monitoring*, ISTE: 2010; pp 13-43.

125. Chang, P. C.; Flatau, A.; Liu, S. C. Review Paper: Health Monitoring of Civil Infrastructure. *Structural Health Monitoring* 2003, 2, 257-267.

126. Endo, M.; Muramatsu, H.; Hayashi, T.; Kim, Y. A.; Terrones, M.; Dresselhaus, M. S. Nanotechnology: /ˆBuckypaper/' from coaxial nanotubes. *Nature* 2005, 433, 476-476.

127. Dikin, D. A.; Stankovich, S.; Zimney, E. J.; Piner, R. D.; Dommett, G. H. B.; Evmenenko, G.; Nguyen, S. T.; Ruoff, R. S. Preparation and characterization of graphene oxide paper. *Nature* 2007, 448, 457-460.

128. Liao, K.; Li, S. Interfacial characteristics of a carbon nanotube–polystyrene composite system. *Applied Physics Letters* 2001, 79, 4225-4227.

129. Zhu, S.; Chung, D. D. L. Analytical model of piezoresistivity for strain sensing in carbon fiber polymer–matrix structural composite under flexure. *Carbon* 2007, 45, 1606-1613.

130. Dalmas, F.; Dendievel, R.; Chazeau, L.; Cavaillé, J.-Y.; Gauthier, C. Carbon nanotube-filled polymer composites. Numerical simulation of electrical conductivity in three-dimensional entangled fibrous networks. *Acta Materialia* 2006, 54, 2923-2931.

131. Hu, N.; Karube, Y.; Yan, C.; Masuda, Z.; Fukunaga, H. Tunneling effect in a polymer/carbon nanotube nanocomposite strain sensor. *Acta Materialia* 2008, 56, 2929-2936.

132. Oliva-Avilés, A. I.; Avilés, F.; Sosa, V. Electrical and piezoresistive properties of multi-walled carbon nanotube/polymer composite films aligned by an electric field. *Carbon* 2011, 49, 2989-2997.

133. Eswaraiah, V.; Balasubramaniam, K.; Ramaprabhu, S. One-pot synthesis of conducting graphene-polymer composites and their strain sensing application. *Nanoscale* 2012, 4, 1258-1262.

134. Li, C.; Chou, T.-W. Theoretical studies on the charge-induced failure of single-walled carbon nanotubes. *Carbon* 2007, 45, 922-930.

135. Kalaitzidou, K.; Fukushima, H.; Drzal, L. T. Multifunctional polypropylene composites produced by incorporation of exfoliated graphite nanoplatelets. *Carbon* 2007, 45, 1446-1452.

136. Kim, H.; Abdala, A. A.; Macosko, C. W. Graphene/Polymer Nanocomposites. *Macromolecules* 2010, 43, 6515-6530.

137. Fan, Z.; Yan, J.; Zhi, L.; Zhang, Q.; Wei, T.; Feng, J.; Zhang, M.; Qian, W.; Wei, F. A Three-Dimensional Carbon Nanotube/Graphene Sandwich and Its Application as Electrode in Supercapacitors. *Advanced Materials* 2010, 22, 3723-3728.

138. Kim, U. J.; Lee, I. H.; Bae, J. J.; Lee, S.; Han, G. H.; Chae, S. J.; Güneş, F.; Choi, J. H.; Baik, C. W.; Kim, S. I.; Kim, J. M.; Lee, Y. H. Graphene/carbon nanotube hybrid-based transparent 2D optical array.

Advanced Materials 2011, 23, 3809-3814.

139. Peng, L.; Feng, Y.; Lv, P.; Lei, D.; Shen, Y.; Li, Y.; Feng, W. Transparent, Conductive, and Flexible Multiwalled Carbon Nanotube/Graphene Hybrid Electrodes with Two Three-Dimensional Microstructures. *The Journal of Physical Chemistry C* 2012, 116, 4970-4978.

140. Lee, S. H.; Lee, D. H.; Lee, W. J.; Kim, S. O. Tailored Assembly of Carbon Nanotubes and Graphene. *Advanced Functional Materials* 2011, 21, 1338-1354.

141. Lv, R.; Cui, T.; Jun, M.-S.; Zhang, Q.; Cao, A.; Su, D. S.; Zhang, Z.; Yoon, S.-H.; Miyawaki, J.; Mochida, I.; Kang, F. Open-Ended, N-Doped Carbon Nanotube–Graphene Hybrid Nanostructures as High-Performance Catalyst Support. *Advanced Functional Materials* 2011, 21, 999-1006.

142. Das, S.; Seelaboyina, R.; Verma, V.; Lahiri, I.; Hwang, J. Y.; Banerjee, R.; Choi, W. Synthesis and characterization of self-organized multilayered graphene-carbon nanotube hybrid films. *Journal of Materials Chemistry* 2011, 21, 7289-7295.

143. Lahiri, I.; Verma, V. P.; Choi, W. An all-graphene based transparent and flexible field emission device. *Carbon* 2011, 49, 1614-1619.

144. Unnikrishnan, B.; Mani, V.; Chen, S.-M. Highly sensitive amperometric sensor for carbamazepine determination based on electrochemically reduced graphene oxide–single-walled carbon nanotube composite film. *Sensors and Actuators B: Chemical* 2012, 173, 274-280.

145. Yen, M.-Y.; Hsiao, M.-C.; Liao, S.-H.; Liu, P.-I.; Tsai, H.-M.; Ma, C.-C. M.; Pu, N.-W.; Ger, M.-D. Preparation of graphene/multi-walled carbon nanotube hybrid and its use as photoanodes of dye-sensitized solar cells. *Carbon* 2011, 49, 3597-3606.

146. Li, X.; Levy, C.; Elaadil, L. Multiwalled carbon nanotube film for strain sensing. *Nanotechnology* 2008, 19, 045501.

147. Mahar, B.; Laslau, C.; Yip, R.; Sun, Y. Development of Carbon Nanotube-Based Sensors—A Review. *Sensors Journal, IEEE* 2007, 7, 266-284.

148. Sakhaee-Pour, A.; Ahmadian, M. T.; Vafai, A. Potential application of single-layered graphene sheet as strain sensor. *Solid State Communications* 2008, 147, 336-340.

149. Arsat, R.; Breedon, M.; Shafiei, M.; Spizziri, P. G.; Gilje, S.; Kaner, R. B.; Kalantar-zadeh, K.; Wlodarski, W. Graphene-like nano-sheets for surface acoustic wave gas sensor applications. *Chemical Physics Letters* 2009, 467, 344-347.

150. Lee, Y.; Bae, S.; Jang, H.; Jang, S.; Zhu, S.-E.; Sim, S. H.; Song, Y. I.; Hong, B. H.; Ahn, J.-H. Wafer-Scale Synthesis and Transfer of Graphene Films. *Nano Letters* 2010, 10, 490-493.

151. Lu, Y.; Goldsmith, B. R.; Kybert, N. J.; Johnson, A. T. C. DNA-decorated graphene chemical sensors. *Applied Physics Letters* 2010, 97, 083107-083107-3.

152. Li, W.; Geng, X.; Guo, Y.; Rong, J.; Gong, Y.; Wu, L.; Zhang, X.; Li, P.; Xu, J.; Cheng, G.; Sun, M.; Liu, L. Reduced Graphene Oxide Electrically Contacted Graphene Sensor for Highly Sensitive Nitric Oxide Detection. *ACS Nano* 2011, 5, 6955-6961.

153. Yoon, H. J.; Jun, D. H.; Yang, J. H.; Zhou, Z.; Yang, S. S.; Cheng, M. M.-C. Carbon dioxide gas sensor using a graphene sheet. *Sensors and Actuators B: Chemical* 2011, 157, 310-313.

154. Zhang, B.; Cui, T. An ultrasensitive and low-cost graphene sensor based on layer-by-layer nano self-assembly. *Applied Physics Letters* 2011, 98, 073116-073116-3.

155. Shao, Y.; Wang, J.; Wu, H.; Liu, J.; Aksay, I. A.; Lin, Y. Graphene Based Electrochemical Sensors and

Biosensors: A Review. *Electroanalysis* 2010, 22, 1027-1036.

156. Kim, Y. J.; Cha, J. Y.; Ham, H.; Huh, H.; So, D. S.; Kang, I. Preparation of piezoresistive nano smart hybrid material based on graphene. *Current Applied Physics* 2011, 11, S350-S352.

157. Choi, S.-M.; Jhi, S.-H.; Son, Y.-W. Effects of strain on electronic properties of graphene. *Physical Review B* 2010, 81, 081407.

158. Guinea, F.; Katsnelson, M. I.; Geim, A. K. Energy gaps and a zero-field quantum Hall effect in graphene by strain engineering. *Nat Phys* 2010, 6, 30-33.

159. Bae, S.-H.; Lee, Y.; Sharma, B. K.; Lee, H.-J.; Kim, J.-H.; Ahn, J.-H. Graphene-based transparent strain sensor. *Carbon* 2013, 51, 236-242.

160. Zhu, Y.; Murali, S.; Cai, W.; Li, X.; Suk, J. W.; Potts, J. R.; Ruoff, R. S. Graphene and Graphene Oxide: Synthesis, Properties, and Applications. *Advanced Materials* 2010, 22, 3906-3924.

161. Mohiuddin, T. M. G.; Lombardo, A.; Nair, R. R.; Bonetti, A.; Savini, G.; Jalil, R.; Bonini, N.; Basko, D. M.; Galiotis, C.; Marzari, N.; Novoselov, K. S.; Geim, A. K.; Ferrari, A. C. Uniaxial strain in graphene by Raman spectroscopy: G peak splitting, Grüneisen parameters, and sample orientation. *Physical Review B* 2009, 79, 205433.

162. Ramanathan, T.; Abdala, A.; Stankovich, S.; Dikin, D.; Herrera-Alonso, M.; Piner, R.; Adamson, D.; Schniepp, H.; Chen, X.; Ruoff, R. Functionalized graphene sheets for polymer nanocomposites. *Nature Nanotechnology* 2008, 3, 327-331.

163. Zhang, L.; Wang, Z.; Xu, C.; Li, Y.; Gao, J.; Wang, W.; Liu, Y. High strength graphene oxide/polyvinyl alcohol composite hydrogels. *Journal of Materials Chemistry* 2011, 21, 10399-10406.

164. Wang, J.; Wang, X.; Xu, C.; Zhang, M.; Shang, X. Preparation of graphene/poly(vinyl alcohol) nanocomposites with enhanced mechanical properties and water resistance. *Polymer International* 2011, 60, 816-822.

165. Lee, H.; Scherer, N. F.; Messersmith, P. B. Single-molecule mechanics of mussel adhesion. *Proceedings of the National Academy of Sciences* 2006, 103, 12999-13003.

166. Lee, H.; Dellatore, S. M.; Miller, W. M.; Messersmith, P. B. Mussel-Inspired Surface Chemistry for Multifunctional Coatings. *Science* 2007, 318, 426-430.

167. Yang, L.; Phua, S. L.; Teo, J. K. H.; Toh, C. L.; Lau, S. K.; Ma, J.; Lu, X. A Biomimetic Approach to Enhancing Interfacial Interactions: Polydopamine-Coated Clay as Reinforcement for Epoxy Resin. *ACS Applied Materials & Interfaces* 2011, 3, 3026-3032.

168. Kang, S. M.; Park, S.; Kim, D.; Park, S. Y.; Ruoff, R. S.; Lee, H. Simultaneous Reduction and Surface Functionalization of Graphene Oxide by Mussel-Inspired Chemistry. *Advanced Functional Materials* 2011, 21, 108-112.

169. Kang, S. M.; Park, S.; Kim, D.; Park, S. Y.; Ruoff, R. S.; Lee, H. Simultaneous Reduction and Surface Functionalization of Graphene Oxide by Mussel-Inspired Chemistry. *Advanced Functional Materials* 2011, 21, 108-112.

170. Shin, M.; Kim, H. K.; Lee, H. Dopamine-loaded poly(d,l-lactic-co-glycolic acid) microspheres: New strategy for encapsulating small hydrophilic drugs with high efficiency. *Biotechnology Progress* 2014, 30, 215-223.

171. Ryu, S.; Lee, Y.; Hwang, J.-W.; Hong, S.; Kim, C.; Park, T. G.; Lee, H.; Hong, S. H. High-Strength Carbon Nanotube Fibers Fabricated by Infiltration and Curing of Mussel-Inspired Catecholamine Polymer.

Advanced Materials 2011, 23, 1971-1975.

172. Yamaguchi, H.; Eda, G.; Mattevi, C.; Kim, H.; Chhowalla, M. Highly Uniform 300 mm Wafer-Scale Deposition of Single and Multilayered Chemically Derived Graphene Thin Films. *ACS Nano* 2010, 4, 524-528.

173. d'Ischia, M.; Napolitano, A.; Pezzella, A.; Meredith, P.; Sarna, T. Chemical and Structural Diversity in Eumelanins: Unexplored Bio-Optoelectronic Materials. *Angewandte Chemie International Edition* 2009, 48, 3914-3921.

174. Dreyer, D. R.; Miller, D. J.; Freeman, B. D.; Paul, D. R.; Bielawski, C. W. Elucidating the Structure of Poly (dopamine). *Langmuir* 2012, 28, 6428-6435.

175. Guo, L.; Liu, Q.; Li, G.; Shi, J.; Liu, J.; Wang, T.; Jiang, G. A mussel-inspired polydopamine coating as a versatile platform for the in situ synthesis of graphene-based nanocomposites. *Nanoscale* 2012, 4, 5864-5867.

176. Kong, J.; Yee, W. A.; Yang, L.; Wei, Y.; Phua, S. L.; Ong, H. G.; Ang, J. M.; Li, X.; Lu, X. Highly electrically conductive layered carbon derived from polydopamine and its functions in SnO2-based lithium ion battery anodes. *Chemical Communications* 2012, 48, 10316-10318.

177. Paredes, J. I.; Villar-Rodil, S.; Martínez-Alonso, A.; Tascón, J. M. D. Graphene Oxide Dispersions in Organic Solvents. *Langmuir* 2008, 24, 10560-10564.

178. Centeno, S. A.; Shamir, J. Surface enhanced Raman scattering (SERS) and FTIR characterization of the sepia melanin pigment used in works of art. *Journal of Molecular Structure* 2008, 873, 149-159.

179. Sahoo, N. G.; Rana, S.; Cho, J. W.; Li, L.; Chan, S. H. Polymer nanocomposites based on functionalized carbon nanotubes. *Progress in Polymer Science* 2010, 35, 837-867.

180. Zhao, X.; Zhang, Q.; Chen, D.; Lu, P. Enhanced Mechanical Properties of Graphene-Based Poly(vinyl alcohol) Composites. *Macromolecules* 2010, 43, 2357-2363.

181. Wang, H.; Feng, C.-D.; Sun, S.-L.; Segre, C. U.; Stetter, J. R. Comparison of conductometric humidity-sensing polymers. *Sensors and Actuators B: Chemical* 1997, 40, 211-216.

182. Fuke, M. V.; Adhyapak, P. V.; Mulik, U. P.; Amalnerkar, D. P.; Aiyer, R. C. Electrical and humidity characterization of m-NA doped Au/PVA nanocomposites. *Talanta* 2009, 78, 590-595.

183. Li, Y.; Ying, B.; Hong, L.; Yang, M. Water-soluble polyaniline and its composite with poly(vinyl alcohol) for humidity sensing. *Synthetic Metals* 2010, 160, 455-461.

184. Barkauskas, J. Investigation of conductometric humidity sensors. *Talanta* 1997, 44, 1107-1112.

185. Yang, M.-R.; Chen, K.-S. Humidity sensors using polyvinyl alcohol mixed with electrolytes. *Sensors and Actuators B: Chemical* 1998, 49, 240-247.

186. Tong, S.; Fan, T.; Zeng, W.; Zhang, D.; Kao, C.-Y.; Liu, Y.; Min, Y.; Epstein, A. J. Formation of tunable three-dimensional networks of graphene hydrogel via covalent bond. *Synthetic Metals* 2014, 196, 27-32.

187. Zhou, H.; Yao, W.; Li, G.; Wang, J.; Lu, Y. Graphene/poly(3,4-ethylenedioxythiophene) hydrogel with excellent mechanical performance and high conductivity. *Carbon* 2013, 59, 495-502.

188. Wang, H.; Xu, Z.; Yi, H.; Wei, H.; Guo, Z.; Wang, X. One-step preparation of single-crystalline Fe2O3 particles/graphene composite hydrogels as high performance anode materials for supercapacitors. *Nano Energy* 2014, 7, 86-96.

189. Yuan, M.; Liu, A.; Zhao, M.; Dong, W.; Zhao, T.; Wang, J.; Tang, W. Bimetallic PdCu nanoparticle

decorated three-dimensional graphene hydrogel for non-enzymatic amperometric glucose sensor. *Sensors and Actuators B: Chemical* 2014, 190, 707-714.

190. Luan, V. H.; Tien, H. N.; Hoa, L. T.; Hien, N. T. M.; Oh, E.-S.; Chung, J.; Kim, E. J.; Choi, W. M.; Kong, B.-S.; Hur, S. H. Synthesis of a highly conductive and large surface area graphene oxide hydrogel and its use in a supercapacitor. *Journal of Materials Chemistry A* 2013, 1, 208-211.

191. Zhang, J.; Yang, H.; Shen, G.; Cheng, P.; Zhang, J.; Guo, S. Reduction of graphene oxide vial-ascorbic acid. *Chemical Communications* 2010, 46, 1112-1114.

192. Schniepp, H. C.; Li, J.-L.; McAllister, M. J.; Sai, H.; Herrera-Alonso, M.; Adamson, D. H.; Prud'homme, R. K.; Car, R.; Saville, D. A.; Aksay, I. A. Functionalized Single Graphene Sheets Derived from Splitting Graphite Oxide. *The Journal of Physical Chemistry B* 2006, 110, 8535-8539.

193. Geng, Y.; Wang, S. J.; Kim, J.-K. Preparation of graphite nanoplatelets and graphene sheets. *Journal of Colloid and Interface Science* 2009, 336, 592-598.

194. Zhang, L.; Shi, G. Preparation of Highly Conductive Graphene Hydrogels for Fabricating Supercapacitors with High Rate Capability. *The Journal of Physical Chemistry C* 2011, 115, 17206-17212.

195. Pham, V. H.; Cuong, T. V.; Hur, S. H.; Oh, E.; Kim, E. J.; Shin, E. W.; Chung, J. S. Chemical functionalization of graphene sheets by solvothermal reduction of a graphene oxide suspension in N-methyl-2-pyrrolidone. *Journal of Materials Chemistry* 2011, 21, 3371-3377.

196. Wang, G.; Yang, J.; Park, J.; Gou, X.; Wang, B.; Liu, H.; Yao, J. Facile Synthesis and Characterization of Graphene Nanosheets. *The Journal of Physical Chemistry C* 2008, 112, 8192-8195.

197. Grosman, A.; Ortega, C. Capillary Condensation in Porous Materials. Hysteresis and Interaction Mechanism without Pore Blocking/Percolation Process. *Langmuir* 2008, 24, 3977-3986.

198. Zhang, X.; Sui, Z.; Xu, B.; Yue, S.; Luo, Y.; Zhan, W.; Liu, B. Mechanically strong and highly conductive graphene aerogel and its use as electrodes for electrochemical power sources. *Journal of Materials Chemistry* 2011, 21, 6494-6497.

Acknowledgements